UNIVERSITÀ DELLA CALABRIA

Universitá della Calabria

Dipartimento di Fisica

Scuola di dottorato
Bernardino Telesio

Curriculum
Sistemi Complessi

Innovative systems for energy harvesting and storage - Fis/03

Coordinatore:
Chiar.mo Prof. Roberto Bartolino

Relatori:
Chiar.mo Prof. Gennaro Chiarello

Chiar.mo Dr. Andrea Goldoni

Candidato:
Marco Caputo

Anno Accademico 2013/2014

Universitá della Calabria

Dipartimento di Fisica

Scuola di dottorato
Bernardino Telesio

Curriculum
Sistemi Complessi

Innovative systems for energy harvesting and storage - Fis/03

Coordinatore:
Chiar.mo Prof. Vincenzo Carbone

Relatori:
Chiar.mo Prof. Gennaro Chiarello

Chiar.mo Dr. Andrea Goldoni

Candidato:
Marco Caputo

Anno Accademico 2013/2014

List of Publications

Published

- A. Politano, M. Caputo, A. Goldoni, P. Torelli and G. Chiarello *Segregation and Selective Oxidation of Ni Atoms in Pt_3Ni (111) in a Low-Pressure Oxygen Environment.* The Journal of Physical Chemistry C **117**, 27007 (2013)
- I. Quinzeni, S. Ferrari, E. Quartarone, D. Capsoni, M. Caputo, A. Goldoni, P. Mustarelli and M. Bini *Fabrication and electrochemical characterization of amorphous lithium iron silicate thin films as positive electrodes for lithium batteries.* Journal of Power Sources **266**, 179 (2014)
- A. Radivo, E. Sovernigo, M. Caputo, S. Dal Zilio, T. Endale, A. Pozzato, A. Goldoni and M. Tormen *Patterning PEDOT:PSS and tailoring its electronic properties by water-vapour-assisted nanoimprint lithography.* RSC Advances **4**, 34014 (2014)
- M. Caputo, M. Panighel, L. Petaccia, C. Struzzi, V. Alijani, M. Coreno, M. De Simone, G. Fratesi, G. Di Santo and A. Goldoni *Metallic Picene/C60 heterojunctions and the effect of potassium doping.* Physical Review B (Rapid Comunication) **90**, 201401(R) (2014)
- M. Marsili, P. Umari, G. Di Santo, M. Caputo, M. Panighel, A. Goldoni, M. Kumar and M. Pedio *Solid state effects on the electronic structure of H_2OEP.* Physical Chemistry Chemical Physics **16**, 27104 (2014)

Submitted

- M. Caputo, B. A. Taleatu, C. Castellarin-Cudia, G. Di Santo, M. Panighel, L. Floreano and A. Goldoni *Ultrafast charge transfer in Zn-Tetraphenyl Porphyrin and nanostructured ZnO interface: a resonant photoemission study.* Submitted to Journal of Physical Chemistry Letters
- M. Caputo, F. Borghi, N. Cefarin, A. Radivo, N. Demitri, M. Panighel, G. Di Santo, S. Moretti, B. Policicchio, A. Giglia, M. Polentarutti, M. Tormen, P. Umari, and A. Goldoni *Unravelling the origin of the high excitonic diffusion length in $MAPbI_{3-x}Cl_x$ mixed perovskite.* Submitted to Nature Materials

Not included in this thesis

- M. Caputo, G. Di Santo, P. Parisse, L. Petaccia, L. Floreano, A.Verdini, M. Panighel, C. Struzzi, B. Taleatu, C. Lal and A. Goldoni *Experimental Study of Pristine and Alkali Metal Doped Picene Layers: Confirmation of the Insulating Phase in Multilayer Doped Compounds.* The Journal of Physical Chemistry C **113**, 19902 (2012)
- A. Politano, M. Caputo, S. Nappini, F. Bondino, E. Magnano, Z. S. Aliev, M. B. Babanly, A. Goldoni G. Chiarello and E. V. Chulkov *Exploring the Surface Chemical Reactivity of Single Crystals of Binary and Ternary Bismuth Chalcogenides.* The Journal of Physical Chemistry C **118**, 21517 (2013)
- D. Pacilé, S. Lisi, I. Di Bernardo, M. Papagno, L. Ferrari, M. Pisarra, M. Caputo, S. K. Mahatha, P. M. Sheverdyaeva, P. Moras, P. Lacovig, S. Lizzit, A. Baraldi, M. G. Betti and C. Carbone *Electronic structure of Graphene/Co interfaces.* Physical Review B **90**, 195446 (2014)

Abstract

Energy harvesting represent one of the most important problem in today's society: climate changes and geopolitical instabilities remember ourself everyday the needs to find alternatives to hydrocarbon exploiting. During my PhD period I concentrated my efforts in elaborating new scientific knowledge to be applied to innovative energy harvesting and storage systems.

Most of my work has been focused on the organic energy harvesting systems, like photoelectrochemical cells, solid-state organic photovoltaic cell, and hybrid organic-inorganic perovskites. Electronic structure and interface dynamics of macromolecules (poprhyrins, phthalocyanines, phenacenes, and fullerenes) have been investigated by mean of synchrotron radiation-based experimental techniques. Alternative systems for dye sensitized solar cell to the commonly used Ru-dyes/TiO_2 interface were investigated, with encouraging results in the case of Zn-tetra phenyl poprhyrine/ZnO, while K doped picene/C_{60} interface exhibited properties with possible applications in the field of superconductivity. Interface effect have been found to cause also in hybrid organic-inorganic perovskites interesting long-living excitonic states, whose tailoring can lead to high efficiency devices.

Doping and morphology effects have been investigated for polymers and molecular thin films. It was shown that nanoimprinting treatments can improve the PEDOT:PSS conductibility and in the meanwhile control the work function, both key parameters in an organic photovoltaic device, instead simply crystal packing in octaethyl porphyrins has found to be responsible for heavy electronic modifications in the frontier orbitals.

Efforts were also made in finding new systems for energy storage. Innovative electrodes for lithium batteries were chemically characterized, while a study on the oxidation dynamic of metallic alloy usable in advanced fuel cells revealed interesting segregation dynamics.

Contents

Introduction

It is universally recognized that modern society starts its development in the industrial revolution of the XVIII century. The term revolution means a new way to intend the human labour: until the advent of machineries people were called to spend most of their energy in physical work, limiting production to manufactures that could be realized with just some simple tools. A breakthrough for the evolution of our society came with the invention of the steam engine. Steam engines were capable of delivering the power of hundred of men, with the obvious consequence of speeding up several process, but also opening completely new perspectives. One example over all is the train: steam locomotives were capable of moving tons of load, beating year after year speed records.

The key aspect of the industrial revolution was simply the power available to be employed. Transformation of the chemical energy contained in coal into heat and mechanical work opened the way to extremely fast social changes that shaped the society were we live today. Still today our society is based on the energy availability: every aspect of our life needs an external energy source to be accomplished. Since the industrial revolution days the world energy demand grew up, and if today the western society is engaged to diminish its energy consumption, the new developing economies (mainly India, China, ad Brazil) are experiencing an extremely fast industrial developments and, as consequence, an exponential energy demand.

Unfortunately, since the XVII century our external power sources remained confined mainly to coal and hydrocarbons. Their availability in huge quantity, and their relatively cheap extraction cost, made hydrocarbons the perfect choice for a fast industrial growth. Only in the last decades this paradigm showed its limit. First of all hydrocarbons are a finite (even if in large quantities) resources. Nowadays the discovery of "conventional" oil and gas deposits is diminishing, while the usage of fracking, oil sands, and other unconventional and invasive methods is required to increase the annual oil production. Secondly, the largest hydrocarbons reservoirs are far from the principal consuming countries, often in lands characterized by political instabilities. But, most important, the hydrocarbons exploiting is altering the delicate equilibrium of the atmosphere: as effect of hydrocarbons combustion large quantities of carbon dioxide are introduced in the atmosphere, increasing the greenhouse effect. This can lead to abrupt climate changes, causing the increase of desert regions, the polar glaciers fusion, and other effects that will reduce our planet habitability.

All these considerations make the development of a new way to intend energy a priority for science and technology. In this thesis I will present fundamental investigations on different systems, aimed to move forward the field of renewable energy conversion and storage. After a short general introduction to energy conversion and storage systems given in this chapter along with an introduction on the experimental techniques, I will present the result of my work. The second part of this thesis contains papers, and a short introduction for each of them.

Renewable energy conversion: innovative solar cells

The total world energy consumption (primary plus electric) is approximately 10^{14} KWh/year, while the solar radiance on the ground is approximately 10^{18} KWh/year. It is clear that the energy we receive form the sun could satisfy the always increasing world energy demand, but unfortunately the cost of the solar energy exploiting is too high if compared with hydrocarbons-derived energy.

Today's commercial photovoltaic devices are based mainly on p-n or p-i-n semiconductors junctions. These devices require high purity materials and high temperature treatments, that make the final product too expensive for mass-applications. Starting from '80s three new alternative paradigms is being developed: Dye Sensitized Solar Cells (DSSCs), Organic Photovoltaic (OPV), and, very recently, Organic/Inorganic Perovskites Solar Cells.

Dye Sensitized Solar Cells were firstly introduced by O'Regan and Grätzel in 1991 [1]. In these devices the photoactive layer is formed by molecular dyes. They are excited by solar light causing electron trasfer to their substrate, a nanostructured layer of some transition metal oxide: typically TiO_2 or ZnO. Successively the dye is regenerated by a iodide-tri-iodide redox solution in contact with a counter electrode, generating a current flow between this and the oxide outside the cell. DSSCs do not need high temperature processing, and they are quite tolerant to impurities. The best efficiency so far reported for these cells excedeed 12% [2], but, as for most of the best-efficiency DSSCs, it has been obtained using a ruthenium-based dye. In prospect of a mass usage of these devices it is mandatory finding cheaper alternative dyes, possibly exclusively organic ones.

The major practical issue of DSSCs is related to the electrolytic solution. It is typically extremely acid, and, since a photovoltaic panel has to last years outdoors, it requires accurate and expensive cell sealing. Another class of innovative photovoltaic devices does not suffer of this problem. Organic Photovoltaic has been introduced in its modern form Tang in 1986 [3]. This type of cells rely on a heterojunction of two different organic molecules or polymers: one electron acceptor, and the other electron donor. An incident photon creates an excitons in the organic blend that diffuses until it reaches the interface between the two different molecules. Here the exciton is separated in two free charges that migrate to the electrodes. Their main components, along with the solution-precessed fabrication method, are extremely cheap and allow the possibility to produce large area modules with very high throughput methods, like ink-jet or roll-to-roll printing [4]. If OPV modules appear very robust from a mechanical point of view, they still suffer low efficiency if compared with other technologies [5]. Their efficiency is mainly limited by their short excitonic diffusion length [6] that requires a high degree of control on the morphology of the bulk heterojunction [7, 8].

In the attempt of substituting the Ru-based dyes for DSSCs, in 2009 Kojima's group synthesized a mixed organic/inorganic light absorber [9]. Instead of organic molecules, a crystalline perovskite layer based on lead halides and methylammonium salts has been employed as light sensitizer. Although initial performances were close to the state-of-the-art organic cells, perovskite based cells degraded very soon due to the solubility of the perovskite in the electrolytic solution. Once this issue has been solved substituting the redox solution by a solid hole transporting material (HTM) [10], this class of photovoltaic devices catalized the attention of the scientific community. Low temperature processing, abundant constituting materials, and efficiency that soon exceeded 15% [11] promise soon very reliable devices. Although electrical and optical characterizations of this new material have been extensively performed by many groups [10, 12, 13], much less is know about the chemistry of the compound and its stability under operation.

Energy storage: innovative lithium batteries and fuel cell

If sun can become our primary energy source, we have to be aware that its power supply is not continuous and tunable. Sun can irradiate our solar cell during the day, but something capable of store and deliver its energy is needed, irrespectively of sun irradiation and in all the situations that need a compact and powerful source. In the new renewable paradigm something analogous to fossil fuel is needed, the renewable counterpart of benzine, diesel and natural gas. High specific energy per unit weight is the fundamental requisite, in case for example to power a mean of transportation or to deliver energy during night.

Among today's energy storage alternatives we have, the only devices that answer these needs are lithium-ion batteries and fuel cells. The first ones are small devices, lightweight and they can store directly electrical power. The latter are much more similar to a conventional engine: they produce electrical power thanks to a fuel, in most of the cases hydrogen that can be produced by hydrolysis.

Lithium shows the highest redox potentials, along with the lowest mass among ions. Joining these two properties in the lithium ion batteries results in the highest specific energy per unit mass in the batteries scenario [14]. The working principle of the lithium ion batteries does not differ from all other type of batteries: a positive ion diffusion inside the cell drive an electron flow, so an electric current, in an external circuit. An oxidation reaction occurs at the anode (usually Li-doped graphite), were Li^+ ions detach from the surface to migrate in a electrolytic solution towards the cathode (usually a lithium-transition metal oxide salt, as $LiCoO_2$), were a reduction reaction intercalate reversibly the Li ions in the cathode. The major issue concerning batteries, comprised Li-ion batteries of course, regards the presence of the electrolytic solutions: the impossibility to use water as solvent requires the usage of highly flammable organic solvents [15]. Substituting the liquid solution with a solid electrolyte would be highly desirable, along with finding new cathode materials, with a better

interface with the solid electrolyte and capable of better lithium atoms intercalation.

Fuel cells use the same working principle of the batteries, but instead of having a finite reservoir of positive ions that migrates back and forth between the electrodes, they use a fuel that continuously provide ions. The most diffuse type of fuel cell is the polymer electrolyte membrane fuel cell (PEMFC). In this case the fuel is molecular hydrogen that enters in contact with the anode freeing its electrons. While electrons flow to the cathode in an external circuit generating electric current, protons flow through a polymeric proton exchange membrane (PEM). Once arrived to the cathode, protons and electrons recombine with the oxygen present in the air forming water. The fuel cell technology, although represents a niche in the energy conversion scenario, is well established since many decades, with efficiencies that can arrive up to 50%. However, in spite of their efficiency and maturity, the actual fuel cell technology cannot become a wide-spread energy conversion solution. Hydrogen and oxygen dissociation at ambient temperature needs high efficiency catalysts, and at the moment only platinum-based materials represent an acceptable choice in term of catalytic efficiency [16, 17].

Experimental techniques: spectroscopy and synchrotron light

All the systems investigated in this thesis have been characterized from a spectroscopic point of view, either with laboratory source or with synchrotron light. The main techniques used are photoemssion spectroscopy, X-ray absorption spectroscopy, and the combination of the two: resonant photoemission spectroscopy.

Photoemission Spectroscopy (PES)

Photoemission Spectroscopy is one of the simplest way to accede to the electronic structure of matter [18]. In this process (see fig.1) an UV or a X-ray photon impinge on the surface of the sample causing the emission of an electron with a kinetic energy

$$E_{kin} = h\nu - E_B - \Phi_0$$

Depending from the energy of the impinging photon we can divide PES in X-ray Photoemission Spectroscopy (XPS) or UV Photoemission Spectroscopy (UPS).

XPS is manly used to probe core levels. With this technique we can understand which elements compose our sample, but also their chemistry looking at the chemical shift of the spectral features. In fact, varying the atoms chemical environment will result in a shift in the binding energy of its core levels.

By mean of UPS we can investigate the electronic structure of the valence band. It becomes really important in the case of interfaces, allowing the detection of band bending, screening effect, electronic correlation and so on.

Both XPS and UPS can be performed using laboratory sources or synchrotron light.

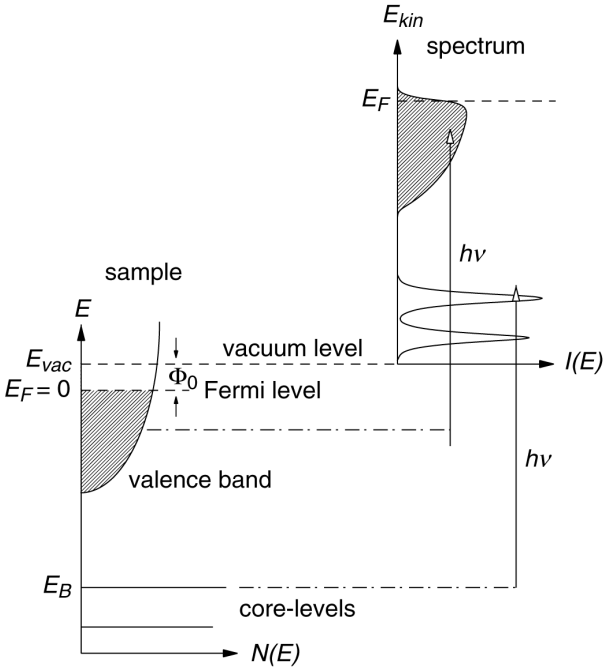

FIGURE 1: Draw of a photoemission spectroscopy experiment

X-ray Absorption Spectroscopy (XAS)

X-ray absorption spectroscopy is commonly used to investigate the unoccupied states of the system [19]. Here the impinging photons excite an electron from the core levels to the unoccupied states, and the subsequent de-excitation process (Auger autoionization or fluorescence) is collected (see fig.2).

With XAS it is possible also to measure the absorption geometry of molecules. The transition probability $|i\rangle \rightarrow |f\rangle$ is given by

$$I \propto |\mathbf{e} \cdot \langle f|\mathbf{p}|i\rangle|^2$$

For a *spheric* initial state and a *vector* final state (e.g. $1s \rightarrow 2p$ transition, a common investigated process for organic molecules composed mainly of C and N) the matrix element points in the direction of the final state. With δ is the angle between the light polarization vector and the final state vector the transition probability becomes

$$I \propto \cos^2 \delta$$

Running XAS measures requires to scan the photon energy across the absorption threshold of the investigated elements. This calls necessarily for a synchrotron lightsource.

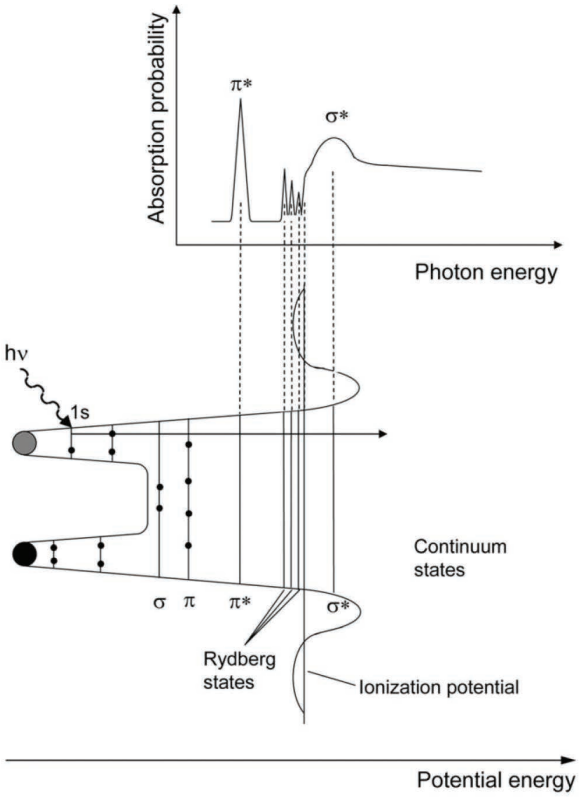

FIGURE 2: Scheme of X-ray absorption spectroscopy of a diatomic molecule

Resonant Photoemission Spectroscopy (ResPES)

Joining photoemission spectroscopy and X-ray absorption spectroscopy results in resonant photoemission spectroscopy [20]. Here valence bands are acquired while the excitation energy varies across the absorption threshold of the element investigated (see fig.3).

Once the excitation energy is sufficient to promote electrons from the core levels to the unoccupied states, the de-excitation channels (participant and spectator, cfr. fig.3) interfere with the direct photoemission from the valence band, giving rise to resonances.

This effect can be used to decouple contributions to the valence band coming from different species, since the x-ray absorption (and the consequent de-excitation process) is element specific. Another application of this technique is the charge transfer time measurement. In the case the probed system is coupled with a continuum (as the case of a molecule adsorbed on a surface) the electron excited can be transferred to the continuum in a characteristic time shorter than the core-hole lifetime. If this happens the participator and spectator decay channels are no longer available, and a comparison between the coupled and uncoupled systems shows a clear quenching of the resonant features.

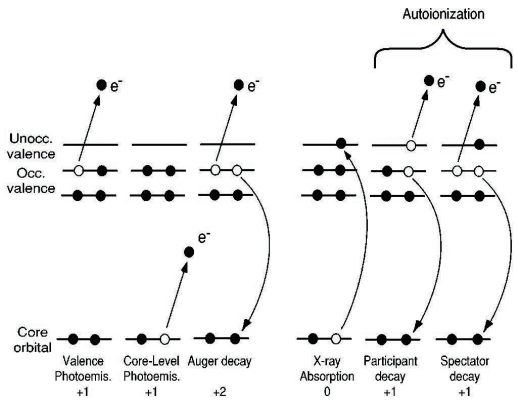

FIGURE 3: Process involved in resonant photoemission spectroscopy

Synchrotron light

All the experiments reported in this thesis were performed on beamlines hosted in Elettra synchrotron light source. Elettra is a third generation synchrotron: it consists of a small linear accelerator that inject bunches of 100 MeV energy electrons in a booster that further accelerate electrons up to 2 or 2.4 GeV. Once reached the final energy, electrons are injected into the storage ring, where synchrotron light is generated.

Third generation synchrotron means that light is generated by the bending magnets used to deviate the electron in order to obtain a close trajectory as any other synchrotron, but also by *insertion devices* located in the storage ring straight sections. Insertion devices (wiggler or undulator) are rows of alternative N/S and S/N magnets placed up and above the electrons orbit (cfr. fig. 4), used to force the electrons to undulate and emit light also in the straight sections. Light emitted by insertion devices is peaked around an energy value, and this can be changed varying the gap between the two rows of magnets. The relatively low energy dispersion of insertion devices light makes these sources extremely brilliant, up to 5 order of magnitude higher with respect to bending magnets.

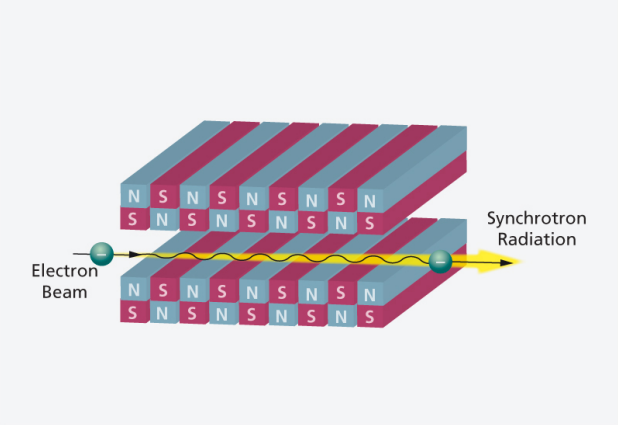

FIGURE 4: Scheme of an insertion device

Once light is produced, a series of mirrors provide to focalise it on a monochromator. Here a grating disperse light on the basis of its energy, allowing a small portion of monochromatic beam pass through the exit slits and, after a refocalising optic, impinge on the sample.

Synchrotron light present many advantages over light produced by conventional laboratory sources:

- Possibility to tune finely the photon energy. Changing the photon energy allows to explore different aspects of a system (e.g. distinguish between bulk and surface effects or minimize/maximize cross section of a certain process), but a fine tuning is a requirement of certain experimental techniques, like NEXAFS or ResPES.
- Grater resolution and higher photon flux, but also the possibility to adjust case by case the resolution sacrificing photon flux and vice versa.
- Defined (and in some cases variable) polarization direction. Linearly polarized light is fundamental were geometry effects are investigated, while the possibility to have circular polarized light allows to make easily experiments on magnetism.
- Small excitation spot, allowing to work with small or inhomogeneous samples.

1

Ultrafast charge transfer in Zn-Tetraphenyl Porphyrin and nanostructured ZnO interface: a resonant photoemission study

As stated in the first chapter, substituting the today's dyes used in DSSCs with ruthenium-free molecules is mandatory if we want this technology to spread out. The main factor that make Ru-based dyes extremely efficient is the metal to ligand charge transfer, that give rise to long living excited states.

However, many organometallic molecules share the metal to ligand charge transfer feature, and among them porphyrins seem to be the nature's choice. Many molecules of biological interest (e.g. chlorophylls, vitamin B-12, heme) share a metallo-porphyrine as functional core. We have now to understand if it is possible to substitute the Ru-based dyes with this class of molecules maintaining an acceptable efficiency.

In a DSSC light harvesting and charge generation at the electrodes occur in four steps:

1. Photon absorption and excitation of the dye molecule
2. Charge transfer from the excited molecule to the oxide substrate
3. Dye regeneration from the electrolytic solution
4. Charges migration to the electrode

The overall efficiency of the device is the product of the efficiency of each single step.

In this paper we investigated by mean of Resonant Photoemission Spectroscopy (ResPES) the process of charge transfer form Zinc Tetra Phenyl Porphyrine (Zn-TPP) to a nano-structured ZnO substrate. Results indicate that the charge transfer time is below the femtosecond time scale, one or two order of magnitude lower with respect to Ru-based dyes on TiO_2 [21–23]. These results encourage future research on this systems, especially for what concern dye regeneration.

Ultrafast charge transfer in Zn-Tetraphenyl Porphyrin and nanostructured ZnO interface: a resonant photoemission study

M. Caputo[1]*, B. A. Taleatu[1,2], C. Castellarin-Cudia[1,3], G. Di Santo[1], M. Panighel[1], L. Floreano[3], A. Goldoni[1]

[1] Elettra Sincrotrone Trieste, s.s. 14 km 163.5 in Area Science Park, 34149 Trieste, Italy
[2] Department of Physics, Obafemi Awolowo University, Ile-Ife 220005 Nigeria, and International Centre for Theoretical Physics, Strada Costiera 11, 34151 Trieste, Italy
[3] CNR-IOM, Lab. TASC, s.s. 14 km 163,5 in Area Science Park, 34149 Trieste, Italy

Abstract

Charge injection throughout the organic/inorganic interface is a key point for Dye Sensitized Solar Cells (DSSCs). This extremely fast (fs scale or lower) process is still not well understood due to the limitation imposed by the laser pulse duration in commonly used pump – probe experiments. Here we propose a Resonant Photoemission (ResPES) study of charge injection dynamic in Zinc Tetra Phenyl Porphyrin (Zn-TPP) adsorbed on a nanostructured ZnO substrate. Results indicate a faster charge transfer with respect to the widely used Ru-based dyes on TiO_2 substrate, but also with respect to the same molecules on TiO_2. This underlines the equivalence of porphyrins and Ru-based dyes, highlighting the benefits driven by a nanostructured substrate.

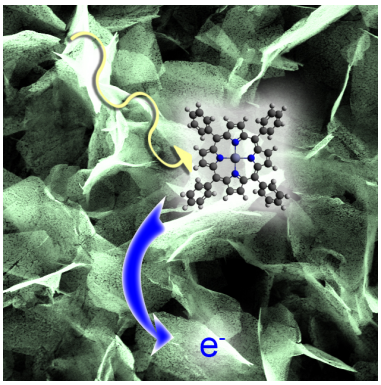

The need of a more sustainable economic development is leading the research of new energy resources. Today's efforts of the scientific community is being focused in finding cheaper alternatives to the classical crystalline silicon-based photovoltaic technology[1,2].

The most promising silicon alternative in term of cost reduction are the Dye Sensitized Solar Cells (DSSC), built for the first time by Michael Grätzel[3]. In these devices a wide band-gap semiconductor hole-blocking layer (generally TiO_2 or ZnO) is sensitized to the visible light by means of a dye. The dye absorbs a photon, transfers the excited electron into the conduction band of the semiconductor, and then it is regenerated by redox species in solution. The overall cell efficiency is the product of the efficiency of every single step: 1 – Dye excitation, 2 – Electron injection, 3 – Dye regeneration, 4 – hole and electron transport. So far the best efficiency reported for this type of solar cells[4] is 10.4% for ruthenium-based dyes, that is not so distant from commercial available amorphous silicon cells. Unfortunately, ruthenium is one of the rarest elements on the earth, making Ru-based dyes very expensive. In order to start a mass production of DSSCs, a cheaper substitutive has to be found. Among the possible dyes, the porphyrin group is the most promising.

Porphyrins are the fundamental building block of chlorophylls, heme, and many other biological molecules. Four pyrrolic units interconnected by four meso-carbon atoms compose porphine, which is the core of all the porphyrins. Different porphyrins can show very different physical and chemical properties thanks to the extreme flexibility of the porphine core, called macrocycle. This can bind several functional groups in its *meso*-position, and in addiction it can host several metals in the macrocycle center, coordinated to the four nitrogen atoms[5]. Porphyrins flexibility allows tailoring many interesting properties. Changing the host metal may cause energy shifts of the molecular orbitals and consequently of the absorption wavelength[6,7]. Moreover, the ability to bind different types of functional groups allows the control of fundamental parameters in the adsorption geometry, like macrocycle – substrate and macrocycle – macrocycle distance[8–11].

The flexibility of this system, along with the efficient light harvesting capabilities, makes these molecules a suitable choice for many nano-electronic devices like photo-inducible energy or electron transfer systems, light-harvesting arrays for solar cells, and nonlinear optics[12,13]. However, charge transfer on organic/inorganic interface is a key parameter that is still not well understood. Although many studies on electron injection of different porphyrins on different substrates are available[8,14–17], a good explanation of the physics underlying the process is still lacking. In fact the widely used pump-probe experiments are unable to resolve the extremely fast processes (<100 fs) that occur at the interface, and the time limit set by these experiments is in the same order of magnitude of intramolecular charge recombination.

To overcome the limitation imposed by laser pulse duration we use Resonant PhotoEmission Spectroscopy (ResPES) studies, able to resolve sub-fs processes. This technique, analogue to two-photon photoemission, can determine the electron injection from the molecule to the substrate using the core-hole lifetime as a clock[18–20]. We will compare the differences in the resonant features of a multilayer of Zn-Tetraphenyl Porphyrin (Zn-TPP) (Fig. 1) and for a monolayer deposited on nanostructured Zinc Oxide (ZnO). In both cases core electrons are excited into unoccupied molecular states by scanning the photon energy across the C1s absorption edge. The subsequent non-radiative decay takes place through Auger Core-Valence-Valence (CVV) process following different competitive paths. When the excited electron is directly involved in the core hole de-excitation (called participator decay or resonant photoemission), the final state contains a single hole in the Valence Band (VB). The corresponding resonant VB signal is much larger than that of direct VB photoemission because of the much larger cross-section at the core level ionization threshold. However, if the excited electron is transferred away from the excited molecule in a timescale comparable or faster than the core-hole lifetime, this decay channel is quenched. Comparing the resonating intensity of the participator decay between a thick molecular film (multilayer), whose purely van der Waals intermolecular coupling is not expected to change significantly the residence time, and a single molecular layer (which intensity may decrease due to a fast charge transfer to the substrate), it is possible to estimate the timescale of the electron transfer away from the molecule in the case of the coupled system. In this paper we will refer to the non-radiative decay channel as the only decay channel accessible to the system, which is a reasonable approximation for excitation on light elements such as carbon[21].

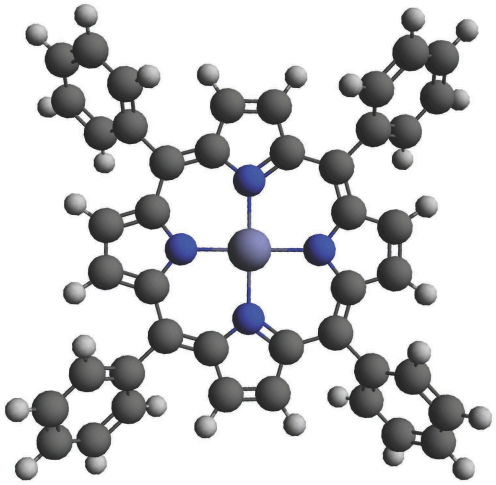

Fig. 1: Zn-TPP. The macrocycle with its four pyrrolic units bridged by four *meso*-carbon atoms and, attached to them, the four phenyl groups. In the centre the Zn host atom.

Figure 2 shows the ResPES spectra of a monolayer of Zn-TPP on the nanostructured ZnO surface after background and off-resonance spectrum subtraction. The ResPES spectra are presented by means of a 2D-map: on the X axis is reported the electron binding energy of the valence band, while on the Y axis is reported the photon

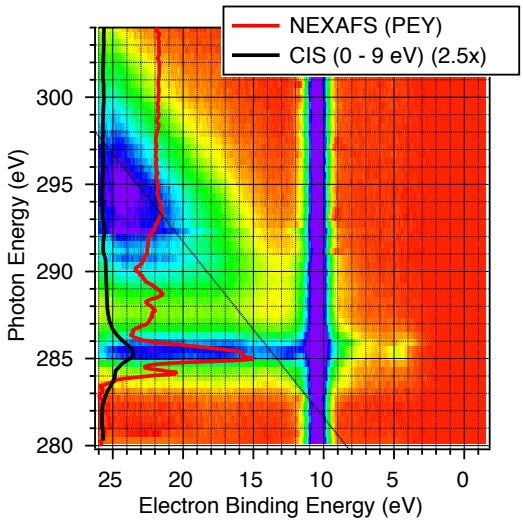

Fig. 2: ResPES map of a monolayer of Zn-TPP/ZnO after background and off-resonance spectrum subtraction. The black line is the CIS spectrum between 0-9 eV compared to the red NEXAFS spectrum. The diagonal line represents the linear dispersion in binding energy, i.e. constant kinetic energy.

energy used to acquire the spectrum. The intensity of the spectra is coded by colors, from red (lowest intensity) to violet (highest intensity). The strong feature visible at about 11 eV of binding energy is the Zn3d photoemission peak.

The map can be divided in two regions according to its dependence on the photon energy. The first region starts from $h\upsilon$=283 eV and ends at $h\upsilon$=291 eV: here the resonant photoemission contribution is evident from the *participant* and *spectator* decays. The final state of the *participant* process has one hole in the valence band, alike direct photoemission, so the emitted electrons have fixed binding energy. Also in the case of *spectator* decays, which final state has two holes in the valence band, the resonating peaks have a constant BE since they behave like an excited shake-up state of the valence band features. In fact the system decays through the recombination of the core-hole with an electron of the valence band, with the subsequent emission of another valence band electron, with the excited core electron still in the unoccupied state, e.g. the process leaves the system with two holes in the valence band and one excited electron in the previously unoccupied state. From $h\upsilon$=291 eV, when the core excitation is above the vacuum level, the Auger features start dispersing linearly in binding energy (i.e. they are constant in kinetic energy).

The spectra displayed on the left axis are the NEXAFS spectrum (red), proportional to the total decay channels, compared with the (black) Constant Initial State (CIS) spectrum. CIS spectra are photon energy dependent intensity of a particular binding energy-integrated region in the valence band. The CIS spectrum shown in Fig. 2 is integrated in the VB interval 0-9 eV. The comparison of the CIS spectra with those of the multilayer permits us to determine the fraction of electrons involved in the resonant decay channels in the monolayer on ZnO with respect to the total decay channels for each single unoccupied state. The choice of the CIS integration interval reflects the different nature of the decay channels. In the case shown in Fig. 3, mostly *participant* decay contributes for the 0-9 eV binding energy interval. Moreover, the omission of the Zn3d peak (11 eV binding energy) permits to exclude anti-resonating effects on this peak.

Similar analysis was performed also for a multilayer system obtaining spectra akin to the one published by Vilmercati et al[22]. Comparing the two CIS spectra, a strong quenching is visible for all the states in the monolayer system (Fig. 3), indicating that the charge transfer is faster than for the

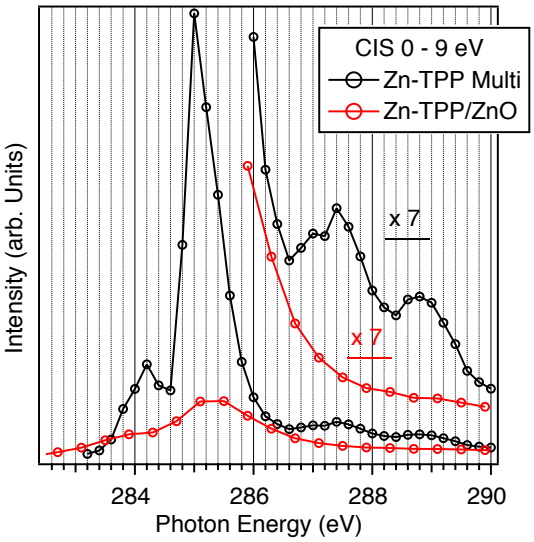

Fig. 3: Comparison between CIS 0-9 eV of Zn-TPP multilayer and one monolayer of Zn-TPP/ZnO. The region 286 – 289 eV of photon energy has been multiplied for a factor 7 and superimposed to underline the total quenching of the states in this region going from the multilayer to the monolayer system.

multilayer. In addition, a total quenching of the two absorption peaks at about 287.4 eV and 288.8 eV of photon energy is visible for the much coupled system (monolayer), indicating an extremely short charge transfer time scale of the excited electron in these states, as already seen for the interacting double-layer Zn-TPP/C_{70} on Si(111)[22]. The total absence of these resonant features simply imply that the electron is transferred away faster than the core – hole lifetime. Valence band resonances localized on both the excitations in the macrocycle and phenyl states, localized at ~284 eV and ~285.5 eV in the C1s absorption spectra, respectively[23], are still observed, meaning that the charge transfer timescale for these excited states is lower, but comparable, than the core-hole lifetime. In particular, the monolayer resonances on the phenyl molecular orbitals (~285.5 eV) display a relative quench stronger than on the macrocycle states (~284 eV). This indicates an overall more efficient charge transfer from the phenyl groups for the monolayer on ZnO, probably due to a more effective spatial overlap between the phenyl states and the conduction band of the ZnO surface.

The lineshape for these type of resonances is well described by the Fano's theory, taking in account the interference between the participator decay channel and the direct photoemission one:

$$I(E) = \frac{(q\Gamma/2 + E - E_{res})^2}{(\Gamma/2)^2 + (E - E_{res})^2}$$

where Γ represents the intrinsic resonance broadening and q is the asymmetry parameter representing the relative weight of the intensity contribution from participator decay with respect to the direct photoemission[24,25]. By fitting our CIS spectra with a Fano lineshape we can easily retrieve the resonance lifetime, which is equivalent to the charge transfer timescale. The values found for both macrocycle and phenyl states are in the low-10^{-16} s range that is about one order of magnitude less than the core hole lifetime in gas phase molecular systems[26] and multilayer of Zn-TPP[25] (between 3 and 6 fs).

To get a better insight in the process involving these low energy resonances, we took a closer look to each initial state after the core electron excitation by comparing the monolayer data with the Zn-TPP multilayer and with previous studies[22]. We performed a fit of the binding energy region 0-9 eV (that comprehends only *participant* decay) of all the valence bands acquired in order to de-convolve each feature and analyze them separately. The left inset of Fig. 4 shows, as an example, the fit performed on the monolayer valence band acquired with photon energy of 285.4 eV, where the resonant features are more intense. We used seven Gaussian functions, corresponding to seven different molecular states, allowing energy position and widths to vary in a small range moving from one spectrum to another (0.1 eV for both energy and width). Even if these degrees of freedom have no physical meaning they are necessary in order to group the complexity of the valence band in just seven peaks, nevertheless the resolution of the experiment does not allow any finer analysis. Similar fit can be done for the multilayer.

Plotting the intensity of each molecular state versus the photon energy for all the seven monolayer peaks, we can see that four of them show a resonant profile (shown in Fig. 4 and Fig. 5a for the monolayer and multilayer case respectively), while three states did not show any intensity dependence on the photon energy in either the monolayer or the multilayer, thus the latter ones were discarded from the following analysis. A comparison of the resonant states for multilayer and monolayer is shown in Fig. 5.

First of all, the occupied state at 3.8 eV resonates only on electron excitation on the phenyl orbitals. Considering that the electronic transitions need a certain degree of spatial overlap between the starting and the ending level, and considering the low superposition of the π electronic states between macrocycle and phenyl groups in metallo-

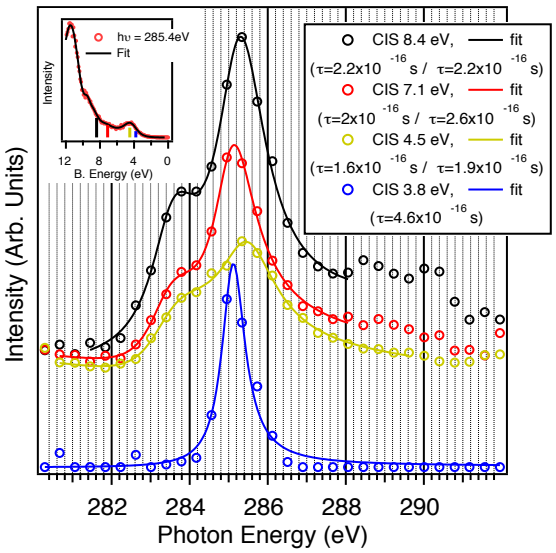

Fig. 4: Valence band peaks intensity (circle) and their fit (solid lines) using Fano profiles for the monolayer case. In the legend the excited states lifetime is reported for the resonance on the phenyl/macrocycle states. The inset shows the fit of the valence band acquired with a photon energy of 285.4 eV, the vertical bars represent the binding energy of the analysed CIS.

porphyrins[16,23,27], we can state that the occupied state at 3.8 eV is almost completely localized on the phenyl groups.

We also notice that the occupied state at 2.1 eV of binding energy, close to the Zn-TPP HOMO, is only resonating in the multilayer CIS (in correspondence of both the macrocycle and phenyl excitations), while no resonating intensity is detected in the monolayer CIS (Fig. 5f). For this decay process the charge transfer time can be just estimated in less than one order of magnitude lower than the core hole lifetime.

A summary of all the calculated decay time for the excited states for the monolayer case, and a comparison with the lifetime of the excited state in the multilayer case is given in Table 1.

		Zn-TPP Multi	Zn-TPP /ZnO
CIS 8.4 eV	Macrocycle	1.5 x 10^{-15} s	2.2 x 10^{-16} s
	Phenyl	2.4 x 10^{-15} s	2.2 x 10^{-16} s
CIS 7.1 eV	Macrocycle	1.5 x 10^{-15} s	2 x 10^{-16} s
	Phenyl	1.3 x 10^{-15} s	2.6 x 10^{-16} s
CIS 4.5 eV	Macrocycle	-	1.6 x 10^{-16} s
	Phenyl	2.1 x 10^{-15} s	1.9 x 10^{-16} s
CIS 3.8 eV	Macrocycle	-	-
	Phenyl	1.6 x 10^{-15} s	4.6 x 10^{-16} s
CIS 2.1 eV	Macrocycle	2.9 x 10^{-15} s	-
	Phenyl	1.4 x 10^{-15} s	-

Table 1: Decay time for the excited states in the multilayer and in the monolayer case

Our results indicate a charge transfer one order of magnitude faster with respect to the already known charge transfer dynamic for bi-isonicotinic acid[28,29] and the best efficient Ru-based "N3" dye ((cis-bis(isothiocyanato)bis(2,2'-bipyridyl-4,4'dicarboxylato)-ruthenium(II))[30] on rutile TiO_2(110) surface. Parallel studies performed on Zn-TPP on rutile TiO_2(110) surface indicate a slower charge transfer timescale[31], comparable to the one found for Ru-based dyes. This underlines that the better charge transfer timescale here reported is given by the effect of the nano-structure of the substrate probably related to the increase in charge separation efficiency in the presence of a space charge region on the surface of the nano-structures[32–35]. Moreover, it could be that the higher mobility of charge carriers in ZnO with respect to TiO_2 also contributes to the faster charge transfer timescale. We found that Zn-TPP/ZnO is a very efficient system in terms of charge injection, with a characteristic charge transfer time in the order of few 10^{-16} s for most of the π* states excited below 286 eV in the XAS spectra and even lower for higher energy excitations. This injection time is the

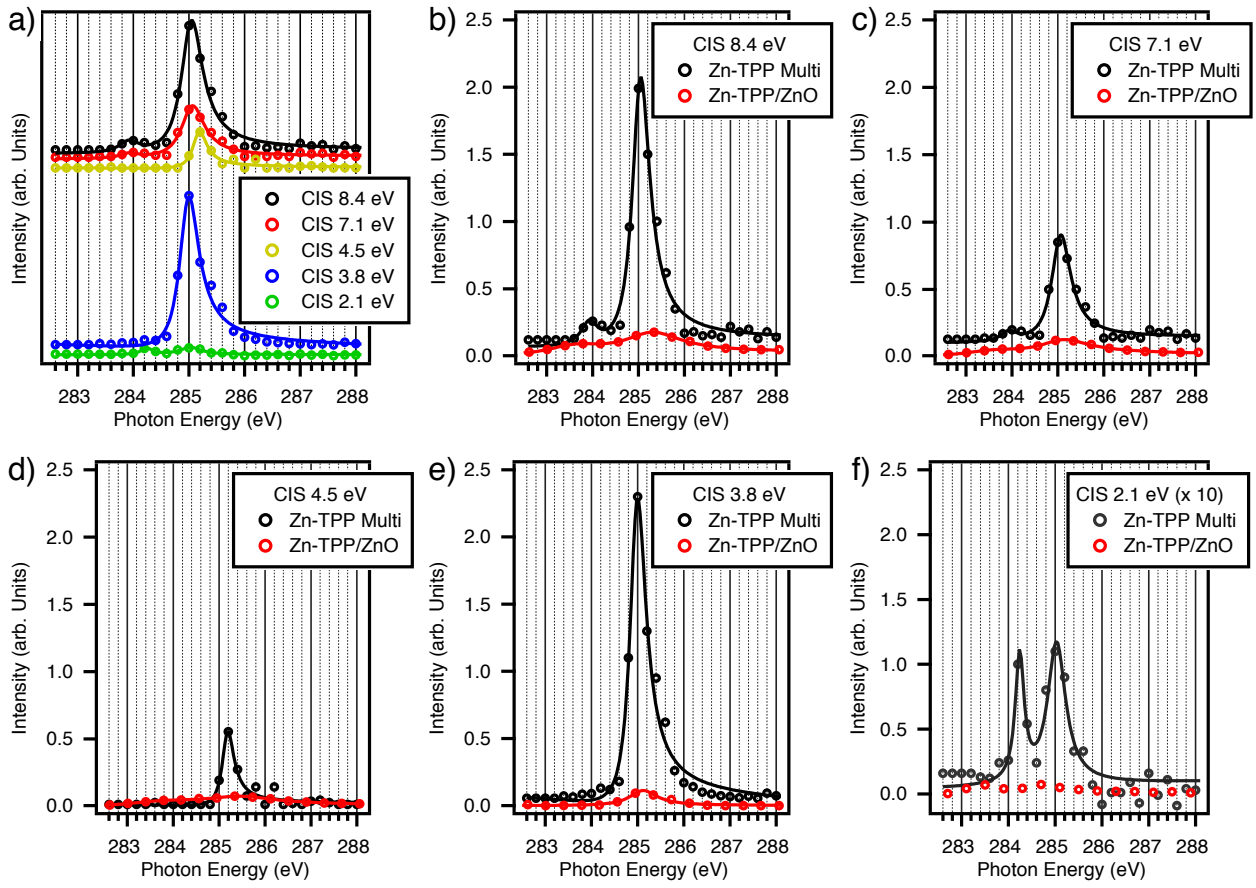

Fig. 5: a) Valence band peaks intensity (circle) and their fit (solid lines) using Fano profiles for the multilayer case. b) - f) Comparison between each analysed CIS of Zn-TPP multilayer and one monolayer of Zn-TPP/ZnO.

lowest reported so far, indicating that porphyrins are molecules capable of replacing the more expensive Ru-based dyes in terms of charge transfer performance. Resonant Photoemission allowed also a distinction between the charge injection from the macrocycle and the phenyl groups, indicating a more effective charge transfer from the latter in the case of one monolayer of Zn-TPP on ZnO with respect to both the multilayer system and the monolayer on TiO_2 single crystal.

The best charge transfer efficiency reported for this system is due to the substrate choice. While all the previous studies has been performed on TiO_2 single crystal surfaces, here a combination of a different oxide and nanostructuration of the surface has been performed. Further studies are requested to decouple the effect of nanstructuration from the charge transfer performance of a bare ZnO surface.

Supporting Information

Detailed experimental methods and SEM images of the nanostructured ZnO substrate used in this work are available free of charge via the Internet at http://pubs.acs.org.

References

(1) Peter, L. The Grätzel Cell: Where Next? *J. Phys. Chem. Lett.* **2011**, 1861–1867.

(2) Hardin, B. E.; Snaith, H. J.; McGehee, M. D. The Renaissance of Dye-Sensitized Solar Cells. *Nat. Photonics* **2012**, *6*, 162–169.

(3) O'Regan, B.; Grätzel, M. A Low-Cost, High-Efficiency Solar Cell Based on Dye-Sensitized Colloidal TiO2 Films. *Nature* **1991**, *353*, 737–740.

(4) Hagfeldt, A.; Grätzel, M. Molecular Photovoltaics. *Acc. Chem. Res.* **2000**, *33*, 269–277.

(5) Panighel, M.; Santo, G. Di; Caputo, M.; Lal, C.; Taleatu, B.; Goldoni, A. Review of 2H-Tetraphenylporphyrins Metalation in Ultra-High Vacuum on Metal Surfaces. *J. Phys. Conf. Ser.* **2013**, *470*, 012012.

(6) Liao, M.-S.; Scheiner, S. Electronic Structure and Bonding in Metal Porphyrins, metal=Fe, Co, Ni, Cu, Zn. *J. Chem. Phys.* **2002**, *117*, 205.

(7) Campbell, W. M.; Burrell, A. K.; Officer, D.; Jolley, K. W. Porphyrins as Light Harvesters in the Dye-Sensitised TiO2 Solar Cell. *Coord. Chem. Rev.* **2004**, *248*, 1363–1379.

(8) Rochford, J.; Chu, D.; Hagfeldt, A.; Galoppini, E. Tetrachelate Porphyrin Chromophores for Metal Oxide Semiconductor Sensitization: Effect of the Spacer Length and Anchoring Group Position. *J. Am. Chem. Soc.* **2007**, *129*, 4655–4665.

(9) Hoeben, F. J. M.; Jonkheijm, P.; Meijer, E. W.; Schenning, A. P. H. J. About Supramolecular Assemblies of Pi-Conjugated Systems. *Chem. Rev.* **2005**, *105*, 1491–1546.

(10) Drain, C. M.; Varotto, A.; Radivojevic, I. Self-Organized Porphyrinic Materials. *Chem. Rev.* **2009**, *109*, 1630–1658.

(11) Castellarin-Cudia, C.; Borghetti, P.; Di Santo, G.; Fanetti, M.; Larciprete, R.; Cepek, C.; Vilmercati, P.; Sangaletti, L.; Verdini, A.; Cossaro, A.; et al. Substrate Influence for the Zn-Tetraphenyl-Porphyrin Adsorption Geometry and the Interface-Induced Electron Transfer. *Chem. Phys. Phys. Chem.* **2010**, *11*, 2248–2255.

(12) Vilmercati, P.; Castellarin-Cudia, C.; Gebauer, R.; Ghosh, P.; Lizzit, S.; Petaccia, L.; Cepek, C.; Larciprete, R.; Verdini, A.; Floreano, L.; et al. Mesoscopic Donor-Acceptor Multilayer by Ultrahigh-Vacuum Codeposition of Zn-Tetraphenyl-Porphyrin and C70. *J. Am. Chem. Soc.* **2009**, *131*, 644–652.

(13) Cho, H. S.; Jeong, D. H.; Cho, S.; Kim, D.; Matsuzaki, Y.; Tanaka, K.; Tsuda, A.; Osuka, A. Photophysical Properties of Porphyrin Tapes. *J. Am. Chem. Soc.* **2002**, *124*, 14642–14654.

(14) Tachibana, Y.; Haque, S. a.; Mercer, I. P.; Durrant, J. R.; Klug, D. R. Electron Injection and Recombination in Dye Sensitized Nanocrystalline Titanium Dioxide Films: A Comparison of Ruthenium Bipyridyl and Porphyrin Sensitizer Dyes. *J. Phys. Chem. B* **2000**, *104*, 1198–1205.

(15) Santos, T. Dos; Morandeira, A.; Koops, S.; Mozer, A. J.; Tsekouras, G.; Dong, Y.; Wagner, P.; Wallace, G.; Earles, J. C.; Gordon, K. C.; et al. Injection Limitations in a Series of Porphyrin Dye-Sensitized Solar Cells. *J. Phys. Chem. C* **2010**, *114*, 3276–3279.

(16) Rochford, J.; Galoppini, E. Zinc(II) Tetraarylporphyrins Anchored to TiO2, ZnO, and ZrO2 Nanoparticle Films through Rigid-Rod Linkers. *Langmuir* **2008**, *24*, 5366–5374.

(17) Campbell, W. M.; Jolley, K. W. Highly Efficient Porphyrin Sensitizers for Dye-Sensitized Solar Cells. *J. Phys. Chem. C* **2007**, *36*, 11760–11762.

(18) Brühwiler, P. A.; Karis, O.; Martensson, N. Charge-Transfer Dynamics Studied Using Resonant Core Spectroscopies. *Rev. Mod. Phys.* **2002**, *74*, 703–740.

(19) Menzel, D. Ultrafast Charge Transfer at Surfaces Accessed by Core Electron Spectroscopies. *Chem. Soc. Rev.* **2008**, *37*, 2212–2223.

(20) Vilmercati, P.; Cvetko, D.; Cossaro, A.; Morgante, A. Heterostructured Organic Interfaces Probed by Resonant Photoemission. *Surf. Sci.* **2009**, *603*, 1542–1556.

(21) Keski-Rahkonen, O.; Krause, M. O. Total and Partial Atomic-Level Widths. *Atomic Data and Nuclear Data Tables*, 1974, *14*, 139–146.

(22) Vilmercati, P.; Castellarin-Cudia, C.; Larciprete, R.; Cepek, C.; Zampieri, G.; Sangaletti, L.; Pagliara, S.; Verdini, A.; Cossaro, A.; Floreano, L.; et al. Molecular Orientations, Electronic Properties and Charge Transfer Timescale in a Zn-porphyrin/C70 Donor–acceptor Complex for Solar Cells. *Surf. Sci.* **2006**, *600*, 4018–4023.

(23) Castellarin-Cudia, C.; Vilmercati, P.; Larciprete, R.; Cepek, C.; Zampieri, G.; Sangaletti, L.; Pagliara, S.; Verdini, A.; Cossaro, A.; Floreano, L.; et al. Electronic Structure and Molecular Orientation of a Zn-Tetra-Phenyl Porphyrin Multilayer on Si(111). *Surf. Sci.* **2006**, *600*, 4013–4017.

(24) Fano, U. Effects of Configuration Interaction on Intensities and Phase Shifts. *Phys. Rev.* **1961**.

(25) Weinelt, M.; Nilsson, A.; Magnuson, M. Resonant Photoemission at the 2p Edges of Ni: Resonant Raman and Interference Effects. *Phys. Rev. Lett.* **1997**, 967–970.

(26) Coville, M.; Thomas, T. Molecular Effects on Inner-Shell Lifetimes: Possible Test of the One-Center Model of Auger Decay. *Phys. Rev. A* **1991**, *43*, 6053–6056.

(27) Rangan, S.; Katalinic, S.; Thorpe, R.; Bartynski, R. A.; Rochford, J.; Galoppini, E. Energy Level Alignment of a Zinc (II) Tetraphenylporphyrin Dye Adsorbed onto TiO2 (110) and ZnO (1120) Surfaces. *J. Phys. Chem. C* **2010**, *2*, 1139–1147.

(28) Schnadt, J.; Brühwiler, P. A.; Patthey, L.; O'Shea, J. N.; Södergren, S.; Odelius, M.; Ahuja, R.; Olof, K.; Bässler, M.; Persson, P.; et al. Experimental Evidence for Sub-3-Fs Charge Transfer from an Aromatic Adsorbate to a Semiconductor. *Nature* **2002**, *418*, 620–623.

(29) Schnadt, J.; O'Shea, J. N.; Patthey, L.; Kjeldgaard, L.; Åhlund, J.; Nilson, K.; Schiessling, J.; Krempaský, J.; Shi, M.; Karis, O.; et al. Excited-State Charge Transfer Dynamics in Systems of Aromatic Adsorbates on TiO[sub 2] Studied with Resonant Core Techniques. *J. Chem. Phys.* **2003**, *119*, 12462.

(30) Mayor, L. C.; Ben Taylor, J.; Magnano, G.; Rienzo, A.; Satterley, C. J.; O'Shea, J. N.; Schnadt, J. Photoemission, Resonant Photoemission, and X-Ray Absorption of a Ru(II) Complex Adsorbed on Rutile TiO2(110) Prepared by in Situ Electrospray Deposition. *J. Chem. Phys.* **2008**, *129*, 114701.

(31) Vilmercati, P. Ultra-Fast Charge Transfer Dynamic in Thin and Ultra-Thin Films of Organics Studied with Synchrotron Radiation., PhD thesis University of Trieste 2008.

(32) Mora-Seró, I.; Fabregat-Santiago, F.; Denier, B.; Bisquert, J.; Tena-Zaera, R.; Elias, J.; Lévy-Clément, C. Determination of Carrier Density of ZnO Nanowires by Electrochemical Techniques. *Appl. Phys. Lett.* **2006**, *89*, 203117.

(33) Galoppini, E.; Rochford, J.; Chen, H.; Saraf, G.; Lu, Y.; Hagfeldt, A.; Boschloo, G. Fast Electron Transport in Metal Organic Vapor Deposition Grown Dye-Sensitized ZnO Nanorod Solar Cells. *J. Phys. Chem. B* **2006**, *110*, 16159–16161.

(34) Stockwell, D.; Yang, Y.; Huang, J. Comparison of Electron-Transfer Dynamics from Coumarin 343 to TiO2, SnO2, and ZnO Nanocrystalline Thin Films: Role of Interface-Bound Charge-Separated Pairs. *J. Phys. Chem. C* **2010**, 6560–6566.

(35) Law, M.; Greene, L. E.; Johnson, J. C.; Saykally, R.; Yang, P. Nanowire Dye-Sensitized Solar Cells. *Nat. Mater.* **2005**, *4*, 455–459.

Ultrafast charge transfer in Zn-Tetraphenyl Porphyrin and nanostructured ZnO interface: a resonant photoemission study

M. Caputo[1]*, B. A. Taleatu[1,2], C. Castellarin-Cudia[1,3], G. Di Santo[1], M. Panighel[1], L. Floreano[3], A. Goldoni[1]

Supporting Information

Nanostructured ZnO was grown *ex-situ* on a ITO/glass substrate by electro-chemical deposition as described elsewhere[1]. Scanning Electron Microscope (SEM) images of the sample used here is shown in Fig. S1. Zn-TPP were purchased by Sigma Aldrich and sublimated in Ultra High Vacuum (UHV) from a well outgassed boron nitride crucible keeping the substrate at room temperature.

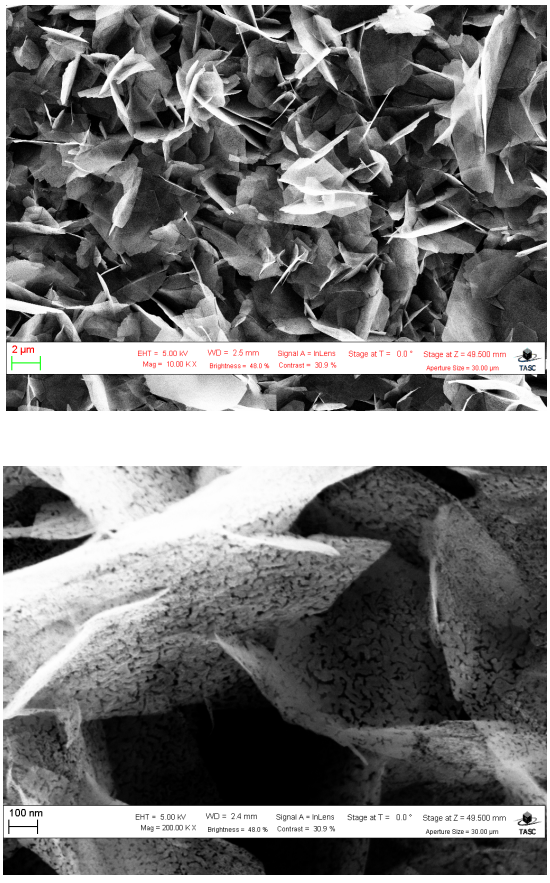

Fig. S1: SEM images of the nanostructured ZnO surface used.

Surface cleanness and film coverage was checked by XPS. The substrate surface has been cleaned annealing the sample in oxygen until negligible carbon signal could be detected. One monolayer of Zn-TPP has been obtained sublimating a thick film of molecule on the surface and then annealing the sample at 285°C. At this temperature, higher than the sublimation temperature of Zn-TPP in vacuum, the molecules kept together by van der Waals force (i.e. the multilayer) leave the sample and only the first layer remains on the surface thanks to the stronger bonding with the substrate.

The measurements were performed at the ALOISA beamline of Elettra synchrotron[2] in a base pressure of about 10^{-10} mbar with linear light polarization at 45° from the sample surface. Single valence band spectra for ResPES were collected with an overall resolution of 215 meV and the photon energy was scanned across the carbon absorption energy with step of 200 meV. NEXAFS spectra, instead, were acquired

in Partial Electron Yield mode with a resolution of 80 meV and a photon energy step of 50 meV.

The raw valence band spectra of the monolayer and multilayer data sets were treated with the same procedures. They were first aligned to the Zn3d photoemission peak in order to remove any charging effect, and then normalized to the photon flux monitored by a NEXAFS spectrum on a clean substrate. For each spectrum a Shirley-type background was subtracted, along with an off-resonance spectrum acquired below the absorption threshold with photon energy of $h\upsilon$=280 eV. The latter process permits a direct and clear visualization of the resonances.

References

(1) Taleatu, B.; Fasasi, a. Y.; Di Santo, G.; Bernstorff, S.; Goldoni, A.; Fanetti, M.; Floreano, L.; Borghetti, P.; Casalis, L.; Sanavio, B.; et al. Electro-Chemical Deposition of Zinc Oxide Nanostructures by Using Two Electrodes. *AIP Adv.* **2011**, *1*, 032147.

(2) Floreano, L.; Naletto, G.; Cvetko, D.; Gotter, R.; Malvezzi, M.; Marassi, L.; Morgante, a.; Santaniello, a.; Verdini, a.; Tommasini, F.; et al. Performance of the Grating-Crystal Monochromator of the ALOISA Beamline at the Elettra Synchrotron. *Rev. Sci. Instrum.* **1999**, *70*, 3855.

2

Solid state effects on the electronic structure of H_2OEP

A fundamental parameter for solar cells is the absorber bandgap. It determines the lowest photon energy necessary to excite the systems and the maximum voltage the cell can provide, hence the thermodynamic efficiency limit [24]. Moving from crystalline inorganic materials to molecular absorber, the bandgap becomes sensible to many factors, as screening, molecular distortions, Jahn-Teller effect and so on. Knowing and controlling these effects can result in further chances of tailoring light absorptions.

In this paper we investigated the solid state effect in the electronic structure of occupied and unoccupied states of Octa Ethyl Porphyrins (H_2OEP) by mean of Photoemission Spectroscopy (PES), Inverse Photoemission Spectroscopy (IPES), X-ray Absorption Spectroscpy (XAS) and ab-initio electronic structure calculations both in gas and solid phase.

From experimental data it has been shown that going from single molecules (gas phase) to a crystal of H_2OEP causes a bandgap shrink, while the LUMO - LUMO+1 degeneracy is lifted. Thanks to theoretical calculations we can state that the gap shrinking is caused by the screening due to the other molecules, while the separation of LUMO - LUMO+1 is caused by a lowering of the molecular symmetry in the crystal packing.

PCCP

PAPER

View Article Online
View Journal | View Issue

Cite this: *Phys. Chem. Chem. Phys.*, 2014, **16**, 27104

Solid state effects on the electronic structure of H_2OEP†

M. Marsili,*[ab] P. Umari,[ac] G. Di Santo,[d] M. Caputo,[d] M. Panighel,[de] A. Goldoni,[d] M. Kumar[f] and M. Pedio[f]

Received 2nd August 2014,
Accepted 30th October 2014

DOI: 10.1039/c4cp03450c

www.rsc.org/pccp

We present the results of a joint experimental and theoretical investigation concerning the effect of crystal packing on the electronic properties of the H_2OEP molecule. Thin films, deposited in ultra high vacuum on metal surfaces, are investigated by combining valence band photoemission, inverse photoemission, and X-ray absorption spectroscopy. The spectra of the films are compared, when possible, with those measured in the gas phase. Once many-body effects are included in the calculations through the GW method, the electronic structure of H_2OEP in the film and gas phase are accurately reproduced for both valence and conduction states. Upon going from an isolated molecule to the film phase, the electronic gap shrinks significantly and the lowest unoccupied molecular orbital (LUMO) and LUMO + 1 degeneracy is removed. The calculations show that the reduction of the transport gap in the film is entirely addressable to the enhancement of the electronic screening.

1 Introduction

Porphyrins belong to a class of molecules that have been intensively studied for their importance in biology and natural processes.[1] From a technological point of view, there are possible applications in a variety of fields such as catalysis, optoelectronics and photovoltaics.[2–4] The application potentiality of this kind of molecules and their involvement in fundamental biological processes are due to the great diversity of functionalities that can be achieved by changing their building blocks, *i.e.* using different functional groups and/or metal centers.[5] Interestingly, in this way, it is possible to control not only the properties of a single molecule, but also how the molecules assemble and pack, thus tailoring, for instance, the crystal structure or the size of the void space between aggregates, and providing a further path for specific functionalization.[6,7] In view of the application of this kind of molecules in their solid state form, we study the effect of crystal packing on the electronic structure of H_2OEP, one of the simplest molecules of this class. The choice of this specific molecule among all other porphyrins is based on the fact that it presents a single crystalline phase, thus favoring the comparison between theoretical prediction and experimental results.

A direct and accurate determination of the electronic levels of molecular solids and films is extremely desirable for a variety of applications, as in optoelectronic, catalytic or magnetic systems. Combined valence-band photoemission (PES) and inverse photoemission (IPS) spectroscopy studies allow the direct determination of the relevant transport levels.[8,9] This kind of studies has been applied to the determination of the electronic structures of several organic films made of phthalocyanines,[8,10–13] perylene derivatives (PTCDA),[8,13–15] Alq3 (aluminum tris-8-hydroxyquinoline),[12,13] fullerenes,[16] bithiophene,[17] and α-NPD (*N*,*N*′-diphenyl-*N*,*N*′-bis(1-naphthyl)-1,1′-biphenyl-4,4″-diamine)[12] films. A few PES-IPS studies on porphyrin films are reported;[18–21] in these studies the interaction of the molecules with the different substrates they were grown on was studied in detail. However, the effect of crystal packing was not analyzed, and there are no studies, to the best of our knowledge, in which both the valence and conduction bands of porphyrin films have been theoretically addressed, with the inclusion of many-body effects, in comparison with the experimental data.

The electronic structure of the H_2OEP molecule has been extensively studied in its gas phase.[22] For the isolated molecule, experimental and theoretical density of occupied states was determined.[23] Therefore we employ direct and inverse photoemission spectroscopy as well as near-edge X-ray absorption fine-structure (NEXAFS) spectroscopy to probe directly the density of occupied and unoccupied electronic levels of H_2OEP thin films

[a] *Dipartimento di Fisica e Astronomia, Universitá di Padova, via Marzolo 8, Padova 35131, Italy. E-mail: margherita.marsili@nano.cnr.it; Fax: +39 049 8277102; Tel: +39 049 8277174*
[b] *S3, Istituto Nanoscienze-CNR, Via Campi 213/A, 41125 Modena, Italy*
[c] *IOM-CNR, Theory@Elettra group, Trieste, Italy*
[d] *Elettra - Sincrotrone Trieste, s.s. 14 km 163.5 in Area Science Park, Basovizza (Trieste) 34149, Italy*
[e] *Department of Physics, University of Trieste, via Valerio 2, Trieste 34100, Italy*
[f] *IOM-CNR, TASC Area Science Park Buil. MM, S.S. 14, Km 163.5, Basovizza (Trieste) 34149, Italy*

† Electronic supplementary information (ESI) available: DFT and GW band structures. See DOI: 10.1039/c4cp03450c

grown on metal substrates. The experimental spectra are then analyzed and compared with the results of state-of-the-art *ab initio* electronic structure calculations based on many-body perturbation theory (MBPT) through the GW method. We have found that the GW method can accurately reproduce the experimental spectra for both the gas and the solid phases. This allows us to trace the origin of the band gap reduction observed for thin films.

The paper is organized as follows: in Section 2 the experimental and theoretical methods are addressed; in Section 3 we present and discuss the results concerning the geometry and the electronic structure of H_2OEP, comparing gas and solid state phases; in Section 4 the conclusions are drawn.

2 Methods

2.1 Experimental

All the experiments were performed in ultra-high vacuum (UHV) experimental chambers at a base pressure greater than 10^{-10} mbar. Highly purified (99%) commercial H_2OEP was used and sublimated at 520 K using a homemade, resistively heated Ta evaporator. The H_2OEP multilayer films were deposited in UHV on a clean Ag(111) substrate of 1 to 40 nm thickness. The H_2OEP films were characterized *ex situ* by X-ray diffraction (XRD), which confirmed the triclinic structure of the film in good agreement with reported X-ray studies.[24,25]

The measurements relative to H_2OEP molecules in gas phase were carried out at the gas phase beamline at Elettra using a 150 mm hemispherical electron energy analyzer. The valence band spectrum of H_2OEP was collected with an incident photon energy of 120 eV and an overall energy resolution (photons + analyzer) of 0.20 eV. The energy scale was calibrated using, by reference, the water spectrum. NEXAFS spectra at the N 1s threshold were collected in partial electron yield mode and the energy scales were calibrated by introducing N_2 in the chamber, collecting a N_2 molecule spectrum, and using the N_2 reference value to align the energies.

The valence band photoemission data for a multilayer film (evaporated on a clean Ag(111) substrate) were collected at the Micro Nano Carbon laboratory by means of a VG 150 hemispherical electron energy analyzer in normal emission using He I radiation (21.22 eV) with an energy resolution of 0.1 eV. The binding energies of the photoemission spectra were calibrated using the Fermi level of Ag(111). The NEXAFS spectra at the N 1s threshold for the multilayer film were collected at the BACH beamline and are already reported in ref. 26.

The angle resolved inverse photoemission (IPS) measurements at normal incidence were performed at the SIPE-TASC laboratory using a homemade Erdman-Zipf electron gun. The electron beam divergence was better than 3°. Photons emitted from the sample surface were collected by a homemade Geiger–Mueller type detector with a He–I_2 gas mixture and a SrF_2 entrance window filtering photons at a $h\nu$ = 9.5 eV energy. The experimental resolution was $\lesssim$350 meV, as measured by the Fermi level onset of clean Ta foil which was frequently interchanged with the sample. In order to prevent degradation of the molecular film, the beam current density was limited to 8×10^{-7} A cm^{-2}. No charging was detected during acquisition. Damage produced by the electron beam has been found after 1 hour of IPS acquisition. To further reduce the degradation of the molecular film during measurements, the spectra were acquired on different samples, prepared in the same way, and at various sample locations, changed after about 20 minutes of acquisition. The single scans were numerically summed subsequently. The IPS spectra shown in this paper are taken on a H_2OEP film whose thickness was about 5 nm, the value beyond which no further band shift was detectable.

2.2 Theoretical

The accurate first-principles determination of the electronic density of states (DOS) of the H_2OEP molecule and film is achieved in a two step procedure: (i) the ground state equilibrium geometry is obtained within density-functional theory (DFT); (ii) the single particle excitation energies of the system are addressed within MBPT employing the GW method.

In the following, we will provide a brief overview of the latter method which is extensively reviewed in ref. 27 and 28.

The GW method. Within MBPT, it can be shown that the poles of the single-particle Green's function are found at frequencies that correspond to the charged excitation energies of the electronic system. The GW method allows for an accurate determination of the poles of the single particle Green's function, thus providing a reliable estimation of the electronic DOS as probed by PE.

In the frequency domain, the single particle Green's function can be expressed as

$$G(\mathbf{r},\mathbf{r}';\omega) = \sum_{\mathrm{nk}} \frac{\psi_{\mathrm{nk}}(\mathbf{r},\omega)\tilde{\psi}_{\mathrm{nk}}{}^{*}(\mathbf{r}',\omega)}{\omega - \varepsilon_{\mathrm{nk}}(\omega)} \tag{1}$$

where $\varepsilon_{\mathrm{nk}}(\omega)$ and $\psi_{\mathrm{nk}}(\boldsymbol{r},\omega)$ are solution of the equation

$$\left[-\frac{\nabla^2}{2} + v_{\mathrm{ext}}(\mathbf{r}) + v_{\mathrm{H}}(\mathbf{r})\right]\psi_{\mathrm{nk}}(\mathbf{r},\omega) + \int \mathrm{d}\mathbf{r}'\Sigma(\mathbf{r},\mathbf{r}';\omega)\psi_{\mathrm{nk}}(\mathbf{r}',\omega) = \varepsilon_{\mathrm{nk}}(\omega)\psi_{\mathrm{nk}}(\mathbf{r},\omega) \tag{2}$$

Here v_{ext} is the external ionic potential, v_{H} is the Hartree potential, Σ is the electronic self-energy, and n and k are the band and k-point indices respectively. All quantities are expressed in atomic units (a.u.). The poles of the Green's function are found at the quasiparticle energies ω_{QP}, that obey the relation $\omega_{\mathrm{nk}}^{\mathrm{QP}} = \varepsilon_{\mathrm{nk}}(\omega_{\mathrm{nk}}^{\mathrm{QP}})$.

In order to solve eqn (2), and to find the quasiparticle energies, an expression for Σ must be provided. A good approximation, that can be derived within the MBPT framework, is the so-called GW approximation, where the electronic self-energy is given, in the time domain, by the simple product of the single particle Green's function G and the screened Coulomb interaction W, *i.e.* $\Sigma(1,2) = iG(1,2)W(1^+,2)$, where $1^+ = (r_1, t_1 + \eta)$ and η is an infinitesimal positive number.

The screened Coulomb interaction can be expressed in terms of the reducible polarizability P as $W(1,2) = v(1,2) + \int \mathrm{d}3\mathrm{d}4 v(1,3)P(3,4)v(4,2) = v(1,2) + W_c(1,2)$, where $v(1,2)$ is the

bare Coulomb potential. The last relation defines W_c, which is the frequency dependent part of the screened interaction. Thus Σ can be expressed as the sum of an exchange term, $\Sigma_x(1,2) = iG(1,2)v(1^+,2)$, and of a correlation term, $\Sigma_c(1,2) = iG(1,2)W_c(1^+,2)$. By neglecting Σ_c, the Hartree–Fock picture is recovered.

Besides using an approximate form for Σ, in actual calculations further approximations are carried out. In this work we employ the so-called G_0W_0 approximation, where the single particle Green's function, entering in the expression of Σ, is the non-interacting DFT Kohn Sham (KS) Green's function; the electronic screening is built, at the RPA level, employing KS energies and wavefunctions; and the $\psi_{nk}(r,\omega)$, in the quasiparticle eqn (2), are approximated by the KS states.

The frequency dependence of the screening is fully taken into account in our calculations. In order to carry out this task, Σ_c is evaluated along the imaginary frequency axis and then analytically continued across the real axis[29,30] after fitting $\Sigma_c(i\omega)$ with a multipole function. Another possible approach is the so-called contour deformation method.[31,32] Within this method the integrals along the real frequency axis are evaluated in terms of integrals over the imaginary axis plus a summation over poles; in this way the fitting procedure is avoided. The contour deformation method is very accurate but extremely demanding from a computational point of view. We employed it to compute the energy levels close to the highest occupied molecular orbital (HOMO)–LUMO levels, and to optimize the fit parameters of the analytic continuation method.

We compare the calculated DOS directly with experimental spectra neglecting matrix-element effects. Usually this approximation leads to good agreement with experiments.[23]

Computational details. The DFT calculations were performed using the Quantum ESPRESSO package.[33] Norm-conserving pseudopotentials and the PBE[34] exchange–correlation functional were used throughout the calculations. The energy cutoff for the plane-wave expansion of the wavefunctions was set to 45 Ry. The Brillouin zone of the crystal was sampled at the Γ point.

For the crystal phase, the experimental lattice parameters were used;[24] the relaxation of the atomic positions ended when all components of all forces were smaller than 1×10^{-4} a.u. The starting atomic coordinates within the crystal cell were obtained from ref. 24 and then the system was allowed to fully relax.

The GW calculations were performed using the GWL code within the Quantum ESPRESSO package.[33] In the isolated case the calculations were carried out using an orthorhombic cell of $(25 \times 25 \times 12)$ Å^3. In order to avoid spurious interaction between periodic replicas, we employed a 10 Å radius spherical cutoff for the Coulomb interaction. In both the isolated case and the crystal phase, following the notation of ref. 35, we employed an $E^* = 5$ Ry cutoff to build the optimal polarizability basis set, which we chose to be made of 2000 elements. This choice corresponds to a polarizability eigenvalue threshold of $q^* = 42$ Bohr^3 $= 8 \times 10^{-4}$ Ω for the isolated case, and $q^* = 4.4$ Bohr^3 $= 9 \times 10^{-4}$ Ω for the crystal phase calculations (here Ω is the unit cell volume of each calculation). The overall convergence for the determination of the levels close to the HOMO and LUMO is $\sim$0.1 eV.

3 Results and discussion

Once organic molecules pack forming a molecular crystal, the geometry of each molecule becomes distorted with respect to the gas phase and, at the same time, the electronic properties of the system drastically change.[36–41] Such change may be an effect of the geometric distortion and/or due to modifications in the electronic screening, more effective in a 3D system. In the following section the results concerning the ground-state geometry and the electronic properties of the H_2OEP molecule and film are presented and discussed.

3.1 Geometry

In the H_2OEP molecule, eight ethyl groups are attached to the β carbon atoms of the porphine pyrrole rings,[42] as shown in Fig. 1. In the gas phase, the carbon skeleton of the molecule is essentially planar, and the deviation of the calculated coordinates from the mean plane is less than 10^{-4} Å for the macrocycle atoms.

H_2OEP crystallizes in a triclinic lattice with one molecule per unit cell. As our calculation scheme does not involve van der Waals corrections, we employed the experimental lattice structure parameters taken from ref. 24, namely, $a = 9.791$ Å, $b = 10.771$ Å, $c = 7.483$ Å, $\alpha = 97.43^\circ$, $\beta = 106.85^\circ$, and $\gamma = 93.25^\circ$.

As common for other porphyrin aggregates, within the crystal the H_2OEP molecules are arranged with parallel π systems, no relative rotation, and a finite center-to-center offset. The extent of such offset is determined by the interplay between van der Waals attraction and electrostatic repulsion.[43] At odds with the gas phase geometry, within the crystal, the ethyl groups of each molecule are oriented almost perpendicularly with respect to the average macrocycle plane. Two subsequent phenyl groups stick inward of the macrocycle plane and the remaining subsequent two outwards. This is a typical geometry for the triclinic arrangement of this class of molecules.[44]

In Fig. 2 the final geometry of the molecule in the triclinic phase is shown, together with the macrocycle bond lengths

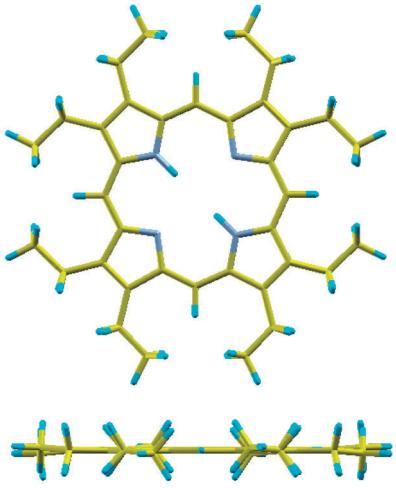

Fig. 1 Equilibrium geometry of the isolated molecule. Carbon atoms in yellow, hydrogen atoms in cyan, and nitrogen atoms in light blue. Top figure: top view; bottom figure: side view.

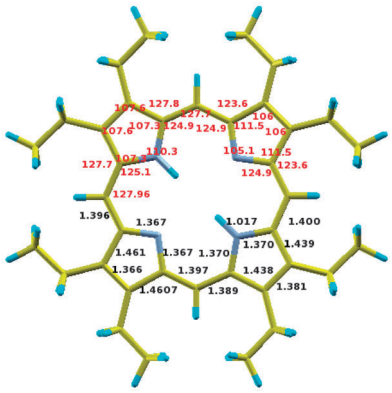

Fig. 2 Geometry of the single H_2OEP molecule within the crystal.

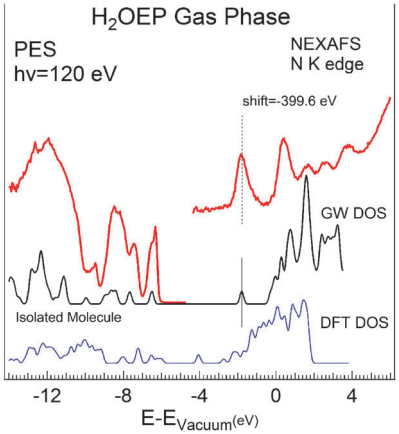

Fig. 3 Density of occupied and unoccupied electronic states for the H_2OEP molecule in gas phase. Upper curves in red: experimental results from PES (occupied states) and NEXAFS (unoccupied states). Middle curve in black: computed GW DOS. Lower blue curve: computed DFT DOS. All energies are referred to the vacuum level.

(in red) and angles (in black). Once the angles and bonds that involve hydrogen atoms are neglected, because their position is determined with less accuracy by XRD, we obtain a mean relative deviation from the experimental geometry[24] of 0.38% concerning bond lengths and of 0.30% concerning angles.

In the crystalline form, the macrocycle is slightly ruffled, and we find for the fully relaxed geometry a mean absolute displacement from the average plane of 0.026 Å, compatible with experimental results reported in ref. 24 where a value of 0.021 ± 0.02 Å is found.

The shortest intermolecular distance, 2.3 Å, is between a methylene hydrogen atom and a hydrogen atom bonded to a *meso* carbon belonging to molecules displaced by (011) (in primitive lattice units). In ref. 24 a shortest intermolecular distance of 2.4 Å is reported, confirming the agreement between the experimental and theoretical geometry.

3.2 Electronic structure

Isolated molecule. The DOS of the isolated molecule, computed at the DFT and GW level, is shown in Fig. 3 together with the measured PES and NEXAFS. The first peak of the N K edge NEXAFS is aligned to the computed GW LUMO level. The N K-edge NEXAFS spectrum for the transition N1s-LUMO shows two peaks, labeled L_1 and L_2, due to the initial state effects of the N 1s core level doublet excitation and related to the presence of two inequivalent N species in the macrocycle.[45]

The computed isolated molecule energy levels close to the gap are reported in Table 1. The ionization potential (IP) of the molecule in gas phase is predicted to be 5.9 eV, close to the measured value of 6.3 eV, and to the previously computed value of 5.7 eV.[23] The discrepancy between the two calculations might be explained taking into account that the calculation methods of ref. 23 involved (truncated) summations on empty states, while here explicit summations of such a kind are exactly avoided.

At the DFT level, when many-body effects are neglected, the IP (4.4 eV) is strongly underestimated and the HOMO–LUMO gap is much smaller than in the GW calculation: the gap is 2.0 eV within DFT, while it is 4.7 eV within GW (see Table 1). In the previous GW calculation,[23] a slightly smaller value of 4.4 eV was reported for the electronic gap, which is consistent with the difference found in the IP values.

Table 1 Computed HOMO − 1, HOMO, LUMO, LUMO + 1 energy levels for the isolated H_2OEP molecule. Energies are referred to the vacuum level E_{Vacuum}

Gas phase	HOMO − 1 (eV)	HOMO (eV)	LUMO (eV)	LUMO + 1 (eV)	GAP (eV)
DFT	−4.6	−4.4	−2.4	−2.4	2.0
GW	−5.9	−5.9	−1.2	−1.2	4.7
HF ($\Sigma_c = 0$)	−5.5	−5.8	0.9	1.0	6.7

As the occupied part of the DOS was extensively analyzed in ref. 23, here we focus on the unoccupied levels, which in the gas phase are experimentally probed by NEXAFS.

Once the GW DOS and the NEXAFS signal are aligned by setting the same energy for the LUMO, the two curves present structures and peaks at similar positions (see Fig. 3). However, the agreement concerning the relative intensities of the peaks is not satisfactory: the GW DOS shows a steep rise above the vacuum level due to the presence of free electron states which instead do not contribute to the NEXAFS. As the character of the free electron states is completely different from the one that we expect to give rise to the NEXAFS, we look at how many body effects are acting on the different states. In Fig. 4 we show the GW corrections and the expectation value of the exchange term $\langle \Sigma_x \rangle$ as a function of KS energies. It can be seen that most of the GW corrections for the unoccupied states range between 0 and 1 eV; however there are a bunch of states with larger corrections. When we look at the values of $\langle \Sigma_x \rangle$ the different character of these states becomes even more evident.

Since the magnitude of $\langle \Sigma_x \rangle$ is linked to the degree of localization over the occupied states of the single-particle-state wavefunctions, it may provide a preliminary criterion to select the single particle states that contribute mostly to the experimental peaks present in the NEXAFS spectra, where the probed empty states must have a finite oscillator strength with the core-hole.

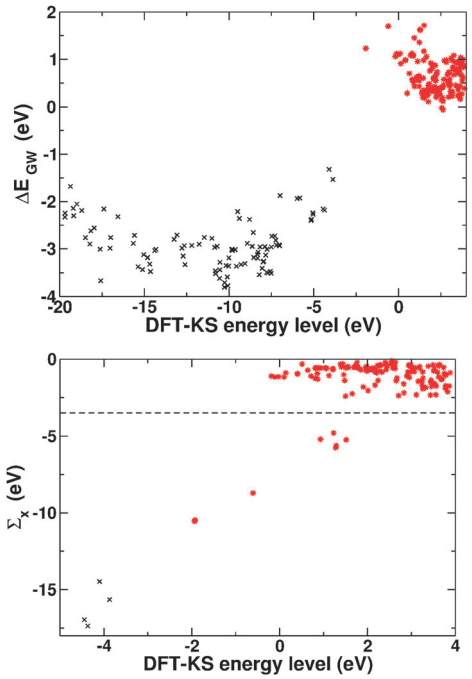

Fig. 4 Top panel: GW corrections as a function of KS energy for the isolated H_2OEP molecule. Bottom panel: Σ_x as a function of KS energies. Black crosses refer to occupied energy levels, while red stars to unoccupied ones.

The set of empty states with $|\langle\Sigma_x\rangle| < 3.5$ eV is clearly isolated from the rest. By taking into account only the empty states that fulfill this condition (*i.e.* that lie below the dashed line in the bottom panel of Fig. 1), we obtain the DOS plotted in red in Fig. 5: the experimental peaks structure is still nicely reproduced with only 9 of the 145 empty states used in the full calculation, and the agreement concerning their relative intensity is improved. It is interesting to notice that similar results are obtained by projecting the total DOS onto the atomic orbitals of the macrocycle carbon and nitrogen atoms (blue-dashed line in Fig. 5).

Thin film phase. Concerning the effect of crystal packing on the electronic properties of molecules, a decrease of the band gap was

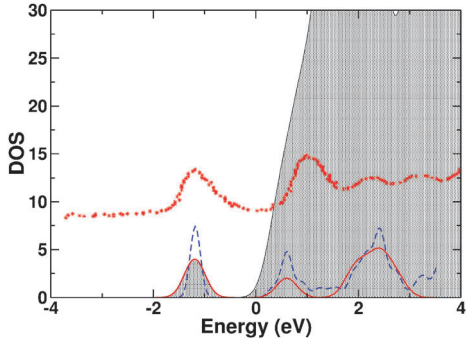

Fig. 5 Comparison of computed GW DOS for the isolated molecule, and gas-phase NEXAFS. Black shaded area: full GW-DOS of the H_2OEP isolated molecule from Fig. 3; red line: GW DOS obtained taking into account only the states for which $|\langle\Sigma_x\rangle| > 3.5$ eV; blue-dashed line: projected DOS onto the macrocycle carbon and nitrogen atoms; red stars: experimental NEXAFS results.

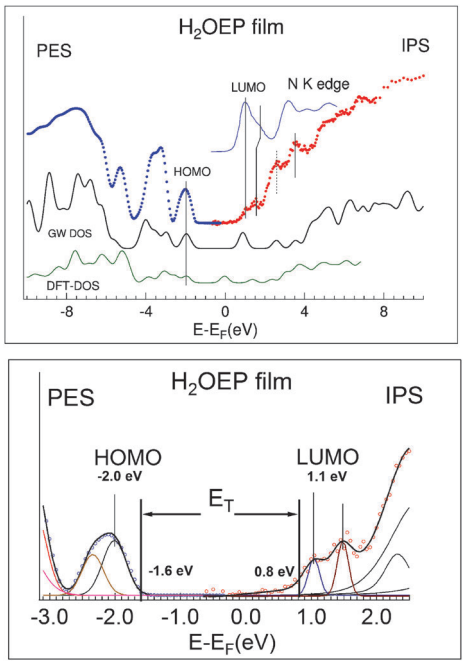

Fig. 6 Top: combined PES and IPS data (blue and red dots respectively) of the H_2OEP film together with the computed DOS (GW results: green line; DFT results: orange line) and NEXAFS (thin full blue line). Bottom: frontier orbital region of the combined PES and IPS spectra (open circles) of the H_2OEP film. The lines are their fits and the relevant components. E_T indicates the transport gap.

reported in corannulene-based materials,[36] in crystalline rubrene,[37] benzene, pentacene, C_{60}, and PTCDA.[38–40] Such changes in the electronic properties of the film with respect to the molecular phase might be caused by a geometry distortion within each molecule and/or an enhancement of the electronic screening. Interestingly, DFT in the standard KS approach was not able to capture this effect and it was compulsory to go beyond this level of description either by using hybrid functionals[38] or by employing MBPT.[39,40]

Fig. 6 shows the combined experimental PES-IPS data of the H_2OEP thin film, the film phase N K edge NEXAFS, and the GW and DFT DOS computed for the triclinic structure. For clarity, the NEXAFS are plotted by aligning the LUMO peak to the first structure of the IPS, and the theoretical DOS are plotted by aligning the HOMO level with the experimental one.

The film transport gap E_T value of 2.4 ± 0.2 eV has been determined by the energy difference between the VB and CB onsets,[8] as found by the least mean square fitting procedure of the experimental spectra. The lower panel of the figure shows the frontier orbital region of the combined PES and IPS measurements of the H_2OEP film. The dots correspond to the PES-IPS spectra. The lines are their fits and the relevant components. The vertical lines correspond to the VB (−1.6 eV) and CB (0.8 eV) onsets. The HOMO and LUMO peaks result at −2.0 eV and at 1.1 eV respectively. The HOMO–HOMO − 1 splitting is 0.35 eV, while LUMO and LUMO + 1 splitting is 0.45 eV in IPS and 0.6 eV in N K edge NEXAFS (top panel).

In Table 2 we report, for the triclinic phase, the computed energy levels of the HOMO − 1, HOMO, LUMO, and LUMO + 1

Table 2 Computed HOMO − 1, HOMO, LUMO, LUMO + 1 energy levels for the H_2OEP molecule in the triclinic phase. Absolute values of energies are obtained by aligning the HOMO with the experimental value

Triclinic phase	HOMO − 1 (eV)	HOMO (eV)	LUMO (eV)	LUMO + 1 (eV)	GAP (eV)
DFT	−1.7	−1.6	0.2	0.3	1.8
GW	−1.7	−1.6	1.0	1.2	2.6
HF ($\Sigma_c = 0$)	−2.3	−1.6	4.8	4.9	6.4

states together with the values of the fundamental gap. Within the GW approach the value of the film electronic gap is 2.6 eV, in excellent agreement with the experimental finding of 2.4 ± 0.2 eV, especially when compared to the DFT value of 1.8 eV.

As in the case of other molecular crystals,[36–40] the computed electronic gap of the film is significantly smaller than the isolated molecule gap (2.6 eV *vs.* 4.7 eV). This effect is only found at the GW level: at the DFT level the gap is 1.8 eV, slightly smaller than the gap of the molecule in gas phase (2.0 eV).

In order to disentangle the effects of the geometry distortion from those of the increased electronic screening due to crystal packing, we performed a GW calculation for an isolated molecule whose geometry was kept fixed to the distorted one. The results are listed in Table 3: there is no shrinking of the electronic gap due to the geometry distortion; in contrast, the GW electronic gap of the distorted molecule is slightly larger than that in the equilibrium geometry (4.8 eV *vs.* 4.7 eV).

The results of calculations where Σ_c was set equal to 0 are also shown in Tables 1–3. These calculations are equivalent to a non-self-consistent Hartree–Fock calculation scheme where the wavefunctions are kept fixed to their KS values. Within this scheme, similar to the case of DFT-KS results, the triclinic phase, the isolated molecule, and the isolated molecule in the distorted configuration have almost the same band gap. Since in this kind of calculations the electronic screening is not present, this further suggests that screening effects are at the origin of the difference of the electronic gap of the two phases.

PES data show that in the film the HOMO–HOMO − 1 orbitals energy separation is increased with respect to the gas phase. As well, IPS show that the LUMO and LUMO + 1 levels, degenerate in the gas phase, are split, and indeed the broadening of the LUMO present in the N K edge NEXAFS could be related to such a splitting.

The origin of the LUMO and LUMO + 1 degeneracy in the gas phase can be understood by looking at the electronic density isosurfaces of the two states, shown in the right part of Fig. 7. The LUMO and LUMO + 1 degeneracy is linked to the 'square' symmetry of the macrocycle (indeed the macrocycle has a lower D_{2h} symmetry due to the presence of two H atoms). Taking into account the stacking of the molecules within the crystal (left panel of Fig. 7), it can be seen that the system becomes even less symmetric and the LUMO and LUMO + 1 states are found to be split by ∼0.4 eV. In the

Table 3 Electronic gap at the DFT, GW and HF level of the isolated molecule with a distorted geometry

	DFT	GW	HF ($\Sigma_c = 0$)
GAP (eV)	2.0	4.8	6.3

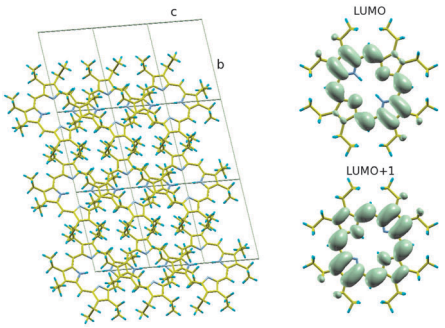

Fig. 7 Left: stacking of the H_2OEP molecules within the triclinic structure. View from the (100) direction. Right: LUMO and LUMO + 1 electronic density isosurface of the isolated molecule at 2.5% of its maximum value.

calculations a splitting between these two levels is present as well, although it is of a smaller magnitude (0.2 eV). To further clarify this point we performed a calculation of the triclinic phase with an artificially distorted molecule. The molecule was distorted in the spirit of ref. 46, namely, one of the two diagonals of the N-atoms square was stretched by 0.1. All the atoms were rigidly shifted accordingly, so that finally only four C–C bonds within the macrocycle were stretched. The resulting structure was higher in energy with respect to the most stable one of $\sim 6 \times 10^{-3}$ eV per atom. As a consequence of the square symmetry breaking, a larger LUMO and LUMO + 1 splitting of ∼0.3 eV was found already at the DFT level.

In Fig. 8 the total GW DOS of the isolated molecule and that of the film are presented together with their projections onto

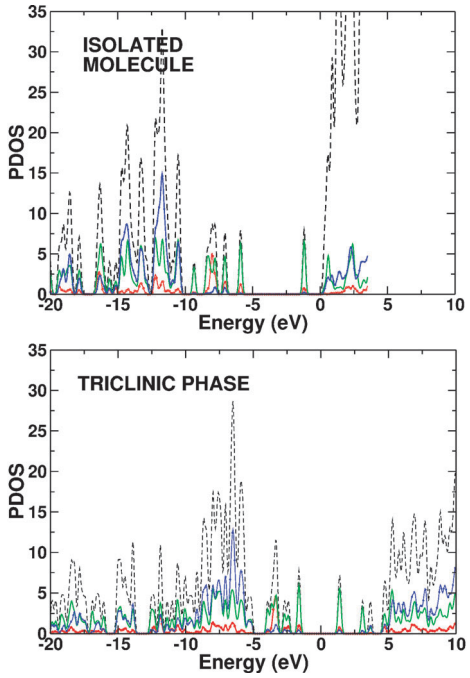

Fig. 8 Projected DOS for the isolated molecule (top panel) and the triclinic phase (bottom panel). Dashed black lines: total DOS; red lines and points: contribution from N atoms; green full lines: contribution from macrocycle C atoms; blue lines and points: contribution from ethyl-group C atoms. In the isolated molecule case all energies are referred to the vacuum level, and in the triclinic phase the HOMO is aligned to the experimental one.

the atomic orbitals of the nitrogen atoms, of the macrocycle carbon atoms, and of the ethyl-group carbon atoms. The comparison of the projected DOS (PDOS) of the film and those of the isolated molecule shows that crystal packing does not alter qualitatively the distribution in energy of the electronic states belonging to the different parts of the molecule. At low energies, between −20 and −10 eV, the states have a mixed macrocycle and ethyl-group character, and the latter becomes predominant between −10 and −5 eV, although the contribution from macrocycle atoms is not at all negligible also in this range of energies. Close to the gap, the electronic states belong, almost completely, to the macrocycle atoms. The total DOS of the isolated molecule rises promptly above the vacuum level, and this rise is not present in the triclinic phase calculation and is addressable to the presence of free electron states whose density, moreover, depends on the size of the simulation cell. Apart from the magnitude of the HOMO–LUMO gap, and not taking into account the total DOS, the PDOS of the unoccupied states is again qualitatively similar to that of the film: the LUMO is addressable mainly to the macrocycle atoms and the ethyl group contribution begins at higher energies.

4 Conclusions

In conclusion we carried out a combined experimental and theoretical investigation concerning the effects of crystal packing on the electronic properties of the H_2OEP molecule, focusing our attention on the unoccupied density of states and on the fundamental transport band gap. The unoccupied states of the film have been probed experimentally using IPS. This technique yields direct information on the unoccupied energy levels in contrast to optical measurements where the joint-density of states is probed and many-body effects make the interpretation of spectra in terms of single particle transitions hardly possible.[41]

At the theoretical level a quantitative description of the electronic properties of materials requires the inclusion of many-body effects going beyond DFT. We computed, for this purpose, GW corrections to the DFT KS energy levels reaching a remarkable agreement with experiment.

In particular we found that, upon packing to form a molecular crystal, the H_2OEP molecule undergoes a sizable shrinking of the HOMO–LUMO gap. This effect is not due to the deformation of the geometry of the molecule, but due to a more effective electronic screening in the 3D system. The computed electronic gap value of 2.6 eV is in excellent agreement with the experimental one of 2.4 eV. Square symmetry breaking, due to crystal packing and possible distortions of the molecule, induces a splitting of the LUMO and LUMO + 1 levels of $\sim$0.4 eV. This effect is present also in the calculations although it is slightly underestimated.

Acknowledgements

This work is partially supported by the Italian Ministero dell' Istruzione, dell' Universitá e della Ricerca through the FIRB "Nanosolar" (contract No. RBAP11C58Y_003), the FIRB "SUPRACAR-BON" (contract No. RBFR10DAK6) and by the PRIN "GRAF" (contract No. 20105ZZTSE). The staff of Gas Phase Beamline (ELETTRA) is kindly acknowledged. The calculations have been performed at the CINECA HPC facility through the project ISC09, and at the ENEA CRESCO facility.

References

1 O. Loboda, *Quantum-Chemical Studies on Porphyrins, Fullerenes and carbon Nanostructures, Carbon Nanostructures*, Springer-Verlag, Berlin Heidelberg, 2013, vol. XVIII.
2 M. G. Walter, A. B. Rudine and C. Wamser, *J. Porphyrins Phthalocyanines*, 2010, **14**, 759.
3 M. Hambourger, *et al.*, *Chem. Soc. Rev.*, 2009, **38**, 25.
4 S. Mathew, *et al.*, *Nat. Chem.*, 2014, **6**, 242.
5 S. D. Pop, S. P. Kate. J. Rappich and K. Hinrichs, *Sol. Energy Mater. Sol. Cells*, 2014, **127**, 169.
6 M. Vasilopoulou, *et al.*, *J. Mater. Chem. A*, 2014, **2**, 182.
7 J. Cai, *et al.*, *Soft Mater.*, 2014, **10**, 2612.
8 D. R. T. Zahn, G. N. Gavrila and M. Gorgoi, *Chem. Phys.*, 2006, **325**, 99.
9 D. R. T. Zahn, G. N. Gavrila and G. Salvan, *Chem. Rev.*, 2007, **107**, 1161–1232.
10 J. Xiao and P. A. Dowben, *J. Phys.: Condens. Matter*, 2009, **21**, 052001.
11 H. Yoshida, K. Tsutsumi and N. Sato, *J. Electron Spectrosc. Relat. Phenom.*, 2001, **121**, 83.
12 T. Schwieger, M. Knupfer, W. Gao and A. Kahn, *Appl. Phys. Lett.*, 2003, **83**, 500.
13 S. Krause, M. B. Casu, A. Schll and E. Umbach, *New J. Phys.*, 2008, **10**, 085001.
14 J. Wsten, S. Berger, K. Heimer, S. Lach and Ch. Ziegler, *J. Appl. Phys.*, 2005, **98**, 013705.
15 C. I. Wu, Y. Hirose, H. Sirringhaus and A. Kahn, *Chem. Phys. Lett.*, 1997, 272.
16 J. H. Weaver, *J. Phys. Chem. Solids*, 1992, **53**, 1433.
17 M. Schatzmayr, G. Koller, I. Kardinal, M. G. Ramsey, S. Stafström and F. P. Netzer, *J. Chem. Phys.*, 1999, **110**, 8060.
18 G. Rojas, X. Chen, C. Bravo, J.-H. Kim, J.-S. Kim, J. Xiao, P. A. Dowben, Y. Gao, X. Cheng Zeng, W. Choe and A. Enders, *J. Phys. Chem. C*, 2010, **114**, 9408.
19 S. Rangan, S. Coh, R. A. Bartynski, K. P. Chitre, E. Galoppini, C. Jaye and D. Fischer, *J. Phys. Chem. C*, 2012, **116**, 2392.
20 G. Rojas, S. Simpson, X. Chen, D. A. Kunkel, J. Nitz, J. Xiao, P. A. Dowben, E. Zurekb and A. Enders, *Phys. Chem. Chem. Phys.*, 2012, **14**, 4971.
21 S. Rangan, S. Katalinic, R. Thorpe, R. A. Bartynski, J. Rochford and E. Galoppini, *J. Phys. Chem. C*, 2010, **114**, 1139.
22 N. E. Gruhn, D. L. Lichtenberger, H. Ogura and F. A. Walker, *Inorg. Chem.*, 1999, **38**, 4023.
23 G. Stenuit, *et al.*, *Phys. Chem. Chem. Phys.*, 2010, **12**, 10812.
24 J. W. Lauher and J. A. Ibers, *J. Am. Chem. Soc.*, 1973, **95**, 5148.
25 S. Dugar, R. Fu and N. S. Dalal, *J. Phys. Chem. B*, 2012, **116**, 9215–9222.

26 P. Borghetti, *et al.*, *J. Chem. Phys.*, 2013, **138**, 144702.
27 R. M. Dreizler and E. K. U. Gross, *Density Functional Theory*, Springer-Verlag, Heidelberg, 1990; R. O. Jones and O. Gunnarsson, The density functional formalism, its applications and prospects, *Rev. Mod. Phys.*, 1989, **61**, 689.
28 G. Onida, L. Reining and A. Rubio, *Rev. Mod. Phys.*, 2002, **74**, 601.
29 M. M. Rieger, L. Steinbek, I. D. White, H. N. Rojas and R. W. Godby, *Comput. Phys. Commun.*, 1999, **117**, 211.
30 H. N. Rojas, R. W. Godby and R. J. Needs, *Phys. Rev. Lett.*, 1995, **74**, 1827.
31 A. Fleszar and W. Hanke, *Phys. Rev. B: Condens. Matter Mater. Phys.*, 1997, **56**, 10228.
32 S. Lebgue, B. Arnaud, M. Alouani and P. E. Bloehl, *Phys. Rev. B: Condens. Matter Mater. Phys.*, 2003, **67**, 155208.
33 P. Giannozzi, *et al.*, *J. Phys.: Condens. Matter*, 2002, **21**, 395502.
34 J. P. Perdew, K. Burke and M. Ernzerhof, *Phys. Rev. Lett.*, 1996, **77**, 3865.
35 P. Umari, G. Stenuit and S. Baroni, *Phys. Rev. B: Condens. Matter Mater. Phys.*, 2010, **81**, 115104.
36 L. Zoppi, L. Martin-Samos and K. K. Baldridge, *J. Am. Chem. Soc.*, 2011, **133**, 14002.
37 N. Sai, M. L. Tiago, J. R. Chelikowsky and F. A. Reboredo, *Phys. Rev. B: Condens. Matter Mater. Phys.*, 2008, **77**, 161306(R).
38 S. Rafaely-Abramson, S. Sharifzadeh, M. Jain, R. Baer, J. B. Neaton and L. Kronik, *Phys. Rev. B: Condens. Matter Mater. Phys.*, 2013, **88**, 081204(R).
39 J. B. Neaton, M. S. Hybertsen and S. G. Louie, *Phys. Rev. Lett.*, 2006, **97**, 216405.
40 S. Sharifzadeh, A. Biller, L. Kronik and J. B. Neaton, *Phys. Rev. B: Condens. Matter Mater. Phys.*, 2012, **85**, 125307.
41 A. Ruini, M. J. Caldas, G. Bussi and E. Molinari, *Phys. Rev. Lett.*, 2002, **88**, 206403.
42 G. P. Moss, *Pure Appl. Chem.*, 1987, **59**, 779.
43 C. A. Hunter and J. K. M. Sanders, *J. Am. Chem. Soc.*, 1990, **112**, 5525.
44 D. L. Cullen and E. F. Meyer Jr, *J. Am. Chem. Soc.*, 1974, **96**, 2095.
45 G. Di Santo, S. Blankenburg, C. Castellarin-Cudia, M. Fanetti, P. Borghetti, L. Sangaletti, L. Floreano, A. Verdini, E. Magnano, F. Bondino, C. A. Pignedoli, M.-T. Nguyen, R. Gaspari, D. Passerone and A. Goldoni, *Chem. – Eur. J.*, 2011, **17**, 14354.
46 C. O. Fernandez, M. Kogan, A. Valasinas and B. Frydman, *J. Org. Chem.*, 1998, **63**, 4829.

Electronic Supplementary Material (ESI) for Physical Chemistry Chemical Physics.

Solid state effects on the electronic structure of H_2OEP - Electronic Supplementary Information

M. Marsili,[*a,b] **P. Umari,**[a,c] **G. Di Santo,**[d] **M. Caputo,**[d] **M. Panighel,**[d,e] **A. Goldoni,**[d] **M. Kumar,**[f] **and M. Pedio** [f]

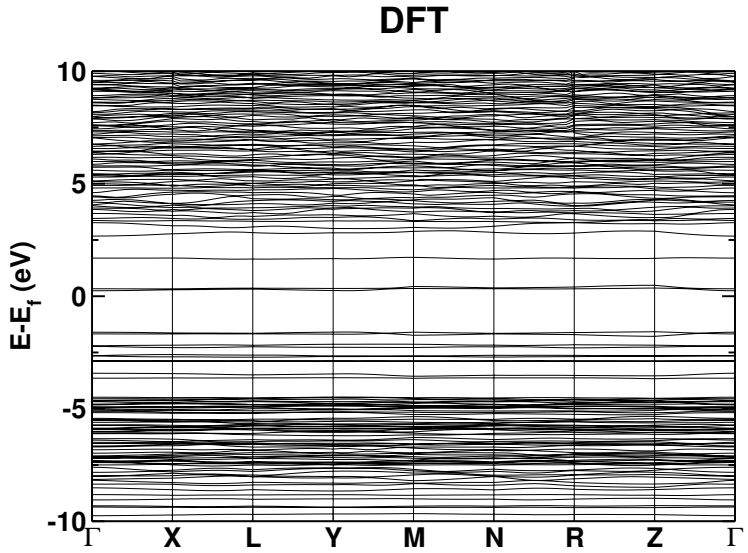

Figure 1 DFT band structure along high symmetry directions. Energies are referred to the experimental Fermi level, alligned as explained in the text.

[a] *Dipartimento di Fisica e Astronomia, Universitá di Padova, via Marzolo 8, Padova 35131, Italy. Fax: +39 049 8277102; Tel: +39 049 8277174; E-mail: margherita.marsili@nano.cnr.it*
[b] *S3, Istituto Nanoscienze-CNR, Via Campi 213/A, 41125 Modena, Italy*
[c] *IOM-CNR, Theory@Elettra group, Trieste, Italy*
[d] *Elettra - Sincrotrone Trieste, s.s. 14 km 163.5 in Area Science Park, Basovizza (Trieste) 34149, Italy*
[e] *Department of Physics, University of Trieste, via Valerio 2, Trieste 34100, Italy*
[f] *IOM-CNR, TASC Area Science Park Buil. MM, S.S. 14, Km 163.5, Basovizza (Trieste) 34149, Italy*

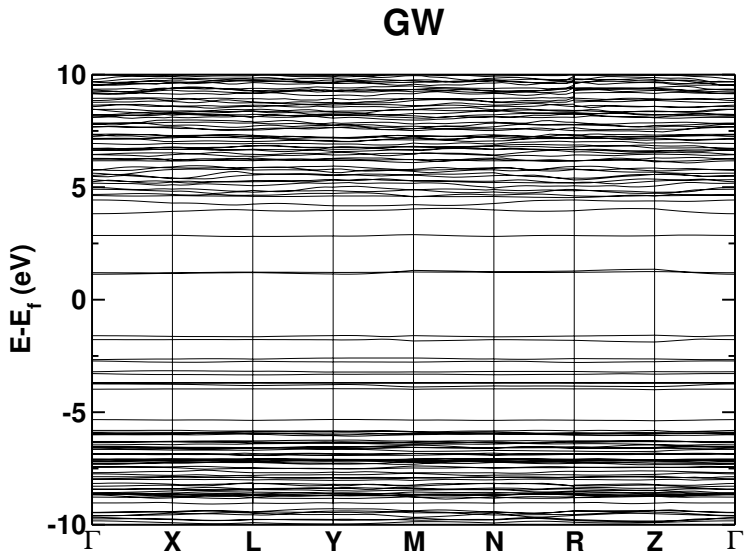

Figure 2 GW band structure along high symmetry directions. Energies are referred to the experimental Fermi level, alligned as explained in the text.

3

Metallic Picene/C_{60} heterojunctions and the effect of potassium doping

The choice of electron donor and acceptor molecules is a key aspect in the design of OPV cells, in particular their energetic levels have to be aligned such that the exciton formed by impinging photons can be separated at the interface between the two. Many molecules has been explored as electron donor (phthalocyanines [3, 25–27], porphyrines [28, 29], and others [30–32]), but as electron acceptor C_{60} and its derivatives has always showed excellent performance.

We explored the possibility to use Picene as electron donor in a Picene/C_{60} heterojunction. However, growing layer by layer this heterojunction resulted in a metallic film. Of course a metallic film is not usable for excitons separations, however this systems shows frontier orbital similar to a monolayer of C_{60} adsorbed on coinage metals [33–35], with a charge transfer from the Picene molecules to the C_{60}. This inspired us to dope the sample, and the result is a continuous tuning of the C_{60} charge state, something not possible for a C_{60} multilayer due to phase separation effect [36].

PHYSICAL REVIEW B **90**, 201401(R) (2014)

Metallic picene/C_{60} heterojunctions and the effect of potassium doping

Marco Caputo, Mirco Panighel, Luca Petaccia, Claudia Struzzi, and Vajiheh Alijani
Elettra Sincrotrone Trieste, s.s. 14 km 163.5 in Area Science Park, 34149 Trieste, Italy

Marcello Coreno
CNR-IMIP, Montelibretti, Roma, Italy

Monica de Simone
TASC CNR-IOM Laboratory, s.s. 14 km 163.5 in Area Science Park, 34169 Trieste, Italy

Guido Fratesi
ETSF, CNISM, and Dipartimento di Scienza dei Materiali, Università Milano-Bicocca, via Cozzi 55, 20125 Milano, Italy and Dipartimento di Fisica, Università di Milano, via Celoria 16, 20133 Milano, Italy

Giovanni Di Santo and Andrea Goldoni*
Elettra Sincrotrone Trieste, s.s. 14 km 163.5 in Area Science Park, 34149 Trieste, Italy and INSTM–Elettra, Micro & Nano-Carbon Laboratory, s.s. 14 km 163.5 in Area Science Park, 34169 Trieste, Italy

(Received 21 March 2014; revised manuscript received 8 September 2014; published 3 November 2014)

A metallic system without any further doping was obtained combining, in a bulk film, heterojunctions made by subsequent depositions of C_{60} and picene layers on Ag(111). This is caused by the formed dipole between the two molecules due to the huge difference in electron affinities and the charge transfer from the substrate. The above situation and the expected molecular geometry have also a role when the heterojunction film is doped with potassium. C_{60} phases diverse from those observed in bulk C_{60}, especially, a metallic state with continuous alkali doping of the LUMO bands was found. This opens the way towards novel bulk molecular heterojunction structures that may create new electronic phases in strongly correlated molecular materials. The present case appears as the only manner known so far to form a bulk metallic K_xC_{60} system ($0 < x < 6$) that may evoke the possibility of seeing the awaited dome-shaped region of the doping-temperature phase diagram if the system should show superconductivity.

DOI: 10.1103/PhysRevB.90.201401 PACS number(s): 74.70.Kn, 73.20.−r, 79.60.Dp, 79.60.Jv

Many properties of organic superconductors are strongly dependent on the number of charge carriers (doping) put into the lowest unoccupied molecular orbitals (LUMO) bands. The doping is usually chemical and it can be obtained by intercalating alkali metals into the structure of the molecular crystals. Some doped crystals may show a metallic behavior and, sometimes, superconductivity may appear at low temperatures.

The most famous molecular crystal with the highest superconducting critical temperature (T_c) is A_3C_{60} (A = alkali metal). In these crystals, characterized by three-dimensional arrangements of almost spherical C_{60} anions, the superconductivity is determined by the competition between localized electronic ground states in fullerenes [1–5]. The absolute T_c observed depends mainly on the electronic structure details related to the molecular orbitals overlap within packing of C_{60}. T_c typically rises with increasing molecular space [1–7] and it is widely accepted that superconductivity, as observed in high-T_c cuprate superconductors, occurs in connection to the correlation-driven Mott metal-insulator transition over a dome-shaped region of the doping-temperature phase diagram, where the highest T_c is obtained for the so-called "optimum doping" [5].

Differently from the high-T_c superconducting copper oxides families where a continuous doping can be made by cationic substitution, in C_{60} solid, the electron correlations and the crystal structure permit that only some particular doping phases are possible (phase separation) [8]. Therefore it is hard to follow by doping the dome-shaped region of the doping-temperature phase diagram near the "optimum doping," which seems to be around 3 electrons/molecule [6].

Here, we demonstrate that growing a heterojunction thin film made by a subsequent depositions of one layer of C_{60} and one layer of picene, up to a thickness of about 6–7 heterojunction layers on Ag(111), a metallic system is obtained. Moreover, doping the bulk heterojunctions with potassium (K) further metallic states are observed, with density of states (DOS) close to the Fermi level very similar to K_xC_{60} ($0 < x < 6$) on coinage metals (Au, Ag, and Cu).

Picene and C_{60} solids doped with potassium are both superconductors with similar T_c (about 18 K) and apparently the same LUMO filling [9]. While for K_3C_{60}, the crystal and electronic structures are well known [2], the situation of superconductivity in K_3 picene is quite controversial [9–13]. The two undoped molecular solids show some similarities [1,2,13–15], like comparable correlation energy (Hubbard $U \sim 1$ eV) and small LUMO band dispersion (0.5 eV). Conversely, they have different work functions (about 5.1 ± 0.1 eV in C_{60} and 4.6 ± 0.1 eV in picene, see Ref. [16]) and the orbital degeneracy in C_{60}, that causes Jahn-Teller

*Corresponding author: andrea.goldoni@elettra.eu

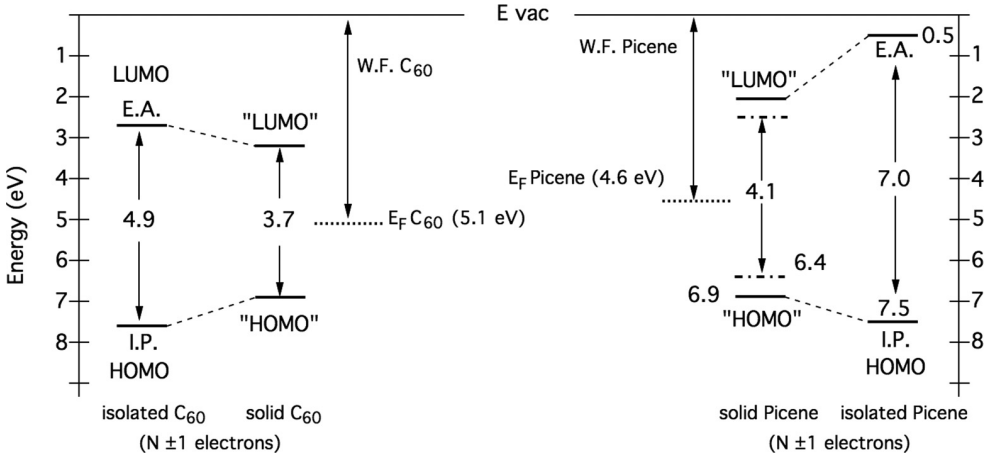

FIG. 1. Energy level diagram for C_{60} (left) and picene (right). The data for C_{60} were taken from reference [16], while for picene, we consider the data available in the literature [17] and our measurements. The dashes/dotted line above the "HOMO" for picene is the threshold position for the HOMO band and 4.1 eV is the adiabatic gap as obtained in Ref. [17b,c], see also Ref. [16].

distortion of the molecules in doped compounds [2], is absent in picene. Considering the isolated molecules, they have almost the same ionization potential (I.P.) that is 7.6 eV for C_{60} [17] and 7.5 eV as we measured for picene (supporting materials), but the electron affinity (E.A.) is quite different, i.e., 2.7 eV for C_{60} [17] and 0.5 eV for picene [18a,b].

Figure 1 shows an energy level diagram for the isolated C_{60} and picene molecules and for the respective molecular solids with respect to the vacuum level, according to our measurements and to the data present in the literature. One can expect that the interfacial electronic interactions in heterojunctions aggregates of C_{60} and picene can induce a ground state distortion of the molecular charges. The distortion and polarization of the electronic cloud in the picene/C_{60} heterojunction has the positive pole next to picene and the negative pole next to C_{60}.

Figure 2 shows the valence band photoemission spectra of interfaces formed by depositing alternating layers of C_{60} and picene molecules, starting from less than a monolayer of C_{60} on Ag(111) (bottom spectrum, 0.5 ML). This spectrum is characterized mainly by the presence of Ag 4*d* states with binding energy between 4 and 7 eV, a Fermi edge and the C_{60} highest occupied molecular orbital (HOMO) and HOMO-1 states on the flat Ag $s-p$ region at 1.8 and 3.3 eV, respectively.

The HOMO and HOMO-1 states appear at lower binding energy with respect to the C_{60} multilayer due to the metallic screening of the substrate [19]. Some interesting features emerge as the heterojunction system is grown.

First, forming the multilayer heterojunctions new molecular-derived states develop and evolve, but the screened HOMO and HOMO-1 states of C_{60} are always visible at the same binding energy, as it can be seen in particular for the screened HOMO feature after the formation of the last heterojunction, just before covering the surface by 4 ML of picene.

Second, the Fermi level (E_F) is always visible, with almost the same intensity, even if the Ag 4*d* bands are no longer discernible. Eventually, after covering the heterojuctions with 4 ML of picene, the Fermi jump E_F is still present although attenuated. Since the intensity at E_F remains almost constant when the heterojunctions are formed, the inset of Fig. 2(b) shows that the ratio $E_F/Ag\ 3d_{5/2}$ (Ref. [16]) increases as the Ag 3*d* decreases, apart from the last step when the intensity simply attenuates at E_F due to the superposition of 4ML of picene. The last spectrum of Fig. 2, apart from the small intensity jump at E_F due to the layers underneath, can be considered as the valence band of picene multilayer. Noteworthy, all spectra were collected at normal emission with the light horizontal linear polarization at 40° from the surface normal. By looking at the spectral features, we observe that the π peaks are strongly attenuated and the σ part enhanced and well separated in structures. This is a clear indication that the picene multilayer grows with the main molecular axis almost perpendicular to the substrate surface, at variance with the case of picene directly grown on Ag and Au substrates [9,10]. As a confirmation, density functional theory (DFT) simulations of the occupied DOS of isolated picene molecules are shown on top of this spectrum. We weighted π and σ contributions with factors of 0.12 and 0.88, respectively, which correspond to molecules having the main axis at a small angle (~20°) from the Ag(111) normal. The agreement between the spectrum and the simulation is good, in spite of the fact that the DFT can only approximately describe the true excited spectrum.

Third, as new heterojunction layers are formed starting from the monolayer of C_{60}/Ag(111), the features appearing in the valence band spectra mainly resemble the typical molecular orbitals of picene or C_{60}, depending on the termination layer. Some of them shift nonrigidly with respect to the corresponding multilayer spectra (e.g., picene states above 7 eV) caused by both the chemical potential movement and the molecular orbital hybridizations. Other states, like the frontier orbitals HOMO and HOMO-1 near the Fermi level, remain almost fixed.

The presence of a Fermi edge when the heterojunctions are formed, even in multilayer structures, may result from the appearance of an interfacial dipole between picene and C_{60}, introducing a change in the electronic environment, and is similar to concepts that were put forward for other organic heterojunctions [20–22]. Doped metallic molecular layers, decoupled from the metal surface by one or two sheets

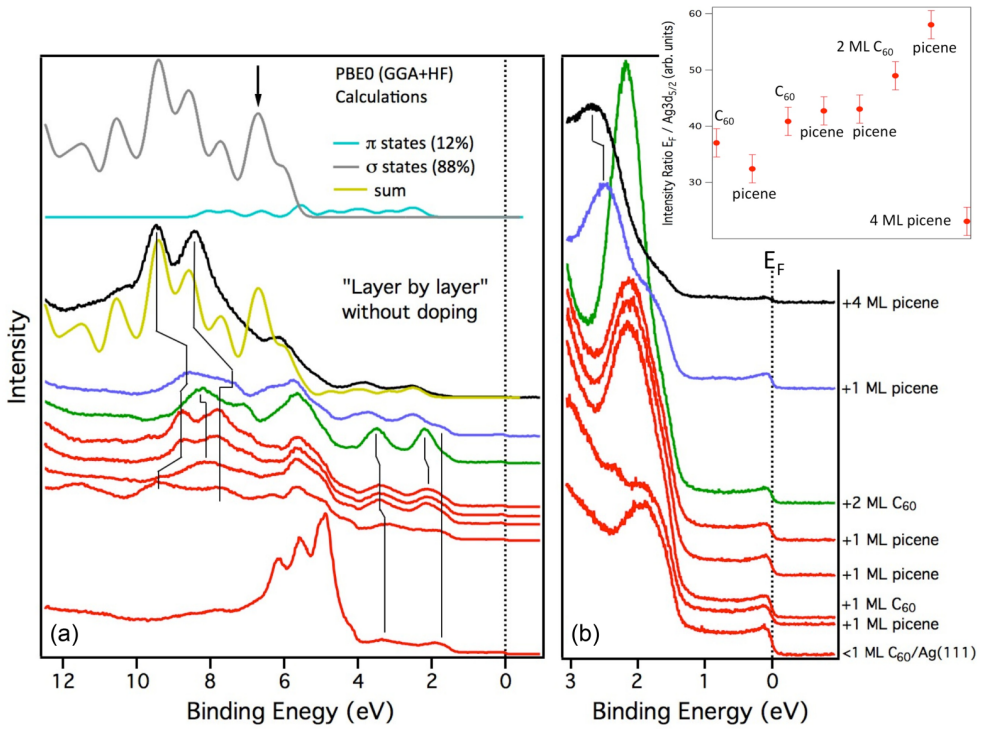

FIG. 2. (Color online) Valence-band spectra of picene/C_{60} heterojunctions as a function of the deposition layer of C_{60} or picene. (a) Extended binding energy region. On top are shown the calculated σ and π DOS of isolated picene molecules with opportune intensity of 88% and 12%, respectively. Their sum is plotted (yellow line) underneath the topmost spectrum (black, 4 ML of picene deposited atop the last heterojunction layer). The small differences in the σ states region (arrow) may be related to symmetry reasons (e.g., the initial state would be odd in our experimental geometry). (b) Binding energy region of the frontier orbitals. Note the presence of the screened HOMO orbital and DOS at E_F for each layer of heterojunctions. All the subsequently formed heterojunction layers, starting from the monolayer of C_{60}/Ag(111), are indicated on the right. (Inset) Intensity ratio $E_F/\mathrm{Ag}\,3d_{5/2}$, without considering the different escape depths.

of organic molecules, can be assembled without the use of dopants just by forming the proper heterojunctions. Niederhausen *et al.* [20] investigated C_{60} (sub)-monolayer films, which are prevented from direct electronic coupling with the Ag(111) substrate by a two-layer thick α-sexithiophene (6T) spacer. The authors unambiguously show that an integer charge transfer from the metal to a fraction of the C_{60} layer is caused by the interface dipole, while the 6T bilayer remains neutral. Stadtmüller and co-workers [21] showed a gradual filling of the LUMO of 1 ML 3,4,9,10-perylene-tetracarboxylic-dianhydride/Ag(111), which was already partly filled by the Ag substrate, due to a chemisorptive bonding of a further single monolayers of copper(II) phthalocyanine. Finally, a charge transfer from the metal to the hexaaza-triphenylene-hexacarbonitrile layer was observed when it was deposited atop of a monolayer of tris(8-hydroxyquinolinato)aluminum on Ag(111) [22]. Our data indicate a similar trend, but in a multilayer structure of heterojunctions, which offers further flexibility, as also observed for a multilayer of multicomponent N-methyldiazabicyclooctane cation, triptycene, and C_{60} [23].

However, to discern whether E_F is related to the electronic configuration of this system or to the presence of islands, which leave uncovered areas of Ag, angle-resolved photoemission experiments at different photon energies could be performed in order to observe the presence or not of Ag direct transitions close to the Fermi level. Anyway, the doping of this system with alkali metals seems to be appealing. Due to the high-energy separation between C_{60} and picene LUMOs, doping the heterojunction with potassium the electrons should fill the C_{60} LUMO. Near E_F, therefore, we should expect to see the same behavior of bulk C_{60} doped with K. Figure 3 shows the K doping starting from the last spectrum of Fig. 2 (black). Surprisingly, as electrons are donated, the intensity at the E_F evolves continuously akin a doped monolayer of C_{60} on coinage metals [19,24,25]. The number of electrons *per* C_{60} molecule, mediated on the few layers investigated with photoemission, can be evaluated from the intensity of the filled LUMO in comparison with the doped monolayer of C_{60} on Ag(100) [25]. The result, corresponding to a range of about 1 to 5 electrons *per* C_{60} molecule, is shown in Fig. 3(b).

That these heterojunctions behave like one monolayer of C_{60} adsorbed on coinage metals was also confirmed looking at the K2p and C1s core levels plotted in Fig. 4. The spectra of the undoped bulk systems, i.e., C_{60} multilayer (black line), picene multilayer (blue line) and picene/C_{60} heterojunctions (red dots), are shown at the bottom of Fig. 4. In particular, the latter is the sum of all the spectra taken while forming several layers of heterojunctions, since these spectra remain in the same position with a similar lineshape (Ref. [16]). This means that E_F was pinned during the formation of different heterojunction layers. Moreover, the C1s heterojunction peak is the sum of C_{60} and picene peaks just shifted in opposite

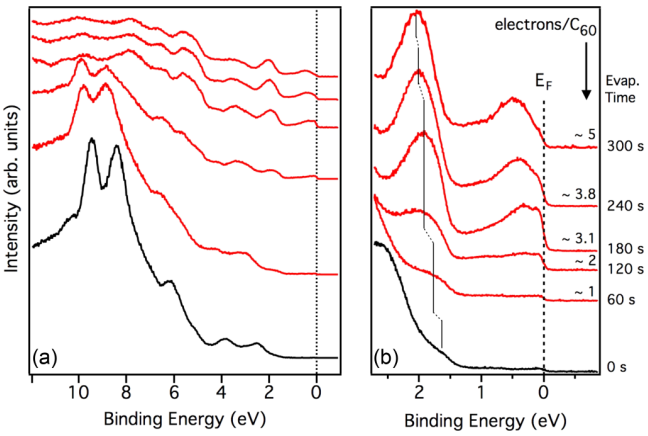

FIG. 3. (Color online) Valence-band photoemission spectra of the K-doped heterojunctions film starting from the black spectrum where about four monolayer of picene were deposited on top of the seven layers of heterojunction film. (a) Extended binding energy region. (b) Evolution of the frontier orbitals near E_F. The expected number of electrons is indicated (see text).

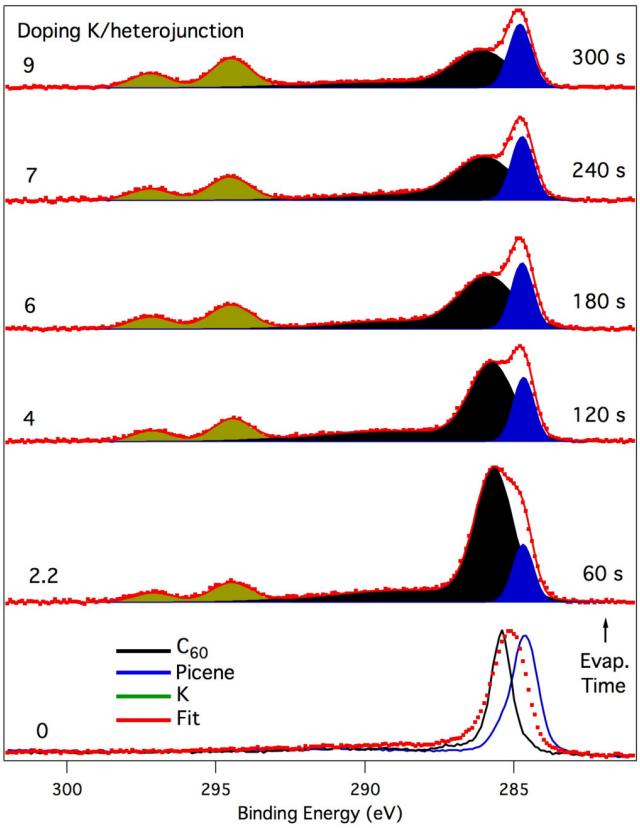

FIG. 4. (Color online) C1*s* core level photoemission spectra of undoped thick films (bottom spectra) of C_{60} (285.5 eV, black line), picene (284.5 eV, blue line), and of picene/C_{60} heterojunctions (285.0 eV, red points). On top there are the K-doped spectra (red point) with the fit analysis (red line). The green component is the K 2*p*, the asymmetric black component is the C1*s* of C_{60} + loss and the blue component is the C1*s* of picene. The numbers on the left correspond to the K atoms per heterojuction calculated with the ratio of K 2*p* and C 1*s* peak areas. The maximum error in these estimations was ±0.2. The K evaporation time is reported on the right.

directions by the same amount (0.7 ± 0.1 eV), due to the charge distortion of the formed dipole. On top of these spectra there are the subsequent K doped spectra (red dots) of the multilayer heterojunctions, with the corresponding fits (red line) and the resulting components (potassium K 2*p* = green, C_{60} C 1*s* = black, and picene C 1*s* = blue). These spectra were plotted as taken. The following features can be highlighted:

(1) The K $2p_{1/2}$ and $2p_{3/2}$ peaks are always formed by a single component, while on face centered cubic (fcc) bulk C_{60} compounds, in particular for K_3C_{60}, two components are observed related to octahedral and tetrahedral K atoms [8,26,27]. This immediately tells that the C_{60} molecules do not form an fcc structure.

(2) Measuring the area of K and C 1*s* peaks (normalized by their respective photoemission cross sections), the obtained rate of K atoms *per* heterojunction (C_{60} + picene) is about two times the electrons per C_{60} estimated in Fig. 3. Therefore each K atom transfers about 0.5–0.6 electrons to C_{60} and the remaining electrons on the K atoms form a sort of electrostatic screening continuum around the heterojunctions, which should reduce the intermolecular interactions and, in turn, the magnitude of the interfacial dipole between C_{60} and picene. The evolution of the C 1*s* core level seems to confirm this hypothesis, since adding K atoms the two C 1*s* components start to separate, with the picene always in the same position and the C_{60} shifting with doping.

To summarize, accurately fabricated picene/C_{60} heterojunction films on Ag(111) substrate, may tune the molecular electronic structures in such a way that the electron correlation strength, a key factor in determining the material properties of C_{60}, can be attenuated. Although here we are not dealing with superconductivity, but only on the electronic structure changes as a function of doping, the superconductivity is a relevant question for this system. Therefore, forming a continuous metallic state in bulk K_xC_{60} may allow following the possible dome-shaped behavior of T_c as a function of doping. Moreover, it opens the way towards novel molecular heterojunctions that may create new electronic phases in strongly correlated materials [20–23].

Experimental. The experiments were performed at room temperature in ultrahigh vacuum (10^{-10} mbar) using the experimental chambers of the BaDElPh beamline [28] and of the Micro&Nano-carbon Laboratory (modified VG-Escalab) at the Elettra synchrotron. The clean Ag(111) was prepared by sputtering and annealing cycles until no traces of contaminants were present in the XPS spectra (Mg K_α line) and a clear surface state was visible in the valence-band spectrum. The energy resolution of the XPS measurements was 0.8 eV. C_{60} and picene molecules were sublimated from degassed Ta crucibles at 300 °C and 130 °C, respectively, and deposited on Ag at room temperature. About 0.5 ML of C_{60} was obtained by growing a multilayer and then annealing the sample at 270 °C. The potassium was deposited with the sample at 50 °C using a SAES getter evaporator.

The solid valence band photoemission measurements were obtained using a photon energy of 31 eV with the linear horizontal polarization of the light at 40° from the sample surface normal. The photoelectrons were collected at normal emission integrating on a ±7° angular window by a SPECS Phoibos 150 mm hemispherical analyzer having a horizontal

entrance slit, i.e., in the scattering plane. In these conditions we are collecting spectra in the "even" geometry [29]. The total energy resolution (photons+analyzer) was 30 meV.

For the DFT numerical simulations, we have optimized the geometry with the PBE approximation to the exchange and correlation functional [30] and adopted for a final evaluation of the DOS the hybrid functional PBE0 [31], which was shown to yield a good agreement with many-body calculations and experiments for pentacene and perylene molecules apart from a rigid shift [32]. We used the plane-wave pseudopotential approach [33] with molecules placed in periodically repeated supercells, with a vacuum separation of 11 Å between adjacent replicas. The DOS shown in Fig. 2 was convoluted with a Gaussian peak having a full with at half maximum of 0.54 eV.

Acknowledgments. This work is partly financed by the Italian MIUR projects FIRB "Supracarbon" RBFR10DAK6 for G.D.S. and FIRB "Nanosolar" RBAP11C58Y for V.A. and A.G. and by the European Community through the ENIAC Joint Undertaking–ERG (Grant Agreement No. 270722-1-ERG) for M.C. C. S. is grateful to the grant of AREA Science Park of Trieste. We thank D. Lonza for technical supports. The critical reading of G. Scoles and E. Tosatti was appreciated.

[1] S. Chakravarty, M.P. Gelfand, and S. Kivelson, Science **254**, 970 (1991).

[2] O. Gunnarsson, *Alkali-Doped Fullerides: Narrow-Band Solids With Unusual Properties* (World Scientific, Singapore, 2004).

[3] Y. Iwasa and T. Takenobu, J. Phys.: Condens. Matter **15**, R495 (2003).

[4] P. Durand, G. R. Darling, Y. Dubitsky, A. Zaopo, and M. J. Rosseinsky, Nat. Mater. **2**, 605 (2003).

[5] M. Capone, M. Fabrizio, C. Castellani, and E. Tosatti, Phys. Rev. Lett. **93**, 047001 (2004); Rev. Modern Phys. **81**, 943 (2009).

[6] T. Yildirim, L. Barbedette, J. E. Fischer, C. L. Lin, J. Robert, P. Petit, and T. T. M. Palstra, Phys. Rev. Lett. **77**, 167 (1996).

[7] A. Y. Ganin, Y. Takabayashi, Y. Z. Khimyak, S. Margadonna, A. Tamai, M. J. Rosseinsky, and K. Prassides, Nat. Mater. **7**, 367 (2008).

[8] D.M. Poirier, Appl. Phys. Lett. **64**, 1356 (1994).

[9] R. Mitsuhashi, Y. Suzuki, Y. Yamanari, H. Mitamura, T. Kambe, N. Ikeda, H. Okamoto, A. Fujiwara, M. Yamaji, N. Kawasaki, Y. Maniwa, and Y. Kubozono, Nature (London) **464**, 76 (2010).

[10] B. Mahns, F. Roth, and M. Knupfer, J. Chem. Phys. **136**, 134503 (2012).

[11] M. Caputo, G. Di Santo, P. Parisse, L. Petaccia, L. Floreano, A. Verdini, M. Panighel, C. Struzzi, B. Taleatu, C. Lal, and A. Goldoni, J. Phys. Chem. C **116**, 19902 (2012).

[12] P. L. de Andres, A. Guijarro, and J. A. Verges, Phys. Rev. B **83**, 245113 (2011).

[13] G. Giovannetti and M. Capone, Phys. Rev. B **83**, 134508 (2011).

[14] M. Kim, B. I. Min, G. Lee, H. J. Kwon, Y. M. Rhee, and J. H. Shim, Phys. Rev. B **83**, 214510 (2011).

[15] A. Subedi and L. Boeri, Phys. Rev. B **84**, 020508(R) (2011).

[16] See Supplemental Material at http://link.aps.org/supplemental/10.1103/PhysRevB.90.201401 for the measured work functions of solid C_{60} and picene, the valence band of picene multilayer and gas phase picene, the C 1*s* core level photoemission spectra of all the heterojunctions layers formed, the shift in energy of the C 1*s* of C_{60} with potassium doping, the growing modes of C_{60} and picene on Ag(111) and the attenuation of Ag 3*d* core levels as a function of the heterojunction formation.

[17] D. L. Lichtenberger, K. W Nebesny, C. D. Ray, D. R. Huffman, and L. D. Lamb, Chem. Phys. Lett. **176**, 203 (1991); L. S. Wang, J. Conceicao, C. Jin, and R. E. Smalley, *ibid.* **182**, 5 (1991); T. R. Ohno, Y. Chen, S. E. Harvey, G. H. Kroll, J. H. Weaver, R. E. Haufler, and R. E. Smalley, Phys. Rev. B **44**, 13747 (1991).

[18] S. Lias, *Ionization energy evaluation*; J. E. Bartmess, *Negative Ion Energetics Data*, in NIST Chemistry WebBook, NIST Standard Reference Database No. 69, edited by P. J. Linstrom and W. G. Mallard (National Institute of Standards and Technology, Gaithersburg, MD); N. Sato, K. Seki, and H. Inokuchi, J. Chem. Soc., Faraday Trans. II **77**, 1621 (1981); N. Sato, H. Inokuchi, and E. A. Silinsh, Chem. Phys. **115**, 269 (1987); F. Roth, M. Gatti, P. Cudazzo, M. Grobosch, B. Mahns, B. Büchner, A. Rubio, and M. Knupfer, New J. Phys. **12**, 103036 (2010).

[19] B. W. Hoogenboom, R. Hesper, L. H. Tjeng, and G. A. Sawatzky, Phys. Rev. B **57**, 11939 (1998).

[20] J. Niederhausen, P. Amsalem, A. Wilke, R. Schlesinger, S. Winkler, A. Vollmer, J. P. Rabe, and N. Koch, Phys. Rev. B **86**, 081411(R) (2012).

[21] B. Stadtmüller, T. Sueyoshi, G. Kichin, I. Kröger, S. Soubatch, R. Temirov, F.S. Tautz, and C. Kumpf, Phys. Rev. Lett. **108**, 106103 (2012).

[22] P. Amsalem, J. Niederhausen, J. Frisch, A. Wilke, B. Bröker, A. Vollmer, R. Rieger, K. Müllen, J. P. Rabe, and N. Koch, J. Phys. Chem. C **115**, 17503 (2011).

[23] D. V. Konarev, S. S. Khasanov, A. Otsuka, M. Maesato, G. Saito, R. N. Lyubovskaya, Angew. Chem. Int. Ed. **49**, 4829 (2010).

[24] P. Rudolf, M. S. Golden, and P. A. Brühwiler, J. Electron Spect. Related Phenom. **100**, 409 (1999).

[25] C. Cepek, M. Sancrotti, T. Greber, and J. Osterwalder, Surf. Sci. **454–456**, 467 (2000).

[26] D. M. Poirier and J. H. Weaver, Phys. Rev. B **47**, 10959 (1993).

[27] A. Goldoni, L. Sangaletti, F. Parmigiani, S. L. Friedmann, Z.-X. Shen, M. Peloi, G. Comelli, and G. Paolucci, Phys. Rev. B **59**, 16071 (1999).

[28] L. Petaccia, P. Vilmercati, S. Gorovikov, M. Barnaba, A. Bianco, D. Cocco, C. Masciovecchio, and A. Goldoni, Nucl. Instrum. Methods .Phys. Res., Sec. A **606**, 780 (2010).

[29] M. C. Asensio, J. Avila, L. Roca, A. Tejeda, G. D. Gu, M. Lindroos, R. S. Markiewicz, and A. Bansil, Phys. Rev. B **67**, 014519 (2003).

[30] J. P. Perdew, K. Burke, and M. Ernzerhof, Phys. Rev. Lett. **77**, 3865 (1996).

[31] C. Adamo and V. Barone, J. Chem. Phys. **110**, 6158 (1999).

[32] S. Refaely-Abramson, S. Sharifzadeh, N. Govind, J. Autschbach, J. B. Neaton, R. Baer, and L. Kronik, Phys. Rev. Lett. **109**, 226405 (2012).

[33] P. Giannozzi *et al.*., J. Phys.: Condens. Matter **21**, 395502 (2009).

Supplemental Material

Further data

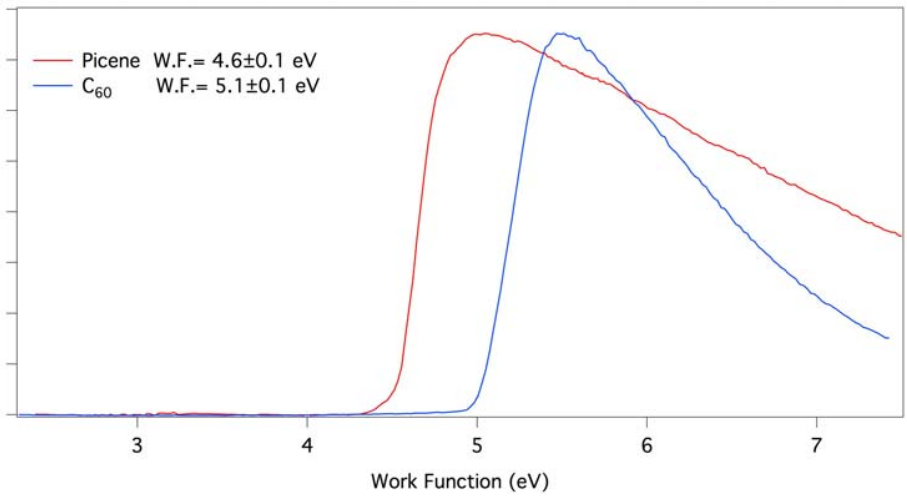

Figure SM1. Work functions of picene and C_{60} thick films on Ag(111). The spectra were measured using He I radiation ($h\nu$=21.22 eV) by applying a voltage of 6 eV to the sample with a pass-energy of 2 eV for the electron energy analyzer. The work functions (W.F.) are defined by the energy cutoff of the secondary electrons referred to the Fermi level. Therefore, they give the position of the Fermi levels (or in this case of the chemical potentials) for the two molecular solids with respect to the vacuum level (dotted levels in Fig. 1). The work function is defined as the middle of the energy cutoff of the secondary electrons, with an error bar that considers the total cutoff range.

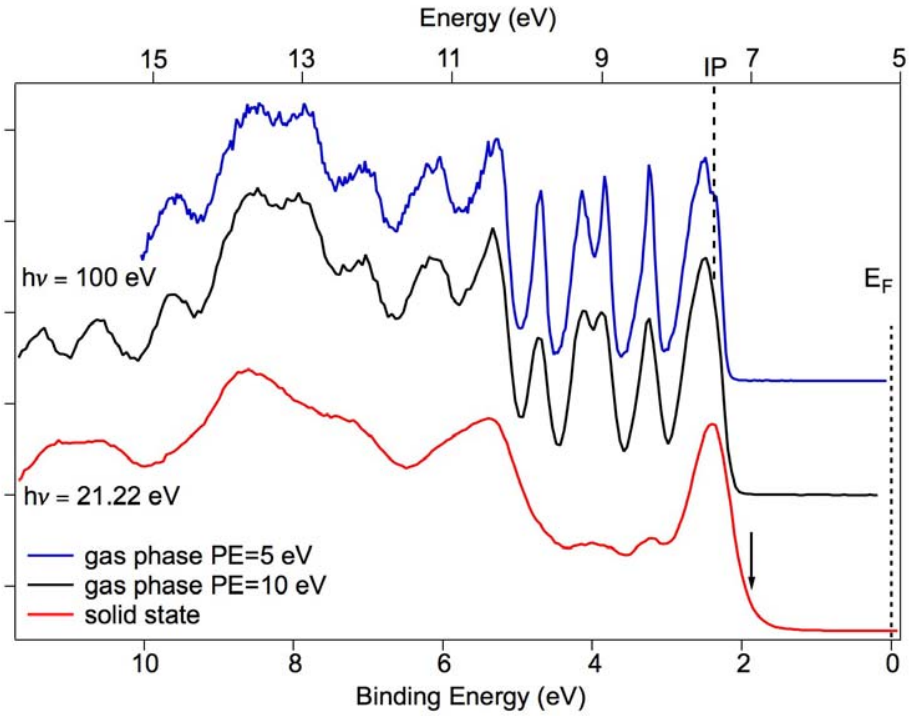

Figure SM2. Picene gas phase and solid state on Ag(111) valence band spectra. The gas phase spectra are referred to the vacuum level (top scale) and measured with hν = 100 eV. The solid state spectrum is referred to the Fermi level (bottom scale) and was measured with unpolarized light at hν = 21.22 eV (He I). The solid state value of the I.P. ("HOMO" state position in Fig. 1 of the main text) can be obtained by considering the work function (4.6 eV) plus the center of the HOMO feature at 2.3 eV from the Fermi level. Therefore the solid state I.P. is 6.9 eV, which has been claimed to be a characteristic of the surface [17]. On the other hand, considering the threshold of the HOMO band (indicated by an arrow) we obtain the threshold ionization potential, which is a characteristic of the bulk. The threshold I.P. results to be 6.4 eV. Therefore, the gap of 4.1 eV measured for picene must correspond to the difference between this energy and the corresponding threshold electron affinity [17]. The gap between the centroid of the "HOMO" band and the corresponding centroid of the "LUMO" bands must be higher than 4.1 eV (see Fig. 1 in the main text).
The gas phase spectra were measured at the GAS-PHASE beamline at Elettra with a total energy resolution of 0.1 eV.

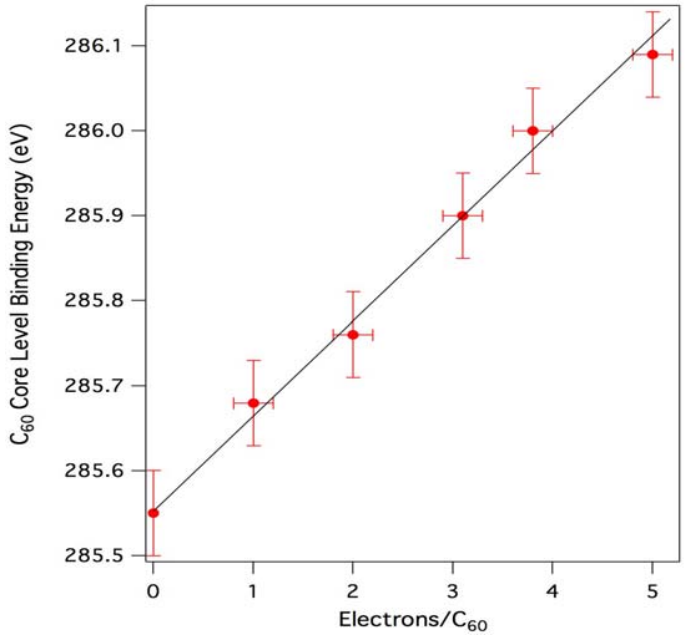

Figure SM3. Shift of the C1s XPS spectrum of C_{60} as a function of K doping. The energy change of the C_{60} component is linear with the charge estimated in Fig. 3.

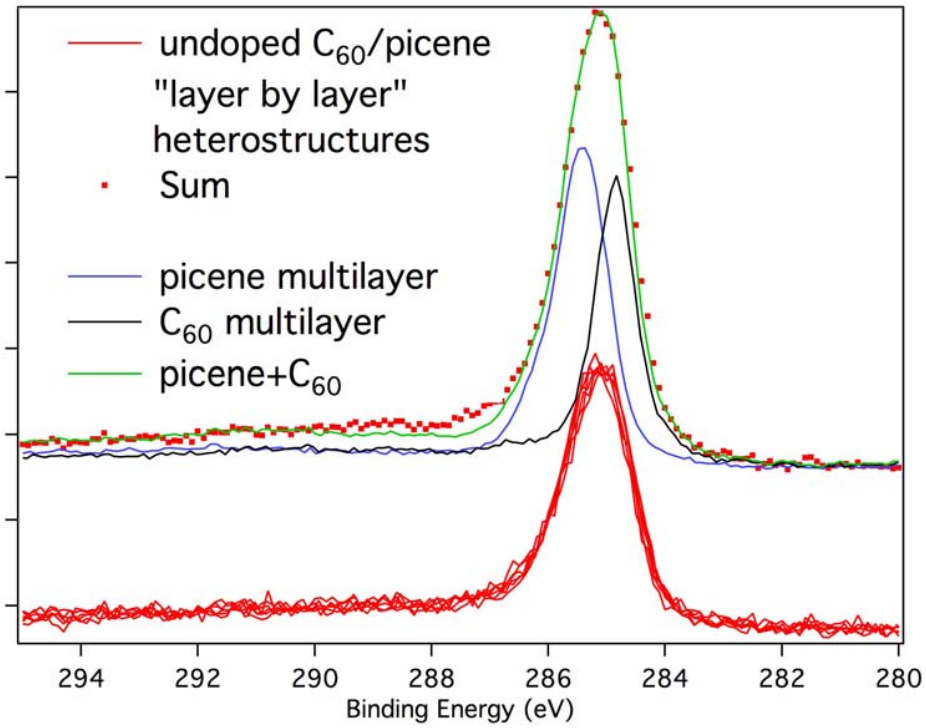

Figure SM4. The C1s spectra of all the undoped heterojunctions formed taken with the Mg Kα line. Note that the binding energy remains the same within 0.02 eV. The sum of these spectra (point) is the undoped spectrum reported in Fig. 4 of the main text. The picene and C_{60}

multilayer spectra, shifted by 0.8 eV and -0.6 eV respectively, and their sum (green line) are used to fit the undoped spectrum (point).

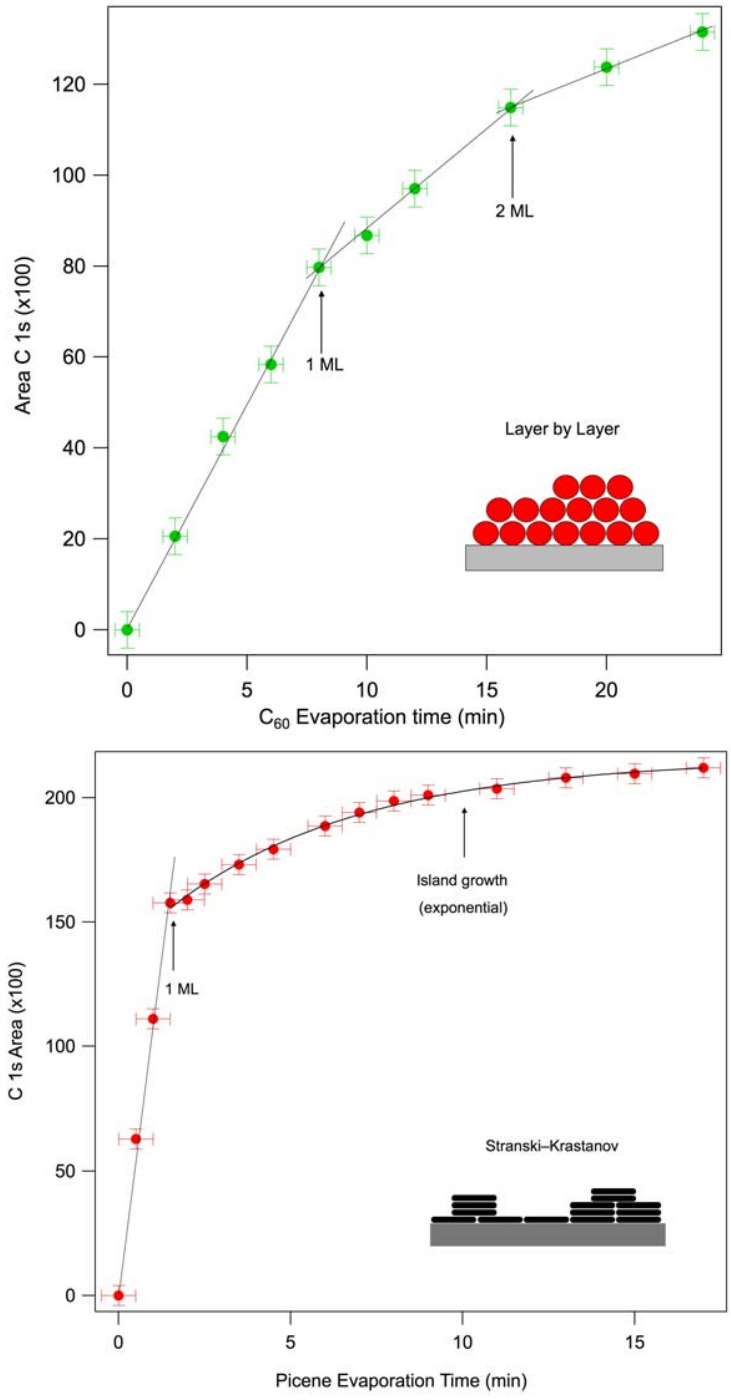

Figure SM5. Growth mode of a multilayer of C_{60} (top) and a multilayer of Picene (bottom) on Ag(111). For the heterojunction system we do not know the growing mode, but simply we deposited the equivalent of a monolayer of C_{60} on Ag(111) and the equivalent of a monolayer of picene on Ag(111) at every deposition, forgetting about the possible differences in sticking

coefficients. The evaporation times for the equivalent deposition of 1 ML were extracted from the above data.

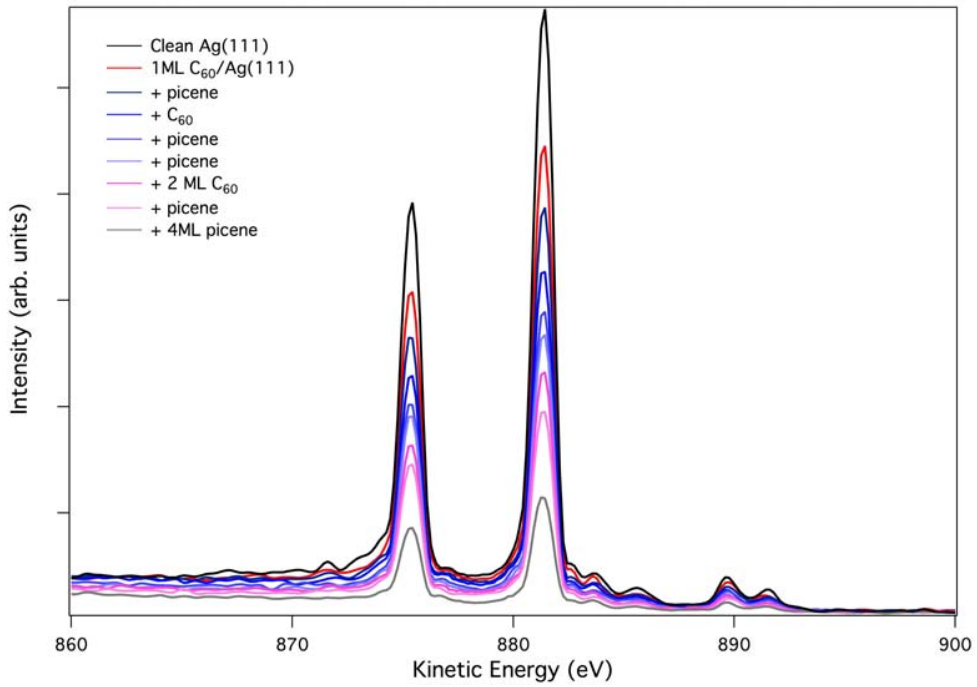

Figure SM6: Ag 3d core levels corresponding to the several layers formed on top of Ag(111) clean surface. Considering the attenuation from clean Ag(111) to 0.5 ML C_{60}/Ag(111) and assuming that 1 ML of C_{60} matches a thickness of 7 Å, the total thickness after all the deposited layers is roughly 35 Å.

4

Patterning PEDOT:PSS and tailoring its electronic properties by water-vapour-assisted nanoimprint lithography

The pursuit of higher efficiency is not the only research line in photovoltaic. Moving from crystalline materials to molecular solids open up new perspectives. The most intriguing one is of course the possibility to have flexible devices [37], adaptable to any surface for integrations in buildings or vehicles, but also to wears, in line for the future wearable electronics [38, 39].

However, even if the active organic blend is composed by molecular materials, the electrode were the cell is build on are still metals and ITO-covered glass. New materials have to be found in order to have highly efficient and flexible devices, one of these could be PEDOT:PSS, a conductive polymer.

In this paper we investigated the electronic properties of PEDOT:PSS after nano imprint lithography and the effect this have on the efficiency of an OPV cell. Thanks to nano imprint lithography it has been possible to create nanostructures with sub-100 nanometres resolution, hence having a substrate with an optimal morphology to overcome the short exciton diffusion length in OPV ($\sim$10 nm [8]). Nano imprint lithography was also able to increase the polymer conductibility of five order of magnitude and decrease the work function of 1.5 eV. All these effects has been found to increase the efficiency of the reference P3HT-ICBA organic cell of more than 60%.

RSC Advances

PAPER

View Article Online
View Journal | View Issue

Cite this: *RSC Adv.*, 2014, **4**, 34014

Patterning PEDOT:PSS and tailoring its electronic properties by water-vapour-assisted nanoimprint lithography†

Andrea Radivo,[ab] Enrico Sovernigo,[ac] Marco Caputo,[d] Simone Dal Zilio,[a] Tsegaye Endale,[e] Alessandro Pozzato,[c] Andrea Goldoni[d] and Massimo Tormen*[ac]

Received 21st May 2014
Accepted 23rd July 2014

DOI: 10.1039/c4ra04807e

www.rsc.org/advances

We present a new water-vapour-assisted nanoimprint lithography (NIL) process for the patterning of the conducting poly(3,4-ethylenedioxythiophene):poly(styrenesulfonate) (PEDOT:PSS). The process was optimized with respect to relative humidity, applied pressure and temperature (RH, *p*, *T*). The control of environmental humidity was found to be crucial. High quality nanostructures were reproducibly obtained at high relative humidity values (RH $\gtrsim$ 75%), with sub-100 nm resolution features attaining aspect ratios as high as ~6 at ~95% RH. The developed process of water-vapour-assisted NIL (WVA-NIL) strongly affects the electronic properties of PEDOT:PSS. By current–voltage measurements and ultraviolet photoemission spectroscopy we demonstrate that the process parameters *p*, *T* and RH are correlated with changes of PEDOT:PSS conductivity, work function and states of the valence band. In particular, an increase in the films conductivity by factors as high as 10^5 and a large decrease in the work function, up to 1.5 eV, upon WVA-NIL processing were observed. Employed as an anode buffer layer in P3HT:ICBA bulk heterojunction solar cells, PEDOT:PSS processing was found to affect significantly the device performance.

1. Introduction

Owing to its huge economic growth potential, organic optoelectronics is a field of intense applied research and a very attractive new market for innovative companies. The development of technologies based on conjugated materials for energy conversion (*e.g.* photovoltaic cells[1]), energy storage (*e.g.* supercapacitors[2]), or energy saving (*e.g.* lighting by OLEDs[3]) is boosted by the prospect of cheap, lightweight, flexible and environmentally friendly devices, produced over large area substrates by high throughput techniques[4–8] as already successfully demonstrated by the market of OLED displays (smartphones, TVs).

The architectures of organic semiconductors based devices are in many cases rather simple. They essentially consist of stacks of planar layers, patterned at the scale of tens to hundreds of micrometres[9] by methods such as ink-jet[10,11] screen printing[12] or laser ablation.[13] The development of organic-based devices is not subject to any roadmap of features' downscaling, analogous to that that in silicon-based microelectronics is referred to as the Moore's law. Nonetheless, new device architectures are calling for an extension to the sub-100 nm scale of the technologies suitable for the patterning of conjugated materials.[14–16]

Here we explore the patterning at that scale of poly(3,4-ethylenedioxythiophene):poly(styrenesulfonate) (PEDOT:PSS). The π-conjugated polymer (PEDOT) together with the polyanion (PSS) dispersed in water is currently the most frequently used anode buffer layer on Indium Tin Oxide (ITO) transparent electrode for its relatively high conductivity, high work function, mechanical flexibility, stability, transparency and easy processing in thin films by spin coating, inkjet printing, airbrushing, doctor blading. PEDOT:PSS is widely used for organic thin-film transistors (OTFTs), organic light-emitting diode (OLED) displays and in organic photovoltaic device (OPV), and has been also demonstrated as catalytically active anti-corrosion electrode in photoelectrochemical cells,[17,18] in ionic charge storage medium for super capacitors,[19,20] or as stable, biocompatible, implantable electrodes for *in vivo* neuronal activity recording.[21]

PEDOT:PSS, similarly to other anode buffer layers, is introduced so as to (i) provide an ohmic contact with p-type organic materials; (ii) to transport positive charges efficiently, (iii) to block negative charges.[22] In addition it should present low

[a]*Istituto Officina dei Materiali-CNR, Laboratorio TASC, I-34149 Trieste, Italy. E-mail: tormen@iom.cnr.it; Tel: +39 0403758416*
[b]*University of Trieste, Piazzale Europa, I-34127 Trieste, Italia*
[c]*ThunderNIL srl, via Ugo Foscolo 8, 35131 Padova, Italy*
[d]*Sincrotrone Trieste SCpA, I-34149 Trieste, Italy*
[e]*Department of Chemistry, Addis Ababa University, P. O. Box: 1176, Addis Ababa, Ethiopia*

† Electronic supplementary information (ESI) available. See DOI: 10.1039/c4ra04807e

series resistance (R_s) and act as a planarization layer for the often-rough ITO surface, so as to prevent electrical shorts and increase device yield. Moreover, it is very actively investigated as an option to fully replace the expensive ITO.[23–28] The improved contacts that PEDOT:PSS provides to most p-type organic semiconductors compared to bare ITO, is usually explained to arise from the PEDOT:PSS higher work function (reported to be between 4.8 and 5.2 eV) *versus* that of ITO (~4.7 eV). This would thus result in a reduction of the barrier for hole injection from the deep-lying HOMO levels of many conjugated semiconductors.[29,30]

Past investigations have highlighted severe hurdles in nanopatterning PEDOT:PSS by standard lithographic techniques. At the micrometre scale several methods[31] have been successfully applied, such as soft lithography,[32] inking and stamping,[33] pulsed UV laser patterning,[34] inkjet printing, screen printing in roll to roll system.[35] However, extending the previous techniques to the patterning of PEDOT:PSS at the sub-micrometre scale proved to be non-viable.

Therefore, we concentrated most efforts on nanoimprinting lithography (NIL) in spite of the modest success to patterning PEDOT:PSS by this technique to date.[36,16] The main problems of applying the standard NIL protocols to PEDOT:PSS are related to the thermo-mechanical properties of this material. In fact, it decomposes with temperature prior to exhibiting a distinct glass transition, while at room temperature and standard lab condition, due to its strong tendency to water uptake from environmental humidity, the material is sticky and with low internal cohesion. This leads to nanostructures prone to being easily damaged or ripped-off from the substrate during the separation of the stamp (step that we will refer to "demoulding") at the end of the NIL process.[37] Organic plasticizers, such as sorbitol,[38] glycerol[39] have been used to enhance the material flow, yet with partial success.[40,41] PEDOT:PSS is a composite material, with grains consisting of a rigid, conductive and hydrophobic PEDOT-rich core and a hydrophilic, soft and non conductive PSS-rich shell, with electrical and mechanical proprieties that are heavily influenced by the water content. In solution PEDOT clusters are kept in colloidal suspension by the PSS shell, and their size in solution has been shown to depend strongly on temperature and concentration.[42,43] When spin coated the resulting films show a highly anisotropic structure with flattened colloids into PEDOT-rich "lasagne-like" structures separated by PSS-rich lamellas. Water uptake from the atmospheric moisture is for thin PEDOT:PSS film very fast (in the matter of seconds for sub-100 nm thick films) and reversible, leading in the end to an equilibrium with the humidity of the environment. This effect results in a change in volume and modifies quite heavily the mechanical behaviour of PEDOT:PSS from brittle, in dry environment to plastic in wet environment. Lang *et al.* for instance reported a change of the Young's modulus from 2.8 GPa at 23% RH to 0.9 Gpa at 55% RH, and of the tensile strength from 53.2 MPa to 22.2 MPa in the same RH range,[37] owing to PEDOT:PSS water uptake.[38]

Several attempts at modifying the standard thermal NIL protocols so as to cope with the peculiar thermo-mechanical behaviour of PEDOT:PSS have been reported. An approach consisted in carrying out the imprinting process under water saturation conditions, using water vapour like a plasticizer.[44] By this technique 40 nm height features with sub-100 nm critical dimension of a silicon stamp could be successfully reproduced into PEDOT:PSS. Another method, that consisted in placing with no additional load an elastomeric stamp with hydrophilic surface on a PEDOT:PSS film followed by annealing has been demonstrated for shallow structures ($h = 10$ nm depth, 700 nm period grating).[45]

A different method consisted of pre-treating the PEDOT:PSS film for 24 h at low relative humidity (15% RH), followed by a nanoimprint lithography step at 100 °C in ambient air (at 45% RH). This NIL process exploits the higher Young's modulus of PEDOT:PSS with low water content, in order to avoid structures to be damaged during the demolding, yet sufficient plasticity to undergo deformation under pressure. Grating of lines of 70 nm in width and 60 nm in height, corresponding to an aspect ratio (AR) of 0.86 were reported in this case.[46] In all cases, only very shallow nanostructures could be obtained, a limitation that we intended to overcome.

Given the strong effect of RH on the PEDOT:PSS mechanical properties in the development of a nanoimprint lithography process here reported we have focused our attention on this parameter. Humidity was found to play a crucial role in the process, and high quality high aspect ratio nanostructures were reliably and reproducibly obtained in a process window at high RH, close to water vapour saturation. Surprisingly, the process of nanopatterning entails very strong effects on conductivity, work function and electronic states of the valence band. This fact may open new opportunities for tailoring PEDOT:PSS properties for specific optoelectronic applications.

2. Results and discussion

2.1 Water-vpour-asisted nanoinprint litholraphy

The peculiarity of the new Water-Vapour-Assisted NIL (WVA-NIL) process consists of taking advantage of the changes in the PEDOT:PSS thermo-mechanical properties induced by a controlled drop of RH in the atmosphere surrounding the sample, between stamp indentation and stamp release. In particular, during the indentation the PEDOT:PSS film should contain a sufficient amount of water to be soft and deformable at moderate temperature. On the contrary, small residual amount of water should be present during the stamp separation to benefit from a higher PEDOT:PSS internal cohesion and from the shrinkage upon drying of the features. This last aspect results in a frictionless extraction of the stamp from the complementary features during demoulding.

The Fig. 1 shows the scheme of WVA-NIL process. PEDOT:PSS films are first prepared by spin-coating. The thickness investigated in this study ranges between 32 and 350 nm. For the deposition of "thick" layers (>50 nm) the starting commercial solution, the CLEVIOS P VP Al 4083, was pre-concentrated by partial evaporation of water (by hot stirring in air) and filtered with 450 nm pore diameter cellulose acetate filters.

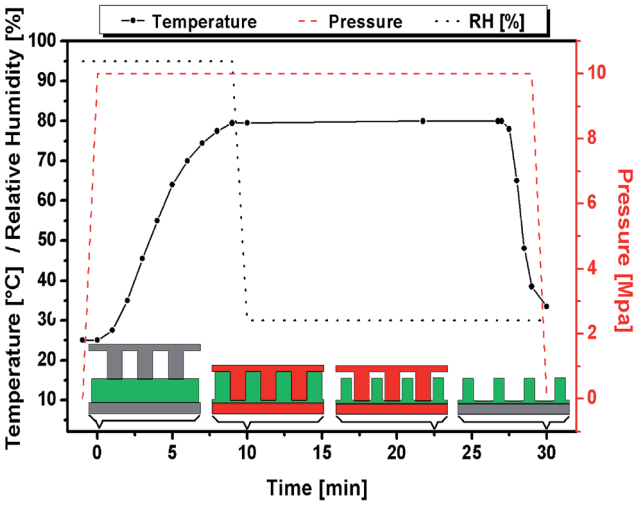

Fig. 1 The water-vapour-assisted NIL process. Example of a cycle carried out at 80 °C, 10 MPa and 95% RH.

After deposition, PEDOT:PSS film is equilibrated with the surrounding atmosphere, maintained at controlled relative humidity and at room temperature. The stamp is put face down onto the sample. Pressure is applied and the heating ramp is started. The RH set initially is maintained until the pre-set temperature for the imprinting process is reached. After a dwell time at these conditions the RH of the surrounding atmosphere is lowered. The PEDOT:PSS film, confined between substrate and stamp, dries from the edges inwards, which causes the shrinkage of the nanostructures. Finally, the plates are cooled down and the stamp is separated from the film/substrate. The fact that the drying starts from the edges and progress towards the centre of the sample does not result in any appreciable non-uniformity in the pattern quality nor in the physical properties of the film up to the tested samples size of 25 × 25 mm^2.

The above process scheme has been tested in a wide process parameters' window, *i.e.* in the range 0–100% of RH, 25–150 °C of temperature, and 2–12 MPa of pressure. The results obtained at fixed pressure of 10 MPa and for different temperatures and different RH are summarized in Fig. 2. Imprinting tests at 0% RH (done in a nitrogen-filled glovebox) showed that no pattern at all could be obtained in the 25–150 °C range, and only at temperature and pressure as high as ~250 °C and ~60 MPa, respectively, PEDOT:PSS plastic deformation could take place (Fig. 2b, micrograph A), resulting anyhow in the formation of shallow structures. Moreover, at 0% RH, 250 °C and 60 MPa the presence of brittle fractures in the resulting structures was observed. In general, the width of the PEDOT:PSS features imprinted in dry conditions (0% RH) exactly reproduces that of the mould, which results in a friction force exerted during stamp separation. Conversely, to test the mechanical stability of dried PEDOT:PSS nanostructures (produced by WVA-NIL in humid environment and dried afterwards), we applied with the help of a flat stamp a pressure of 20 MPa at 0% RH and 150 °C on a PEDOT:PSS grating. No deformation of the original

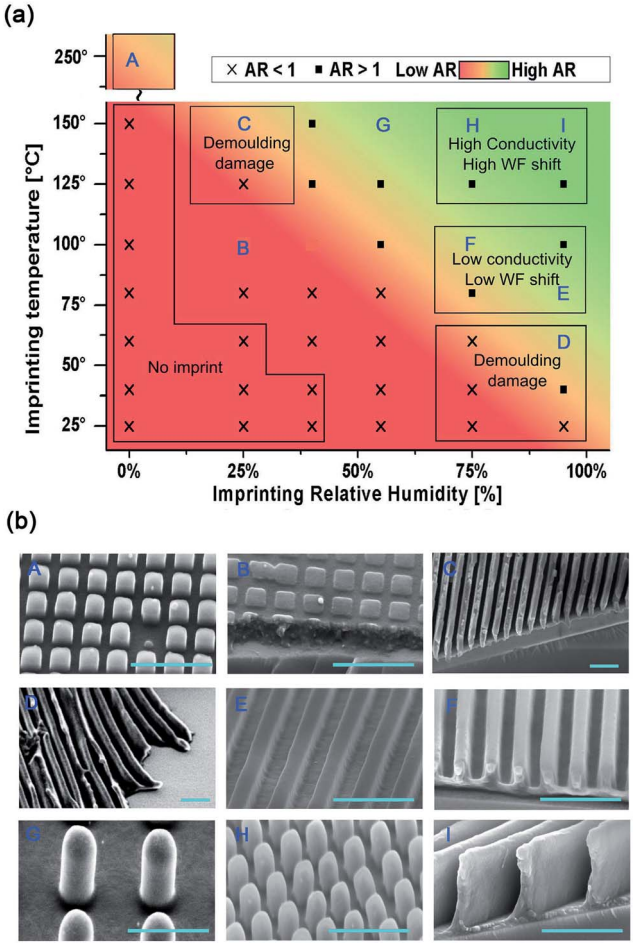

Fig. 2 (a) WVA-NIL process window. Systematic experiments were made in order to determine the optimal process window. In the experiments, silicon stamps with array of holes or gratings were used, fixing the applied pressure and the duration to 10 MPa and 30 min respectively, and varying the imprinting temperatures and relative humidity. Lithographic results were characterized by SEM and the regions of the (*T*, RH) plane were qualitatively classified on the basis of the aspect ratio and integrity of the structures. The regions were classified as suitable for high aspect ratio (AR > 1), for low aspect ratio (AR < 1), not suited for imprinting, or characterized by stamp release issues (ripping-off of the structures or collapse during demoulding). (b) Scanning electron micrographs of nanoimprinted PEDOT:PSS structures obtained at different temperature and RH (and at fixed 10 MPa, with the exception of sample A), identified in the process window map (a) by capital letters. Imprinting at 0% RH, 250 °C requires high-pressure (60 MPa) to occur (A). Insufficient water content, 25% RH, leads to shallow indentation at 100 °C (B) or to brittle fractures at 150 °C (C). At 95% RH the structures imprinted at temperatures as low as 60 °C were severely distorted and ripped-off during demolding (D). Structures of moderate aspect ratio (1 < AR < 2) can be obtained at 95% RH and 80 °C (E), 75% RH and 100 °C (F), or 55% RH and 150 °C and (G). Structures of aspect ~2, such as the 180 nm period array of pillars with square cross-section shown in (H) were imprinted at 75% RH and 150 °C. Lines of ~60 nm width and 400 nm height, corresponding to AR > 6 in a 180 nm period grating were obtained at 95% RH and 150 °C (I). Scale bars are 500 nm.

structures was detected, which leads to the idea that nanostructured PEDOT:PSS films could serve themselves as stamps or could be permanently indented as nanopatterned electrodes into various conjugated materials. This would open a new strategy for the fabrication of organic optoelectronic devices with novel architectures.

At 25% RH, imprinting of PEDOT:PSS was found feasible. At 100 °C the imprinted features were shallow (Fig. 2b, micrograph B), while at 150 °C they appear fully indented (Fig. 2b, micrograph C). However, in the latter case, we did not detect any appreciable lateral shrinkage of the features, which leads to the build-up of friction forces between PEDOT:PSS and stamp during the demolding and explains why the resulting structures were partially damaged.

At 100% RH (*i.e.* vapour saturation), the PEDOT:PSS film becomes unstable, with a tendency to de-wetting, resulting in poor and irreproducible imprinting results. However, slightly below saturation (90–95% RH) the previous issues disappear. Nevertheless, at temperatures below 60 °C the film could not be dried in a reasonable time, arbitrarily set to 30 min, and consequently the structures in the film were severely distorted or ripped away during demoulding (Fig. 2b, micrograph D).

A convenient process window in the (RH, *T*) plane, leading to features exceeding AR of 1 was identified in the approximately triangular region defined by the vertexes (40% RH, 150 °C), (95% RH, 150 °C) and (95% RH, 80 °C). The imprinting processes of Fig. 2b, micrographs E, F, G, H, I were conducted in that region.

Structures of moderate aspect ratio (1 < AR < 2) were obtained at 95% RH and 80 °C (micrograph E), and 75% RH and 100 °C (micrograph F). Structures of increasing AR were obtained at 150 °C by increasing the relative humidity, from 55% (micrograph G) to 75% (micrograph H), and 95% (micrograph I).

The optimal WVA-NIL process parameters for the fabrication of high AR nanostructures is represented by the region at high RH and high temperature such as ~95% RH, ~150 °C and ~10 MPa (micrograph I). At these conditions the excellent plasticity of the material and the fast evaporation of water results in a relatively short process time, leading to high AR structures, easily and reliably separated from the stamp, owing to a shrinkage of up to 20–25% of the features' width (Fig. 3).

The WVA-NIL process was extensively tested using different silicon stamps with features ranging from 80 to 250 nm, and height from 100 to 500 nm. In none of the tested imprinting conditions, even at temperatures and pressures of 200 °C and 30 MPa, the residual layer could be reduced below 20–30 nm.

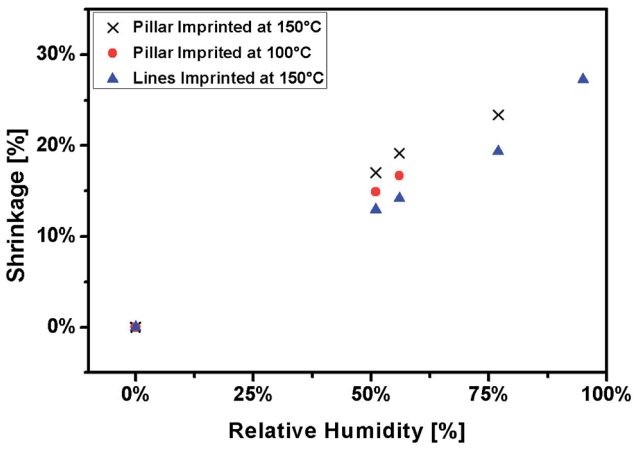

Fig. 3 Linear shrinkage of features' cross section as a function of the relative humidity set initially for the WVA-NIL process for lines and pillars imprinted at 10 MPa. No significant difference in the shrinkage was found for gratings of different period in the 180–500 nm range.

2.2 Effects of WVA-NIL process on the physical properties of PEDOT:PSS

Having identified a convenient parameters' window for the water-vapour-assisted NIL process, the attention has to be focused on the effects that this process has on the PEDOT:PSS electronic properties, in particular on the conductivity, work function, and density of states in the valence band.

2.2.1 WVA-NIL effects on PEDOT:PSS conductivity. It is well known that PEDOT:PSS physical properties strongly depend on the relative amount of PEDOT and PSS, but that they can also be affected by the chosen processing conditions or by adding high boiling solvents (HBS) to the dispersion,[47–51] Pettersson *et al.* revealed the effect of sorbitol on the refractive index and extinction coefficient.[48] Jönsson *et al.* found a 600-fold increase of conductivity and an increase by a factor of 2–3 of the ratio of PEDOT-to-PSS at the film surface by adding various solvents to the dispersion.[49] Kim *et al.* investigated the temperature-dependent conductivity of PEDOT:PSS doped with different solvents such as methyl sulfoxide (DMSO), *N*,*N*-dimethylformamide (DMF), tetrahydrofuran (THF), deducing that the screening effect of the solvent plays an important role in the variation of the conductivity.[52]

Other works highlighted the fact that the deposition by spin-coating itself introduces an anisotropy caused by the squeezing of PEDOT:PSS colloids orthogonally to the substrate, which results in different in-plane and out-of-plane conductivities.[53,42] The effect of exposing PEDOT:PSS to temperatures exceeding 100 °C in the presence of oxygen and/or moisture was reported to slowly degrade the conductivity.[54] (Huang, Miller, de Mello, de Mello, & Bradley, 2003; Vitoratos *et al.*, 2009) Given, the strong PEDOT:PSS susceptibility to fine processing an compositional details, it is important to establish how the physical properties of this material are affected by the different WVA-NIL processing conditions.

The first observed effect of our protocol was that conductivity is enhanced by the pre-concentration of PEDOT:PSS water dispersion. In fact, films spin-coated from the concentrated dispersion showed ~1 order of magnitude increase in the film conductivity compared to those deposited from the pristine dispersion (Fig. 4a). This effect would be compatible with the formation already in the pre-concentrated dispersion of larger PEDOT:PSS colloids, which, according to the PEDOT:PSS conductivity model by Vitoratos *et al.*[54] is expected to lead to larger conductivity values. However, even more pronounced was

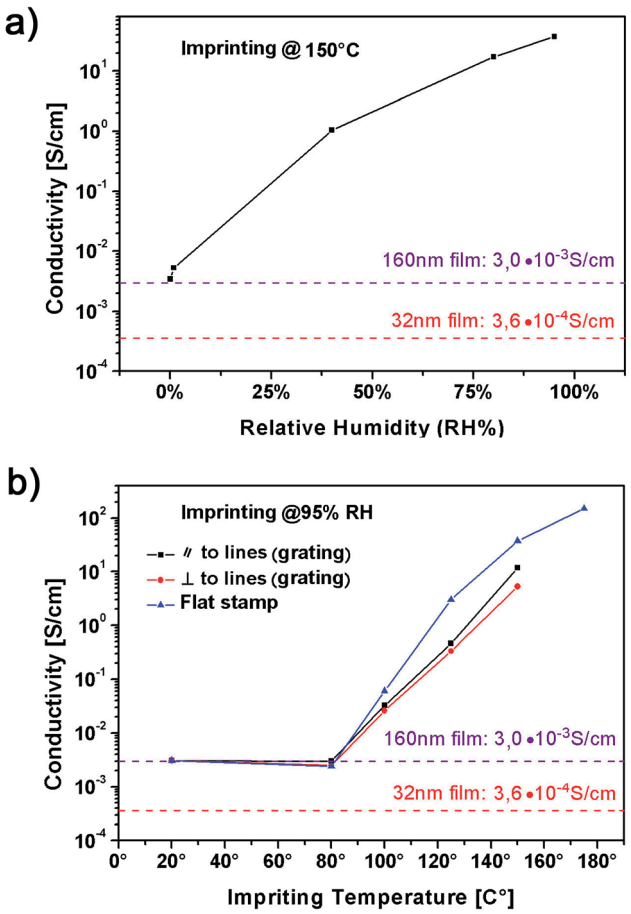

Fig. 4 In-plane conductivity of PEDOT:PSS films as a function of (a) the relative humidity and (b) the temperature set for the WVA-NIL process. The data refer to 32 nm thick film (dashed red line) spin-coated from the pristine PEDOT:PSS dispersion and to 160 nm thick film (dashed violet line) deposited from the pre-concentrated solution. The conductivities of the as-coated films are confronted to those of films processed by water-vapour-assisted NIL on thick films (160 nm) using a flat silicon substrate as a stamp. (a) Effect of RH on the conductivity of films imprinted at 150 °C and 8 MPa, and varying RH, from 0% to 95%. (b) Effect of imprinting temperature on conductivity of films imprinted with 250 nm period line gratings mould and flat silicon, at 8 MPa, 95% RH and different imprinting temperature in the 80–175 °C range. The lines are guides to the eye.

the effect arising from the WVA-NIL process. The conductivity was found to increase as a function of the RH. For WVA-NIL processes at high RH, enhancement by up to 5 orders of magnitude with respect to the pristine dispersion has been measured. This effect was limited to the areas actually compressed by the stamp, while areas not subjected to pressure were not affected. On the contrary, thermal NIL processes performed in glovebox (0% RH) left conductivity nearly unaffected. The effect on the conductivity depends also on the temperature at which the WVA-NIL process is carried out (Fig. 4b). Conductivity does not change for process temperatures up to 80 °C while it increases nearly exponentially, starting from ~100 °C. For all tested temperatures the conductivity was found to be independent of the applied pressure in the 2 to 12 MPa range. Only in the case of no load applied to the stamp, the conductivity showed only a weak, almost negligible increase, likely due to the ineffective confinement of the water vapour and the consequent faster drying of the film. This interpretation would also explain why WVA-NIL process performed with flat stamps results in an enhancement of conductivity exceeding that obtained with nanostructured stamps even if it does not involve any polymer flow. In fact flat stamps ensure a better water vapour confinement, while nanostructures provide easy paths for water escape. For given process parameters no major effect could be ascribed to the differences in the type and size of nanostructures (we varied AR from 1 to 5, for arrays or gratings of different periods). Only minor differences in the conduction were observed by measuring the resistivity in directions parallel and perpendicular to the lines.

The overall picture that emerges from the experiments is that the decrease of resistivity would not be related to any net polymer shear flow and consequent one-dimensional elongation of the PEDOT chains, but it would be an effect of "boiling" PEDOT:PSS in water. The understanding of what the "boiling" of the film entails at the level of PEDOT:PSS microscopic morphology is beyond the scope of this work. We speculate that it may have a similar physical origin as that of the so-called high-conductivity PEDOT:PSS state caused by inclusion of high-boiling solvents (HBS) in the dispersion. In fact, water remaining confined by the stamp during the WVA-NIL process in PEDOT:PSS films at temperatures well above 100 °C, may play the role of plasticizer, similarly to high-boiling solvents such as sorbitol, providing the mobility to PEDOT and PSS to rearrange during the annealing.

On the other hand, the effect of the presence of high boiling solvents in the dispersion on morphology is still controversial. Several explanation schemes have been proposed. Some authors explain this phenomenon in terms of phase segregation between PEDOT and PSS due to the higher relative mobility of the chains of both components with interposed HBS.[55] Rearrangement of PEDOT-rich clusters into elongated domains, has been reported in STM studies.[56] Conformational changes of PEDOT:PSS toward linear filamentary structures[57,58] or screening due to the polar character of HBS[59] are also invoked to explain the increased conductivity. Future work is required to better understand the microscopic effects on morphology of WVA-NIL process and whether our hypothesis of an analogy with the effect induced by HBS holds.

2.2.2 Effects of WVA-NIL process on PEDOT:PSS work function and valence band states. Water-vapour-assisted NIL impacts also on PEDOT:PSS work function and on the states of the valence band. This fact is presumably correlated to a change in the phase segregation between PEDOT and PSS already reported by other studies[38,60] and in particular to a reduction in the PSS content at the surface.[61] In fact, the work of Lee *et al.*[61] establish a clear correlation between work function and surface concentration of the PSS dopant, with work function increasing for increasing PSS-to-PEDOT ratio at the surface. This effect was confirmed by our XPS measurement (data presented in support information), in the opposite direction, *i.e.* a decreasing work function for decreasing PSS-to-PEDOT ratio.

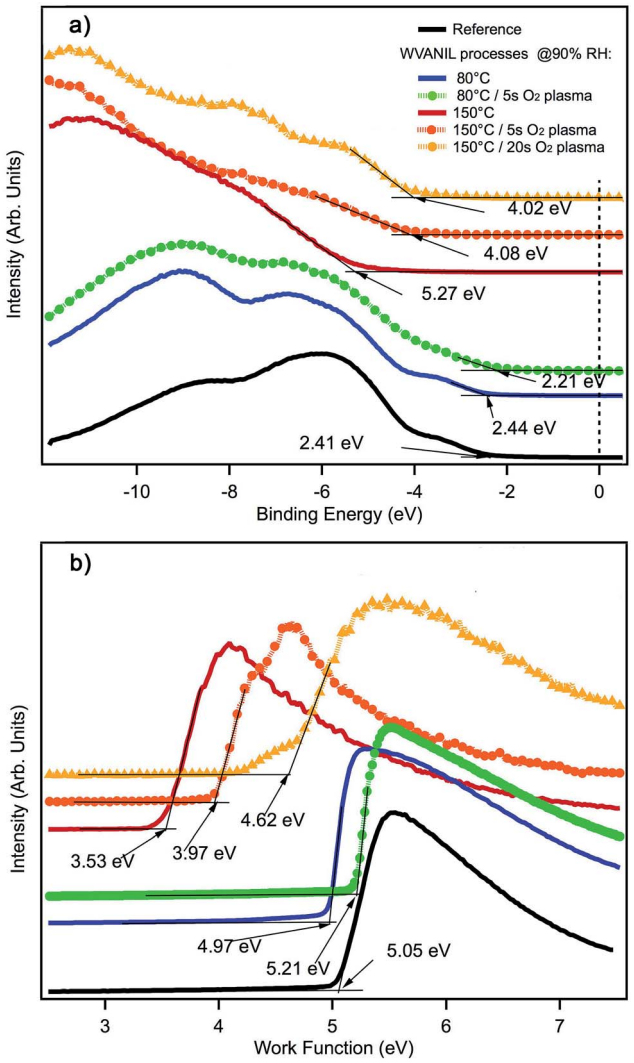

Fig. 5 UPS spectra for the pristine and WVANIL/oxygen plasma processed films. (a) Valence band and (b) edge of secondary electrons.

We have analyzed such effects by Ultraviolet Photoelectron Spectroscopy (UPS). Fig. 5a shows the valence band of a flat 160 nm thick PEDOT:PSS film on ITO (black spectrum) compared to that of films of the same thickness processed by WVA-NIL at 90% RH, but at different temperatures, namely, 80 °C (blue spectrum) and 150 °C (red spectrum). An additional treatment in oxygen plasma for 5 s of the sample processed by WVA-NIL at 80 °C leads to the green spectrum. The orange and yellow spectra refer to the sample processed at 150 °C and subsequently treated in oxygen plasma for 5 s and additional 15 s, respectively. Fig. 5b shows the measured work function of the same set of samples obtained by measuring the cut-off energy of the secondary peak.

The valence band spectrum of the as-deposited flat film (black spectrum) shows three main structures in the valence band in agreement with similar measurements already present in literature. In particular, the top of the valence band (peak centered at about 3 eV) can be extracted with a linear interpolation of the edge at about 2.41 ± 0.05 eV from the Fermi level. The work function is 5.05 ± 0.05 eV in good correspondence with the reported values in literature.[38,61,62]

In Fig. 5a it is evident that the WVA-NIL treatment at 90 RH% and 150 °C (red spectrum) strongly influences the valence band structures. Upon processing, all valence band peaks appear smeared out and the onset of the valence band shifts away from the Fermi level by about 2.9 eV (it is now at 5.27 ± 0.05 eV from the Fermi level). A concomitant decrease of the work function to about 3.53 ± 0.05 eV is observed, corresponding to a shift of 1.52 eV from the value of the untreated film (black spectrum). Interestingly, by subsequent oxygen plasma (5 s and 20 s, orange and yellow curves), the work function increases and valence bands appear to recover partially the lost structures with the edge shifting towards the Fermi level.

On the other hand, the NIL treatment at 90 RH% and 80 °C (blue spectrum) only slightly modifies the valence band features with the top of the valence band at 2.44 ± 0.05 eV from the Fermi level, very close to the value for the as-coated film. The work function decreases by less than 0.1 eV to 4.97 ± 0.05 eV.

The oxygen plasma treatment on the WVA-NIL processed sample at 90 RH% and 80 °C (green spectrum) slightly broadens the valence band features, but increases the work function at 5.21 ± 0.05 more than the level of the as-coated film. Most interesting is the shift of the valence band onset edge that now appears closer to the Fermi level, *i.e.* 2.21 ± 0.05 eV below it.

We try to rationalize the observed phenomenology based on the currently most accepted morphological model of the PEDOT:PSS system. This model depicts PEDOT:PSS morphology as consisting of colloids dispersed in water segregated into PEDOT-rich cores surrounded by PSS-rich shells, due to hydrophobic (hydrophilic) character of PEDOT (PSS). The core–shell structure is preserved to some extent also in the film. During the coating the colloids flatten into a lamellar structure of PEDOT-rich layers vertically alternated with PSS-rich ones.[42] PEDOT:PSS forms a surface layer that is highly enriched in PSS, with respect to bulk PSS/PEDOT ratio.[63,61] Furthermore, it is known that the work function correlates with the surface composition of the PEDOT:PSS film, which highly depends on the preparation processes such as thermal annealing process, solvent treatment and coating method.[62] In particular, higher PSS surface concentration leads to larger work function.[61]

Yun *et al.*[62] studied by UPS the electronic properties of PEDOT:PSS, reporting an increase of work function (from 5.0 to 5.2 eV) upon annealing for 1 h at 130 °C in ultra high vacuum (interpreted as the effect of desorption of contaminants), whereas for temperature higher than 170 °C the work function shifted gradually as a function of time towards lower values. For annealing temperatures of 220 °C and 290 °C for 3 h the work function reduced to 4.8 and 4.5 eV, respectively, and this progressive lowering of work function as the annealing temperature increases, correlates with a progressive reduction of the PSS at the film surface, probed by XPS. On the other hand the work function of the only PEDOT (not doped by PSS) has been reported to be in the range 4.0 ± 0.2 eV (ref. 64) or 4.3 eV.[65]

In our investigation on the WVA-NIL process the change of PEDOT:PSS work function was found, in the most dramatic

case, much larger than previously reported studies on the effects of thermal annealing.[62] Interestingly, the work function in the WVA-NIL process carried out at 90% RH and 150 °C lead to a work function smaller even than the reported value for the undoped PEDOT (4.0 ± 0.2 eV).

WVA-NIL, due to the confinement of water in the film while heating, ensures large relative mobility to the PEDOT and PSS chains. We presume that the lamellar structure of the PEDOT:PSS is disrupted and that a mixing at a finer level of the two components is reached, lowering the PSS content at the surface. The fact that the PSS-rich top surface is replaced by a phase more rich in PEDOT would explain the reduction in the work function.

2.3 Polymer photovoltaic cells on nanostructured PEDOT:PSS

We have investigated the impact that changes induced on the PEDOT:PSS electronic structure by WVA-NIL process and oxygen plasma produce on the *J–V* characteristics of poly(3-hexylthiophene) (P3HT): indene-C_{60} bisadduct (ICBA) bulk heterojunction solar cells. By studying a series of solar cells on PEDOT:PSS anode buffer layers on ITO-coated glass either as spin-coated or processed by WVA-NIL (experimental details are in ESI†), we observed that cells' characteristics are strongly correlated with the position of the conduction band edge and of the work function of PEDOT:PSS. This dependence is so marked that the potentially favorable increase of conductivity by several order of magnitude induced on PEDOT:PSS owing to WVA-NIL process is totally obscured by the unfavorable shift of the alignment with the HOMO level of the P3HT.

Though the *J–V* characteristics that we report here do not represent the state of the art in organic photovoltaics, the relative trends in cells performances as a function of the WVA-NIL process parameters and oxygen plasma treatment on PEDOT:PSS reveal very significant information. The modest value of efficiency (~1%) is explained by the following reasons. Our devices were made in N_2-filled glovebox with ~50 ppm residual oxygen and water, and characterized in open atmosphere without encapsulation. Their active area of 26 mm^2 was significantly larger than that of the reported best performing ones, which rarely exceed 1–4 mm^2 area. In our experience as well as in published research by others[66] the efficiency of larger cells underestimates by a factor 2–3 the efficiency of the small-area cell limit, where the power dissipation in the ITO owing to ohmic loss is negligible. Finally, the large variability of P3HT-based bulk heterojunction solar cells from producer and from batch it is well known.[67]

In spite of these factors, the reported trends may be very relevant also in the case of high-efficiency cells.

Fig. 6 shows the *J–V* characteristics and the main photovoltaic parameters, *i.e.* efficiency (η), short circuit current density (J_{sc}), open circuit voltage (V_{oc}) and fill factor (FF) under AM 1.5 simulated solar irradiation at 100 mW cm^{-2} intensity. Measures are referred to a set of polymer solar cells made on 300 nm period PEDOT:PSS gratings (~120/180 nm lines/spaces) by WVA-NIL at 95% RH and temperatures of 80, 100, 130, and 150 °C.

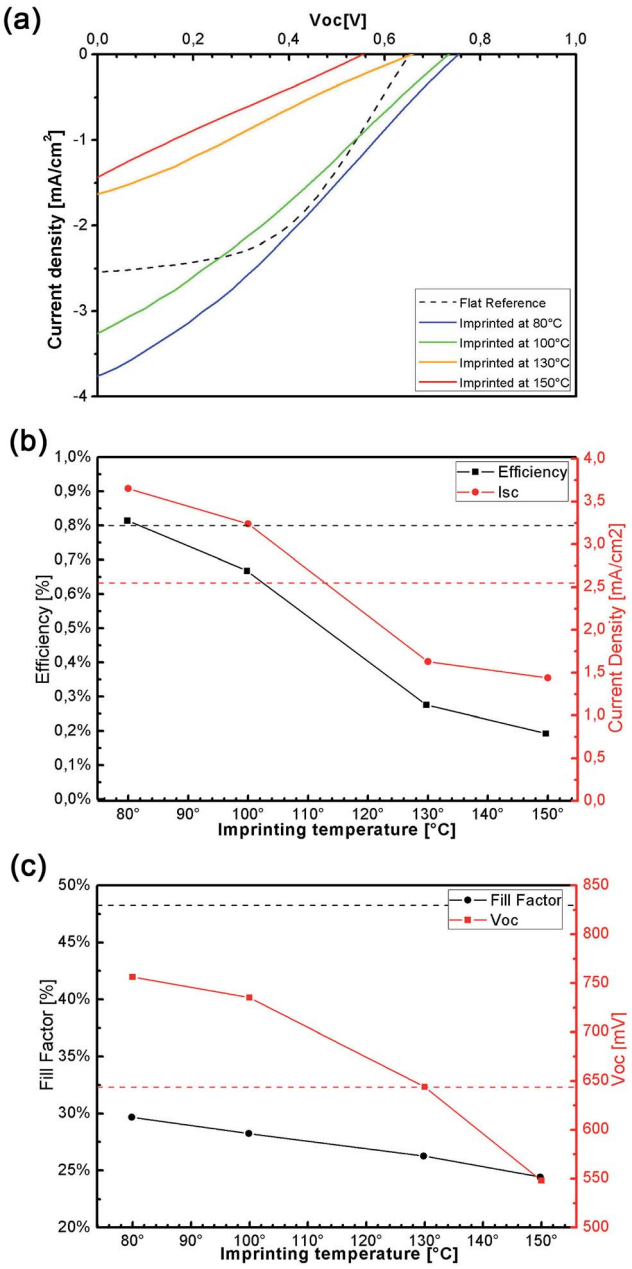

Fig. 6 Performance of P3HT:ICBA bulk heterojunction solar cells build on the pristine and WVA-NIL patterned PEDOT:PSS anode buffer layer. (a) *J–V* characteristics (b) efficiency and short circuit current density (c) fill factor and open circuit voltage for cells prepared on PEDOT:PSS patterned at different temperatures.

The *J–V* characteristics of the cells made on PEDOT:PSS patterned by WVA-NIL differ markedly from the reference cell made on the as-deposited 160 nm thick PEDOT:PSS film.

We observe that the cell on PEDOT:PSS patterned at 80 °C and the reference one feature approximately the same efficiency of ~0.8%. However, the patterned one exhibits larger J_{sc} and V_{oc} than the reference cell (3.5 mA cm^{-2} and 750 mV *vs.* 2.5 mA cm^{-2} and 650 mV, respectively) and lower FF (30% instead of 48%).

Increasing the WVA-NIL process temperature, which we saw previously to shift downwards the level of the PEDOT:PSS valence band edge, leads to a progressive reduction of J_{sc}, V_{oc} and FF of the cells. In particular, the lowering of the work function from 5.05 ± 0.05 eV to the 3.53 ± 0.05 eV by processing the as-deposited flat PEDOT:PSS with WVA-NIL at 150 °C results in a reduction of cell efficiency from 0.8% down to 0.15%. The reason for this behaviour, in spite of the increased hole conductivity in the PEDOT:PSS, must be searched in the new position of the valence band that with increased WVA-NIL temperature moves below the HOMO of the blend (increasing, therefore, the barrier for hole injection from the polymer to the PEDOT:PSS).

Interestingly, the shift of the valence band edge and the reduction of the work function in PEDOT:PSS due to WVA-NIL process at high temperature and high RH can be reverted by a subsequent oxygen plasma treatment, that tends to shift the top of the valence band towards the Fermi level (Fig. 5a). At the same time the efficiency of photovoltaic cells slightly increases (Fig. 7). Fig. 7 shows the current–voltage characteristics and the extracted values for η, J_{sc}, V_{oc} and FF of OPV cells fabricated on PEDOT:PSS nanopatterned by WVA-NIL at 80 °C and 95% RH. The pattern consisted of gratings of lines (250/250 nm lines/spaces) and were subsequently subjected to oxygen plasma for 0, 5, 30, 60 and 120 s.

On the other hand, the only WVA-NIL at 80 °C leaves all valence band features almost unaffected as in the flat sample with the onset of the valence band at 2.44 ± 0.05 eV from the Fermi level. The corresponding work function is 4.97 ± 0.05 eV and the measured efficiency is about 0.8% as for the reference cell. The oxygen plasma treatment only slightly broadens the valence band features, but increases the work function to 5.21 ± 0.05 even higher than that of the reference sample. Most interesting is the shift of the valence band onset that now appears at 2.21 ± 0.05 eV from the Fermi level, so reducing the barrier for the hole injection and consequently increasing the efficiency to 1.3%, *i.e.* 60% relative increase compared to the reference cell. By increasing the duration of the oxygen plasma to 1 min, the cells efficiency decreases to 1.1%, mainly due a drop in the current (whereas FF and V_{oc} remain essentially stable). Increasing further the plasma treatment to 2 min results in a drop to 0.7% efficiency by a combined drop of V_{oc} (from 800 mV to 525 mV) and FF (from 42.5% to 35%).

The observed trends as a function of WVA-NIL, temperature, and duration of oxygen plasma treatment show that the performances of cells tend to worsen for process conditions that increase the separation of the valence band edge with the Fermi level, possibly associated with the lowering of the work function.

In particular, the series of measurements as a function of the duration of oxygen plasma show an initial increase of efficiency for oxygen plasma etching of 5 s, and 20 s, according to the UPS measured shift of work function and valence band edge.

The results of this experiment agree with those of a study by Frohne *et al.*,[68] who studied the influence of the anodic work function on the performance of organic solar cells. In that case, they used an *ex situ* electrochemical procedure to alter the work

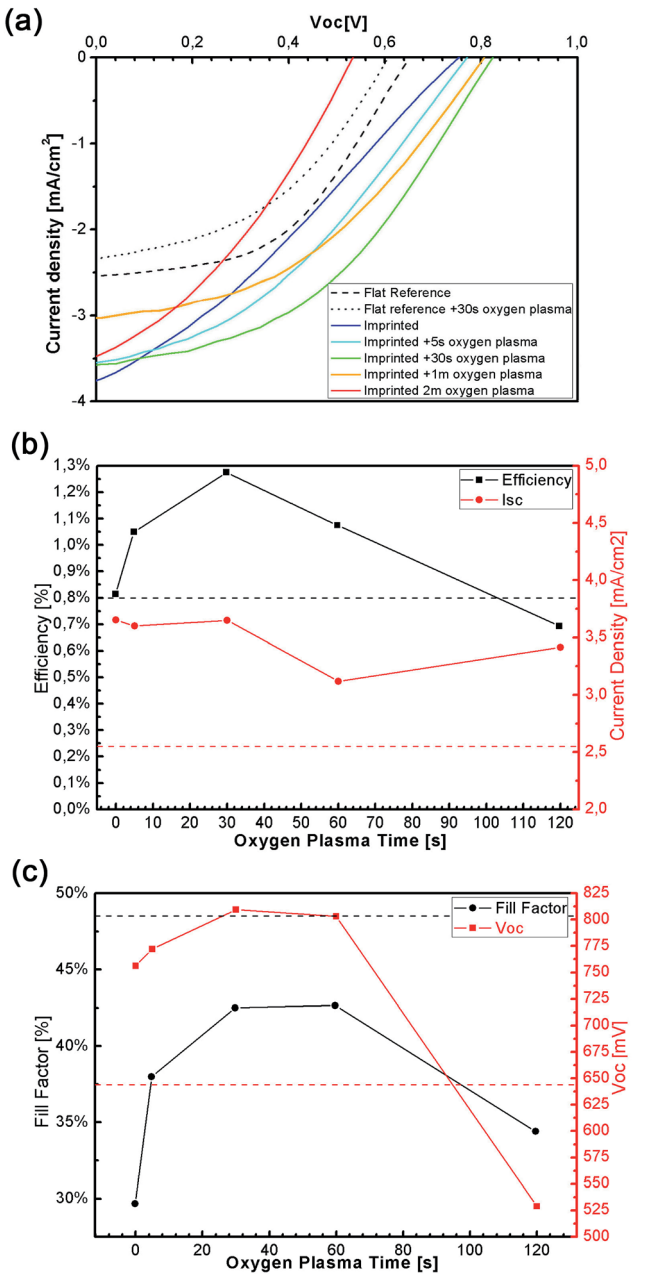

Fig. 7 Performance of P3HT:ICBA bulk heterojunction solar cells build on the pristine and WVA-NIL patterned PEDOT:PSS anode buffer layer at 80 °C and 95% RH as a function of an additional oxygen plasma treatment. (a) *J–V* characteristics (b) efficiency and short circuit current density (c) fill factor and open circuit voltage for cells patterned PEDOT:PSS treated in oxygen plasma for different time.

function of PEDOT:PSS, adjusting the equilibrium potential E_q *vs.* a standard electrode.[69] Frohne *et al.* showed that with decreasing E_q (*i.e.* decreasing work function) the *J–V* curves shifts progressively closer to the origin of axes, showing a progressive reduction in J_{sc}, V_{oc} and efficiency.[68]

Generally the doping of the PEDOT with PSS is associated also with a change in the optical properties of the material. This aspect has been investigated by UV-vis photospectrometry, but

no significant change in absorbance could be measured as the effect of WVA-NIL process.

3. Conclusions

We have systematically investigated a water-vapour-assisted nanoimprint lithography process for the patterning of PEDOT:PSS, exploring the space of parameter RH, p, and T. Relative humidity in the atmosphere surrounding the sample during the process of WVA-NIL plays a key role in the process. A reliable and reproducible nanoimprint lithography process has been developed, for the patterning of conductive PEDOT:PSS layers with lithographic results of unprecedented quality. It was found that the NIL process window lies in the region of temperature/relative humidity between 80 and 100 °C and 75 to 95%, where sub-100 nm features with aspect ratio up to 6 have been achieved.

The process affects the electronic properties of PEDOT:PSS. In particular conductivity can be enhanced approximately by 5 orders of magnitude, work function can be decreased down to 3.5 eV, and valence band edge shifts by up to 3 eV. This may represent an opportunity to use PEDOT:PSS also as a cathode and not just as anode in optoelectronic applications.

The possibility of tailoring PEDOT:PSS electronic properties has a strong impact in organic photovoltaic cells performance, and implications may be relevant to other type of devices for energy conversion or storage. The testing of the WVA-NIL processed PEDOT:PSS in organic photovoltaic cells showed a clear effect associated to the shift of work function and the shift of the edge of the valence band. In particular, a shift towards the Fermi energy of the valence band edge leads to an overall improvement of cells performance, while a shift in the opposite direction is associated to a worsening of the performance.

The availability of a patterning process for PEDOT:PSS and the mastering of its effects on key physical properties of the latter may open new opportunities in energy-related applications of conjugated materials.

4. Material and methods

4.1 Substrate preparation

PEDOT:PSS films were deposited on 3 different types of substrate, namely Si (100), chosen for its easy cleavage in the preparation of cross-view SEM samples for the characterization of the lithographic results, Si(100) with 200 nm of thermal SiO_2 layer for the measurement of the PEDOT:PSS conductivity, and OLED Grade ITO Coated Glass with 15 Ω per sq (Visiontek Systems Ltd) for the fabrication of photovoltaic cell and for UV-vis absorbance measurement. The substrates were all thoroughly cleaned in class 1000 clean room using the same procedure, consisting of 30 minutes sonication in demineralised water with a detergent, and the sequential dipping in hot acetone, IPA, and Milli-Q water. After drying under nitrogen stream the cleaning procedure is concluded with oxygen plasma for 5 minutes to improve the wetting of the substrate by the aqueous dispersion of PEDOT:PSS. The cleaning is done and the substrate were used shortly after cleaning and oxygen plasma.

4.2 Pre-concentration of the PEDOT:PSS dispersion and spin-coating

The PEDOT:PSS films were produced by spin coating using a commercial aqueous solution of PEDOTT:PSS, "P VP Al 4083" from H. C. Starck, a low conductivity PEDOT:PSS commonly used for OPV for its good film forming properties. As the achievable films thickness range (30–70 nm) was unsufficient for the patterning tests of high aspect ratio structures, the dispersion was pre-concentrated by partial evaporation of the water by magnetic stirring the solution in a glass vial open to air on a hot plate. The obtained dispersion is unstable at high pre-concentration levels (typically 50% volume reduction) and needs to be cooled down and rested for 24 h in a refrigerator to be stabilized, ensuring reproducibility in the thickness of the spin-coated films. Both pristine and pre-concentrated dispersions were used immediately after removal from the refrigerator (at 5 °C), and filtered at the moment of the deposition with a 0.45 μm cellulose acetate filter. The spin coating was done by dropping the solution on the substrate already in rotation. The rotational speed was set between 1000 rpm to 3000 rpm depending on the final needed thickness. The film thickness reproducible within ±5 nm as measured by profilometry.

4.3 Control of environmental humidity and sample handling

The samples were used either immediately after, or within 24 h from the spin-coating of PEDOT:PSS. In the latter case, the samples were maintained at the environmental humidity and were equilibrated with the WVA-NIL processing humidity for 5 minutes prior to the imprinting. The control of relative humidity was achieved by different means.

The imprinting tests at 0% RH were performed in a glovebox fluxed with nitrogen. In the range between 25% and 75% RH was controlled by setting the desired value in a clean room equipped with active humidification/dehumidification system (in this case all steps from storage to positioning, imprinting and demoulding could be done at constant RH). For the high humidity tests in addition to setting high RH values for the clean room, the humidity was increased locally with an home-made bubbler, by fluxing nitrogen into Milli-Q water, and delivering the water-saturated nitrogen in the gap between the press plates.

4.4 Nanoimprint lithography

For WVA-NIL experiments a PW 20 E hydraulic press with heating plates (Paul-Otto Weber GmbH), with maximum heating and cooling rates of 8 °C min^{-1} and 50 °C min^{-1} and maximum force of 200 kN. An electronic pressure gauge ensure the control of pressure with 0.2 kN resolution. For the experiments at 0% RH we used a home-made press with heating plates installed in glovebox.

Stamps were silicon gratings of lines with periods of 180 nm, 250 nm, 300 nm, 500 nm, height between 90 and 250 nm period

and duty cycle of 50%, or arrays of square or cylindrical holes in silicon of 180 and 500 nm period, respectively. Copies of the silicon stamps into Ormostamp (micro resist technology GmbH) on glass were used mainly for the patterning of PEDOT:PSS on ITO/glass, in order to solve a problem consisting in the disruption PEDOT:PSS features caused by the different thermal expansion of silicon stamps and ITO/glass substrates. By matching the thermal expansion of the substrates the previous problem disappeared. All stamps were surface functionalized by self-assembling of a monolayer of dodecyltrichlorosilane from vapour phase, to make their surface hydrophobic and ease the demoulding.

4.5 Oxygen plasma

Oxygen plasma treatment mentioned in the paper were performed with a 100 W RF power on 6″ cathode, pressure of 0.7×10^{-2} mbar and 115 V bias. For treatments of up to 30 seconds no significant change in the topography or in the conductivity were seen.

4.6 Conductivity measurement

The measurement of in-plane conductivity were made on as-coated, and WVA-NIL processed PEDOT:PSS films on SiO_2 (300 nm)/Si substrates. The WVA-NIL process was done using as a stamp either silicon gratings of lines, or flat silicon substrates. Contacts to PEDOT:PSS were made evaporation of 80 nm of gold by shadowing a stripe of the substrate with a calibrated metal wire, resulting in 220 μm gap between contacts, as measured by SEM. The resistance was obtained by a linear fit of the *I–V* curve between −2.0 V and 2.0 V. The conductivity for the patterned films were measured in parallel and orthogonal direction with respect to the lines. To extract the conductivity we used the value of film thickness as measured by profilometry (before patterning the film).

4.7 Scanning electron microscopy

SEM images of the NIL or WVA-NIL-structured PEDOT:PSS films were acquired on a Zeiss Supra 40 scanning electron microscope. The cross-sections of the samples were obtained after few minutes drying PEDOT:PSS films on at hot plate at 150 °C. Cleavage was done with the substrates still hot (cleavage without dehydration step lead to heavy plastic deformation of the PEDOT:PSS film).

4.8 UPS measurements

The UPS experiments were performed in a modified VG-II ESCAlab system (base pressure 10^{-10} mbar) using the He I radiation (21.22 eV). The electron hemispherical analyser worked with 2 eV of pass energy and the Fermi level was measured on the copper sample holder in electrical contact with the sample before each measurement. To obtain the work function relative to the measured Fermi level, a bias of 6.00 V was applied between the sample and the ground, in order to make visible the secondary photoelectron cut-off. The energy resolution was 50 meV.

4.9 OPV cell fabrication and testing

For cell production the PEDOT:PSS was deposited on patterned ITO substrate. The patterning of ITO was obtained by UV photolithography on the photoresist S1813 and wet etching of the ITO with a 10 : 10 : 1 HCl : H_2O : HNO_3 solution at 50–60 °C. Regioregular poly(3-hexylthiophene) (P3HT) polymer used in this work was obtained from Rieke Specialty Polymers, Rieke Metals Inc., while indene-C60 bisadduct (ICBA) from Lumtec Luminescence Technology Corp. After imprinting with Ormostamp/glass stamp, the PEDOT:PSS/ITO/glass samples were transferred in a nitrogen filled glovebox. Residual water and oxygen were approximately 50 ppm. Prior to device fabrication, a solution consisting of P3HT : ICBA in blend ratio of 1 : 1 (wt/wt %) and blend concentration of 40 mg mL^{-1} in dichlorobenzene was stirred at 40 °C for 36 hours inside glovebox. P3HT:ICBA solution was spin-casted onto the differently processed PEDOT:PSS films at 800 rpm for 50 seconds. Finally through shadow mask 100 nm thick aluminum contacts were vacuum evaporated at a pressure of approximately 2×10^{-6} Torr. After aluminum evaporation (with evaporator directly connected to glovebox) the devices were annealed at 140 °C for 30 minutes inside glove-box.

References

1 S. Günes, H. Neugebauer and N. Sariciftci, *Chem. Rev.*, 2007, **107**, 1324–1338.
2 K. Wang, H. Wu, Y. Meng and Z. Wei, *Small*, 2014, **10**, 14–31.
3 S. Reineke, F. Lindner, G. Schwartz, N. Seidler, K. Walzer, B. Lüssem and K. Leo, *Nature*, 2009, **459**, 234–238.
4 C. Dodabalapur, L. Filas, B. LaDuca and S. K. Li, *Nature*, 2000, **403**, 521–523.
5 S. Forrest, *Nature*, 2004, **428**, 911–918.
6 G. Malliaras and R. Friend, *Phys. Today*, 2005, **58**, 53–58, DOI: 10.1063/1.1995748.
7 H. Klauk, U. Zschieschang, J. Pflaum and M. Halik, *Nature*, 2007, **445**, 745–748.
8 H. Huitema, G. Gelinck, J. van der Putten, K. Kuijk, C. Hart, E. Cantatore, P. Herwig, A. van Breemen and D. de Leeuw, *Nature*, 2001, **414**, 599.
9 Y. Xu, F. Zhang and X. Feng, *Small*, 2011, **7**, 1338–1360.
10 T. Kawase, H. Sirringhaus, R. H. Friend and T. Shimoda, *Adv. Mater.*, 2001, **13**, 1601–1605.
11 P. Calvert, *Chem. Mater.*, 2001, **13**, 3299–3305, DOI: 10.1021/cm0101632.
12 D. A. Pardo, G. E. Jabbour and N. Peyghambarian, *Adv. Mater.*, 2000, **12**, 1249–1252.
13 D. G. Lidzey, M. Voigt, C. Giebeler, A. Buckley, J. Wright, K. Böhlen, J. Fieret and R. Allott, *Org. Electron.*, 2005, **6**, 221–228, DOI: 10.1016/j.orgel.2005.06.007.
14 P. Watkins, A. Walker and G. Verschoor, *Nano Lett.*, 2005, **5**, 1814–1818.
15 F. Yang and S. Forrest, *ACS Nano*, 2008, **2**, 1022–1032.
16 J. Weickert, R. Dunbar, H. Hesse, W. Wiedemann and L. Schmidt-Mende, *Adv. Mater.*, 2011, **23**, 1810–1828.

17 S. Mubeen, J. Lee, N. Singh, M. Moskovits and E. W. McFarland, *Energy Environ. Sci.*, 2013, **6**, 1633.
18 N. Singh, S. Mubeen, J. Lee, H. Metiu, M. Moskovits and E. W. McFarland, *Energy Environ. Sci.*, 2014, **7**, 978–981.
19 S. I. Cho and S. B. Lee, *Acc. Chem. Res.*, 2008, **41**, 699–707.
20 Y. Hou, Y. Cheng, T. Hobson and J. Liu, *Nano Lett.*, 2010, **10**, 2727–2733.
21 D. Khodagholy, T. Doublet, M. Gurfinkel, P. Quilichini, E. Ismailova, P. Leleux, T. Herve, S. Sanaur, C. Bernard and G. Malliaras, *Adv. Mater.*, 2011, **23**, H268–H272.
22 R. Po, C. Carbonera, A. Bernardi and N. Camaioni, *Energy Environ. Sci.*, 2011, **4**, 285.
23 S.-I. Na, S.-S. Kim, J. Jo and D.-Y. Kim, *Adv. Mater.*, 2008, **20**, 4061–4067, DOI: 10.1002/adma.200800338.
24 S. K. Hau, H.-L. Yip, J. Zou and A. K.-Y. Jen, *Org. Electron.*, 2009, **10**, 1401–1407, DOI: 10.1016/j.orgel.2009.06.019.
25 B. Winther-Jensen and F. C. Krebs, *Sol. Energy Mater. Sol. Cells*, 2006, **90**, 123–132, DOI: 10.1016/j.solmat.2005.02.004.
26 F. Guo, X. Zhu, K. Forberich, J. Krantz, T. Stubhan, M. Salinas, M. Halik, S. Spallek, B. Butz, E. Spiecker, T. Ameri, N. Li, P. Kubis, D. M. Guldi, G. J. Matt and C. J. Brabec, *Adv. Energy Mater.*, 2013, **3**, 1062–1067, DOI: 10.1002/aenm.201300100.
27 Y. Xia, K. Sun and J. Ouyang, *Energy Environ. Sci.*, 2012, **5**, 5325–5332.
28 W. Zhang, B. Zhao, Z. He, X. Zhao, H. Wang, S. Yang, H. Wu and Y. Cao, *Energy Environ. Sci.*, 2013, **6**, 1956–1964.
29 P. J. Brewer, J. Huang, P. Lane, A. J. deMello, D. D. C. Bradley and J. C. deMello, *Phys. Rev. B: Condens. Matter Mater. Phys.*, 2006, **74**, 115202, DOI: 10.1103/PhysRevB.74.125320.
30 C. Tengstedt, W. Osikowicz, W. R. Salaneck, I. D. Parker, C.-H. Hsu and M. Fahlman, *Appl. Phys. Lett.*, 2006, **88**, 053502, DOI: 10.1063/1.2168515.
31 B. Charlot, G. Sassine, A. Garraud, B. Sorli, A. Giani and P. Combette, *Microsyst. Technol.*, 2012, **19**, 895–903, DOI: 10.1007/s00542-012-1696-5.
32 T. Granlund, T. Nyberg, L. S. Roman, M. Svensson and O. Inganäs, *Adv. Mater.*, 2000, **12**, 269–273.
33 D. Li and L. J. Guo, *Appl. Phys. Lett.*, 2006, **88**, 063513, DOI: 10.1063/1.2168669.
34 S.-F. Tseng, W.-T. Hsiao, K.-C. Huang and D. Chiang, *Appl. Phys. A: Mater. Sci. Process.*, 2012, **112**, 41–47, DOI: 10.1007/s00339-012-7172-3.
35 F. C. Krebs, M. Jørgensen, K. Norrman, O. Hagemann, J. Alstrup, T. D. Nielsen, J. Fyenbo, K. Larsen and J. Kristensen, *Sol. Energy Mater. Sol. Cells*, 2009, **93**, 422–441, DOI: 10.1016/j.solmat.2008.12.001.
36 L. J. Guo, *J. Phys. D: Appl. Phys.*, 2004, **37**, 123–141, DOI: 10.1088/0022-3727/37/11/R01.
37 U. Lang, N. Naujoks and J. Dual, *Synth. Met.*, 2009, **159**, 473–479, DOI: 10.1016/j.synthmet.2008.11.005.
38 A. M. Nardes, M. Kemerink, M. M. de Kok, E. Vinken, K. Maturova and R. A. J. Janssen, *Organic Electronics*, 2008, **9**, 727–734, DOI: 10.1016/j.orgel.2008.05.006.
39 R. Meier, C. Birkenstock, C. Palumbiny and P. Müller-Buschbaum, *Phys. Chem. Chem. Phys.*, 2012, **14**, 15088–15098.
40 R. M. Reano, Y. P. Kong, H. Y. Low, L. Tan, F. Wang, S. W. Pang and A. F. Yee, *J. Vac. Sci. Technol., B: Microelectron. Nanometer Struct.–Process., Meas., Phenom.*, 2004, **22**, 3294–3299, DOI: 10.1116/1.1825013.
41 L. Tan, Y. P. Kong, S. W. Pang and A. F. Yee, *J. Vac. Sci. Technol., B: Microelectron. Nanometer Struct.–Process., Meas., Phenom.*, 2004, **22**, 2486–2492, DOI: 10.1116/1.1800353.
42 A. M. Nardes, M. Kemerink, R. A. J. Janssen, J. A. M. Bastiaansen, N. M. M. Kiggen, B. M. W. Langeveld, A. J. J. M. van Breemen and M. M. de Kok, *Adv. Mater.*, 2007, **19**, 1196–1200, DOI: 10.1002/adma.200602575.
43 X. Crispin, S. Marciniak, W. Osikowicz, G. Zotti, A. W. D. van der Gon, F. Louwet, M. Fahlman, L. Groenendaal, F. D. Schryver and W. R. Salaneck, *J. Polym. Sci., Part B: Polym. Phys.*, 2003, **41**, 2561–2583, DOI: 10.1002/polb.10659.
44 H. Hlaing, X. Lu, C.-Y. Nam and B. M. Ocko, *Small*, 2012, **8**, 3443–3447.
45 J. B. Emah, R. J. Curry and S. R. P. Silva, *Appl. Phys. Lett.*, 2008, **93**, 103301, DOI: 10.1063/1.2973342.
46 Y. Yang, K. Lee, K. Mielczarek, W. Hu and A. Zakhidov, *Nanotechnology*, 2011, **22**, 485301.
47 W. H. Kim, A. J. Mäkinen, N. Nikolov, R. Shashidhar, H. Kim and Z. H. Kafafi, *Appl. Phys. Lett.*, 2002, **80**, 3844–3846, DOI: 10.1063/1.1480100.
48 L. Pettersson, S. Ghosh and O. Inganäs, *Organic Electronics*, 2002, **3**, 143–148.
49 S. K. Jönsson, J. Birgerson, X. Crispin, G. Greczynski, W. Osikowicz, A. D. van der Gon, W. Salaneck and M. Fahlman, *Synth. Met.*, 2003, **139**, 1–10, DOI: 10.1016/s0379-6779(02)01259-6.
50 W. Zhang, B. Zhao, Z. He, X. Zhao, H. Wang, S. Yang, H. Wu and Y. Cao, *Energy Environ. Sci.*, 2013, **6**, 1956–1964.
51 T. Takano, H. Masunaga, A. Fujiwara, H. Okuzaki and T. Sasaki, *Macromolecules*, 2012, **45**, 3859–3865.
52 J. Y. Kim, J. H. Jung, D. E. Lee and J. Joo, *Synth. Met.*, 2002, **126**, 311–316.
53 A. Nardes, M. Kemerink and R. Janssen, *Phys. Rev. B: Condens. Matter Mater. Phys.*, 2007, **76**, 085208, DOI: 10.1103/physrevb.76.085208.
54 E. Vitoratos, S. Sakkapoulos, E. Dalas, N. Paliatsas, D. Karageirgopoulos, F. Petraki, S. Kennou and S. Choulis, *Organic Electronics*, 2009, **10**, 61–66, DOI: 10.1016/j.orgel.2008.10.008.
55 S. Timpanaro, M. Kemerink, F. J. Touwslager, M. M. D. Kok and S. Schrader, *Chem. Phys. Lett.*, 2004, **394**, 339–343, DOI: 10.1016/j.cplett.2004.07.035.
56 A. M. Nardes, R. A. J. Janssen and M. Kemerink, *Adv. Funct. Mater.*, 2008, **18**, 865–871, DOI: 10.1002/adfm.200700796.
57 J. Ouyang, Q. Xu, C.-W. Chu, Y. Yang, G. Li and J. Shinar, *Polymer*, 2004, **45**, 8443.
58 K. van de Ruit, R. I. Cohen, D. Bollen, T. van Mol, R. Yerushalmi-Rozen, R. A. J. Janssen and M. Kemerink, *Adv. Funct. Mater.*, 2013, **46**, 5778–5786, DOI: 10.1002/adfm.201301174.
59 Y. Xi and J. Ouyang, *J. Mater. Chem.*, 2011, **21**, 4927.
60 B. Friedel, P. E. Keivanidis, T. J. K. Brenner, A. Abrusci, C. R. McNeill, R. H. Friend and N. C. Greenham,

Macromolecules, 2009, **42**, 6741–6747, DOI: 10.1021/ma901182u.
61 T.-W. Lee and Y. Chung, *Adv. Funct. Mater.*, 2008, **18**, 2246–2252, DOI: 10.1002/adfm.200700766.
62 D.-J. Yun, H. Ra, J. Kim, I. Hwang, J. Lee, S.-W. Rhee and J. Chung, *ECS J. Solid State Sci. Technol.*, 2012, **1**, M10–M14, DOI: 10.1149/2.028201jss.
63 G. Greczynski, T. Kugler and W. Salaneck, *Thin Solid Films*, 1999, **354**, 129–135, DOI: 10.1016/s0040-6090(99)00422-8.
64 K. Z. Xing, M. Fahlman, X. W. Chen, O. Inganäs and W. R. Salanek, *Synth. Met.*, 1997, **89**, 161–165.
65 A. Gadisa, K. Tvingstedt, S. Admassie, L. Lindell, X. Crispin, M. R. Andersson, W. R. Salaneck and O. Inganäs, *Synth. Met.*, 2006, **156**, 1102–1107, DOI: 10.1016/j.synthmet.2006.07.006.
66 A. K. Pandey, J. M. Nunzi, B. Ratier and A. Moliton, *Phys. Lett. A*, 2008, **372**, 1333–1336, DOI: 10.1016/j.physleta.2007.09.068.
67 A. Ng, X. Liu, W. Y. Jim, A. B. Djurišić, K. C. Lo, S. Y. Li and W. K. Chan, *J. Appl. Polym. Sci.*, 2014, **131**, 39776.
68 H. Frohne, S. Shaheen, C. Brabec, D. Müller, N. Sariciftci and K. Meerholz, *ChemPhysChem*, 2002, **3**, 795–799.
69 G. Muller, N. Scherf, N. Brauchle and K. Meerholz, *Nature*, 2000, **405**, 661–665.

Supporting information for

Patterning PEDOT:PSS and Tailoring its Electronic Properties by Water-Vapour-Assisted Nanoimprint Lithography

Andrea Radivo[1,2], Enrico Sovernigo[1,3], Marco Caputo[4], Simone Dal Zilio[1], Tsegaye Endale[5], Alessandro Pozzato[3], Andrea Goldoni[4], Massimo Tormen[1,3,*]

[1] Istituto Officina dei Materiali-CNR, Laboratorio TASC, I-34149 Trieste, Italy

[2] University of Trieste, Piazzale Europa, 1, 34127 Trieste, Italia

[3] ThunderNIL srl, via Ugo Foscolo 8, 35131 Padova, Italy

[4] Sincrotrone Trieste SCpA, I-34149 Trieste, Italy

[5] Department of Chemistry, Addis Ababa University, P. O. Box: 1176, Addis Ababa, Ethiopia

Change of PEDOT to PSS ratio at the surface induced by WVA-NIL process.

XPS measure were performed to confirm the hypothesis that a change of the PEDOT to PSS ratio at the sample surface is induced WVA-NIL process. The result is plot in the image below:

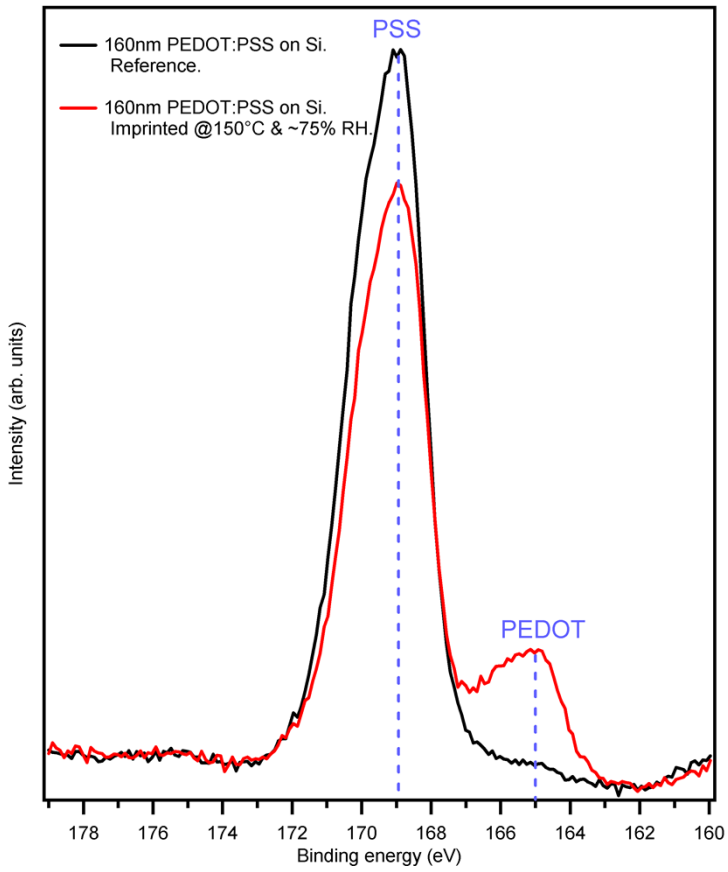

A reference flat untreated sample with 160nm PEDOT:PSS layer on Silicon substrate was compared to an identical film imprinted with a flat silicon mould at 150°C and ~75%RH. The sp2 peak of PSS's and PEDOT's sulfur are located respectively at 169 eV and 165 eV in binding energy. The ratio between the two peaks intensities is representative of the ratio between PEDOT and PSS.[1] A clear reduction of the PSS's peak intensity and an increase of PEDOT's peak intensity after the imprinting process was found, confirming an increase of PEDOT/PSS ratio on the surface. The acid PEDOT:PSS causes partial dissolution of ITO films, leading to the diffusion of In and Sn into PEDOT:PSS layer.[2] The diffused In interacts with S present in PEDOT:PSS,[3] making the measurements more difficult to understand. For this reason the experiment was performed using Si substrate.

1 T.-W. Lee, Y. Chung, *Advanced Functional Materials,* **2008**, *18, 2246–2252,* DOI 10.1002/adfm.200700766.

2 Anirudh Sharma, Scott E. Watkins, David A. Lewis, Gunther Andersson *Solar Energy Materials Solar Cells,* **2011**, 95, 3251–3255, DOI 10.1016/j.solmat.2011.07.012

3 Polona Škraba, Gvido Bratina, Satoru Igarashi, Hirosi Nohira, Kazuyuki Hirose, *Thin Solid Films*, **2011**, 519, 4216–4219

5

Unravelling the origin of the high excitonic diffusion length in $MAPbI_{3-x}Cl_x$ mixed perovskite

Organic-Inorganic Perovskites are firstly introduced by Kojima [9] in 2009 as alternative to molecular dyes in DSSC's. Their high quantum efficiency and low cost production make these materials an excellent candidate to be the next generation dyes for DSSC's, but unfortunately their low stability in electrolytic solutions seemed to stop their perspectives.

The key point for Organic-Inorganic perovskites is represented by the work of Kim et al.[10] published just two years ago, that showed how perovskites can be used also in a all-solid-state architecture, thanks to an solid state hole transport material (in their case Spiro-MeOTAD). The original work of Kim reported an efficiency of 9%, very close to the state-of-the-art organic and dye sensitized solar cells, and the exponential number of publications that followed this work showed how all the scientific community engaged in renewable energy harvesting has been excited by this exceptional value. Because of their nature, organic - inorganic perovskites catalysed the attention of groups of different extraction: people that previously worked in OPV, DSSC, but also semiconductor specialists previously engaged in thin film technology.

First studies has been concentrated on the architecture of the devices [40–43], but also on the dynamic of charge carriers by fast pump-probe and transient spectroscopies [11–13, 44–46]. In particular these last studies underlined a difference of one order of magnitude in the exciton diffusion length between the *classical* organic-inorganic pervoskite $CH_3NH_3PbI_3$, and its variant $CH_3NH_3PbI_{3-x}Cl_x$, where a small amount of chlorine used in the precursor reagents remains in the final perovskite. The reason why this two similar compounds show a so different behaviour is still unknown, and in this study we propose a possible explanation.

Thanks to X-ray diffraction we were able to show that the mixed $CH_3NH_3PbI_{3-x}Cl_x$ perovskite is a solid solution of $CH_3NH_3PbI_3$ and $CH_3NH_3PbCl_3$ perovskites, and thanks to photoemission spectroscopy we draw the scheme of the energetic levels of the two perovskites. From this we realized that holes can be tranferred from $CH_3NH_3PbI_3$ to $CH_3NH_3PbI_{3-x}Cl_x$, while the electrons can not follow the reverse path, realizing a charge separation interface able to enhance the charge carriers lifetime.

Unravelling the origin of the high excitonic diffusion length in $MAPbI_{3-x}Cl_x$ mixed perovskite

M. Caputo[1], F. Borghi[2], N. Cefarin[3,4], A. Radivo[1,3], N. Demitri[1], M. Panighel[1,4], G. Di Santo[1], S. Moretti[5], B. Policicchio[5], A. Giglia[3], M. Polentarutti[1], M. Tormen[3], P. Umari[3,6], and A. Goldoni[1]

[1]Elettra - Sincrotrone Trieste, s.s. 14 Km 163.5 in Area Science Park, Basovizza (Trieste) 34149, Italy
[2]Dipartimento di Fisica - Università di Modena e Reggio Emilia, via Campi 41125 Modena, Italy
[3]IOM-CNR Lab. TASC, s.s. 14 Km 163.5 in Area Science Park, Basovizza (Trieste) 34149, Italy
[4]Dipartimento di Fisica - Università di Trieste, via Valerio Trieste, Italy
[5]Dipartimento di Chimica - Università della Calabria, via Bucci 87036 Rende, Italy
[6]Dipartimento di Fisica e Astronomia - Università di Padova, via Marzolo 35131 Padova, Italy

Organic-Inorganic perovskite absorber is catalysing the attention of scientific community since their first usage. In particular the mixed phase $MAPbI_{3-x}Cl_x$ showed exceptional excitonic diffusion length, but the nature of these performances is still not understood. On the basis of X ray diffraction measures we can state that this mixed phase is actually a solid solution of $MAPbI_3$ and $MAPbCl_3$, and photoemission spectroscopy permitted us to draw the energy alignment diagram. This last revealed that the $MAPbI_3$/$MAPbCl_3$ interface act as a charge separator, actually breaking the excitons and enhancing the single lifetime charge carriers.

Introduction

The always-increasing world energy demand, along with the need of a more sustainable development, calls for alternative energy source. Solar energy is the most obvious solution since it is an abundant and freely available resource. Unfortunately today's photovoltaic landscape is dominated by semiconductor technology: its requirements of high purity materials and high temperature processes make its cost prohibitive if compared to hydrocarbon energy production. Since three decades new paradigms have been studied to substitute the semiconductor technology: Dye Sensitized Solar Cells (DSSCs) and Organic Photovoltaic (OPV) have been the most extensively studied and promising architecture, but their low efficiency has never increased to acceptable values.

In the attempt of boosting the efficiency of DSSCs, Miyasaka's group opened the doors of the organic/inorganic Methylammonium Lead Iodide ($MAPbI_3$) perovskite paradigm[1]: they used initially the perovskite as light absorber in electrochemical cell (Grätzel cells). Park's group moved forward the field going to an all-solid state architecture solving the problem of the dissolution of the perovskite in the electrolyte[2]. This represented the launching ramp for an exponential increase of the number of works on this system. Initially the perovskite absorber has been used as sensitizer for all-solid-state dye sensitized solar cells[3–6], but soon it has been clear that perovskite could act itself as charge transport medium thanks to its charge transport properties[3,5,7,8], opening the route to planar architecture devices[9–11].

Beside the benchmark $MAPbI_3$ several alterative organic/inorganic perovskites have been developed. First attempts of substituting the environmental problematic Lead with Tin have been performed[12], along with the substitution of metylammonium with formamidinium cation[13]. Also the halide part of the perovskite has been subjected to substitutions, resulting in a interesting tuning of the bandgap[6].

However, the most intriguing deviation from the initial $MAPbI_3$ is represented by the mixed phase $MAPbI_{3-x}Cl_x$: here a small part of the chlorine used in the precursor is supposed to remain in the final perovskite, even if it results very difficult to be observed. However the difference in the two phases is evident in terms of charge recombination rate, sensibly lower in the mixed phase[5,8,14]. Even if it is known that the nature of the mixed phase is a solid solution of $MAPbI_3$ and $MAPbCl_3$[15,16], it is still not clear the reason why it should show an excitonic diffusion length one order of magnitude higher than the benchmark $MAPbI_3$.

A recent study by Yamada et al.[17] suggests that the actual energy transport process has to be attributed to free charge carriers rather than to excitonic diffusion. Starting from this we will confirm by mean of X-Ray Diffraction (XRD), Photoemission Spectroscopy (PES), and GW band structure calculations, that the mixed phase $MAPbI_{3-x}Cl_x$ is a solution of $MAPbI_3$ and $MAPbCl_3$, and we will show that their energy levels makes possible a fast excitonic separation inside the absorber layer, enhancing the single carrier lifetime.

Experimental methods

Two different mixed halide perovskite samples have been compared with the benchmarks $MAPbI_3$, $MAPbCl_3$, PbI_2, $PbCl_2$.

Lead halide samples have been evaporated in high vacuum ($P<10^{-8}$ mbar) on a polycrystalline gold sample for photoemission experiments, while the diffraction measures have been performed in powder crystalized on a nylon loop.

$MAPbI_3$ sample has been prepared by spincoating. Pure iodine perovskite solution (CH_3NH_3I and PbI_2 1:1 in DMF) was spin coated on silicon <100> wafers (20x 20 mm^2) (2000 rpm for 60") and the substrates were placed on a hot plate for 5' at 85°C to achieve the evaporation of the solvent and the crystallization of the hybrid organic-inorganic material

$MAPbCl_3$ sample for photoemission experiment has been prepared with the two-step method: we evaporated $PbCl_2$ on a polycrystalline gold substrate and dropcasted on the obtained film a saturated methylammonium chloride (MACl) solution in ethanol. Diffraction measures have been performed crystalizing a solution of MACl and $PbCl_2$ 1:1 in DMSO on a nylon loop.

The first mixed halide phase (**M1**) has been obtained evaporating PbI_2 on polycrystalline gold (photoemission experiment) or silicon on a kapton tape (diffraction experiment) and dropcasting a solution of MACl and PbI_2 1:1 5% in weight in DMF.

The second mixed halide phase (**M2**) has been prepared evaporating PbI_2 on polycrystalline gold and dropcasting a saturated solution of MACl in ethanhol.

Photoemission experiment has been performed in a modified VG Escalab MKII (secondary cut-off and valence band spectra at 21.22 eV) and on BEAR beamline at ELETTRA. The overall resolution is 200 meV for valence band spectra and 800 meV for core level spectra. When not stated otherwise all the binding energy are referred to the Fermi level. Binding energy calibration has been performed using the Au $4f_{7/2}$ peaks (for core levels) and the Fermi level (for valence bands) of a gold foil put in the proximity of the sample. The binding energy of core levels has further refined using the elemental $Pb4f_{7/2}$ component present in all the spectra.

Diffraction experiments have been performed on XRD1 beamline at ELETTRA. Powder diffraction patterns have been collected in transmission mode at a monochromatic wavelength of 0.7 Å for samples grown on thick substrates, or 1/1.5 Å for samples mounted on nylon loop. Data have been collected at room temperature (25°C) otherwise specified. Standard experimental calibration has been followed using a 0.3 mm borosilicate capillary filled with NIST LaB_6 660a standard powder (SRM660), to define the beam centre, adjust detector distance and tilting. Monochromator energy has been calibrated

using a fluorescence scan at selenium absorption edge. Calculated profiles have been obtained from single crystal structures found on AMCSD database.

Calculations were performed within the Density Functional Theory (DFT) within the “screened” version of Hartree-Fock frameworks (GW approximation) using the Quantum-Espresso package[18]. The exchange and correlation functionals in the DFT method were obtained in the generalized gradient approximations (GGA) described in ref. 19 (hereinafter referred to as PBE). These GGA functionals were also used to calculate the structural configurations of the several solids utilized after the creation of the valence band hole in photoemission experiments. Therefore, we have calculated the valence electronic density of states (DOS) directly from the PBE eigenenergies and through the many-body method based on the GW approximation[20,21].

Results and discussion

Figure 1 shows the diffraction pattern of all the investigated samples. Panels a) and b) show the diffraction pattern of $MAPbI_3$ and $MAPbCl_3$ samples, along with the diffraction patterns of respectively PbI_2, MAI, $PbCl_2$, and MACl. Upon formation of $MAPbI_3$ perovskite by spincoating process no traces of residual of PbI_2 or MAI can be detected, while panel b) shows that residual of MACl are present (peaks at 17.5, 22.9, 27.2, 29.5 degrees) when the solvent evaporation is not accompanied by any other process.

Panel c) of Figure 1 shows the diffraction pattern of M1 sample. Almost all the peaks come from the two perovskites, along with a certain amount of unreacted PbI_2 and MACl. In particular the inset shows the region 11.5 - 16.5 degrees once the background coming from the kapton tape has ben removed: here we can easily distinguish the contribution coming from PbI_2 (12.7°), $MAPbI_3$ (14.1°), and $MAPbCl_3$ (15.6°).

Finally, panel d) of Figure 1 shows the diffraction pattern of M2 sample. Also here we can distinguish the contribution coming from the different reagents along with the main contribution coming from $MAPbCl_3$ and a small amount of $MAPbI_3$. Peaks at 25° and 30.5° can be attributed to a $PbCl_2$ phase, while probably the peak at 16.6° comes from a $PbCl_4$ phase.

These data confirms the coexistence of both $MAPbI_3$ and $MAPbCl_3$ perovskites in a single sample. To understand the effect of the interface formation we performed photoemission measure.

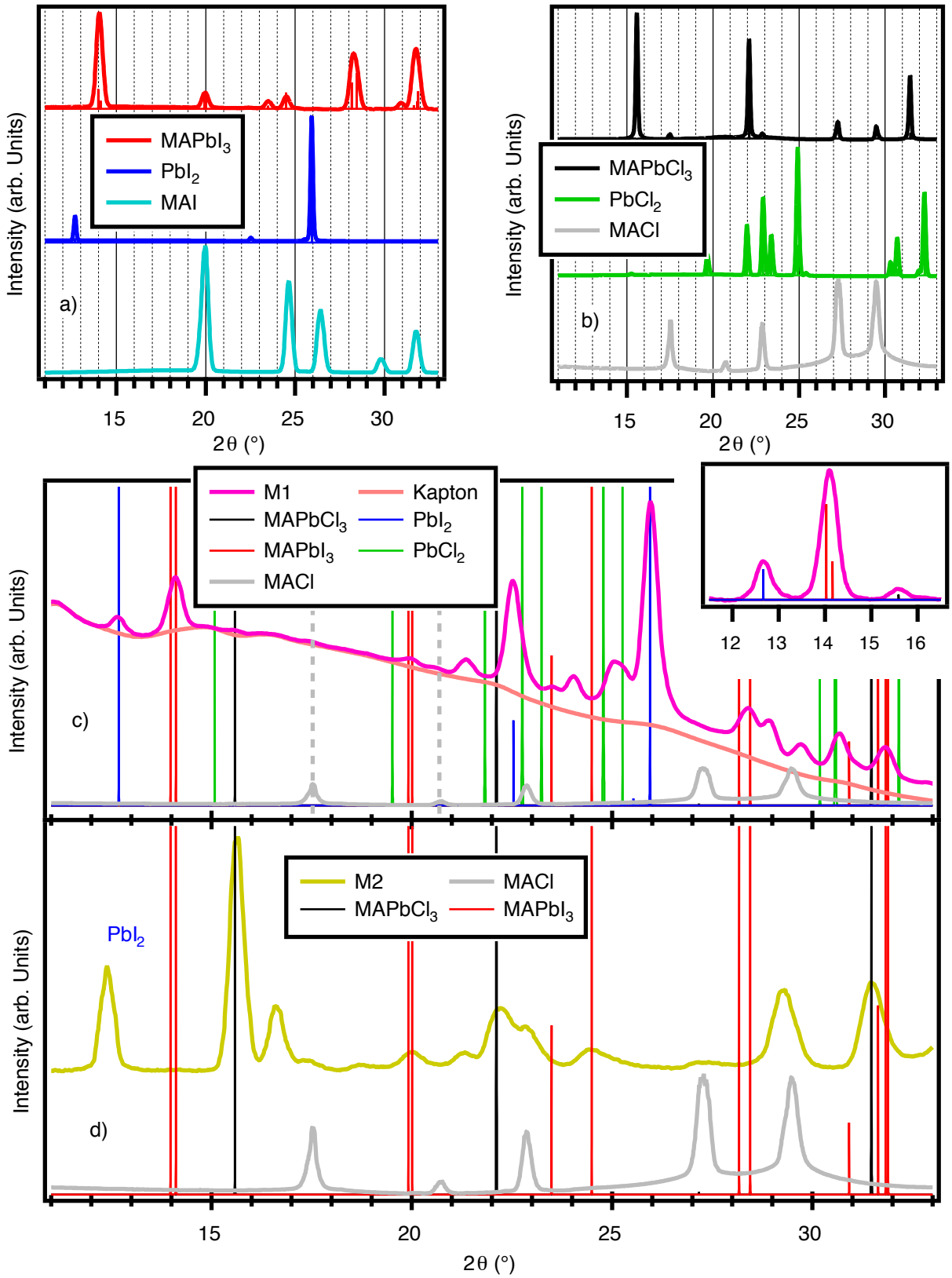

Figure 1: Diffraction patterns for $MAPbI_3$ (red), PbI_2 (blue), and MAI (cyan) in panel a. Diffraction patterns for $MAPbCl_3$ (black), $PbCl_2$ (green), and MACl (grey) in panel b). Diffraction patterns for M1 (purple), MACl (gray), and for the kapton used to hold the sample (pink) in panel c). Diffraction patterns for M2 (yellow) and MACl (grey) in panel d). Vertical bars in all panels indicate the position of $MAPbI_3$ (red), $MAPbCl_3$ (black), and PbI_2 (blue) peaks according to calculations.

Figure 2c shows the Pb 4f photoemission peaks of our reference compounds $MAPbCl_3$, $MAPbI_3$, $PbCl_2$, and PbI_2. All these spectra show a low energy component at 136.69 eV: it corresponds to elemental Pb. We can note that the energy of the two lead salt peaks is remarkably different (1.5 eV) even if they are very similar compounds with same lead oxidation state. The electron affinity of chlorine is in fact higher than the iodine one, causing a different degree of charge transfer form lead atoms. In particular increasing the electron affinity of the halide corresponds to an increase of the binding energy of the lead peaks.

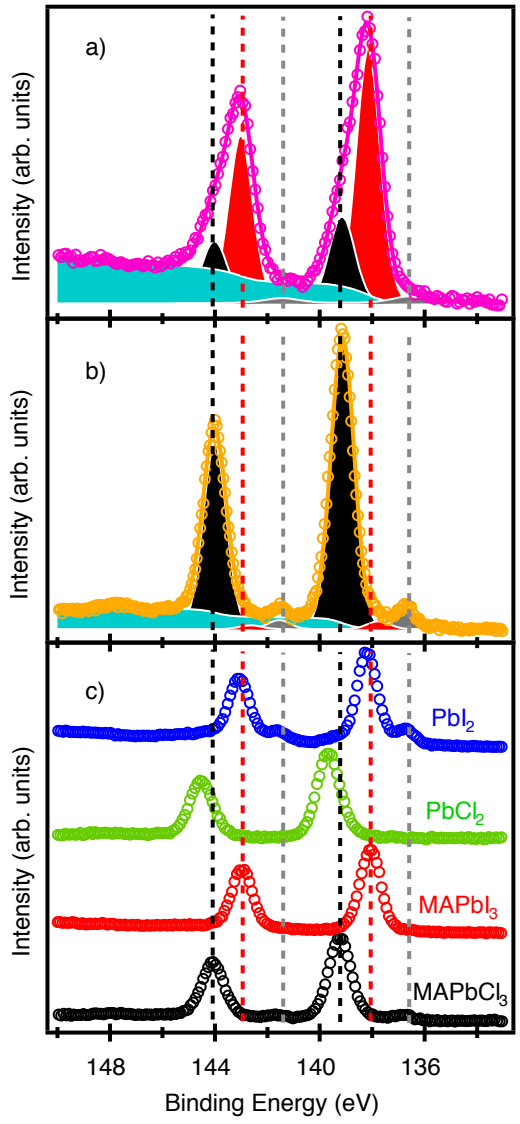

Figure 2: Pb 4f core level spectra of sample M1 (panel a), M2 (b), and the benchmarks $MAPbCl_3$ (black circles, panel c), $MAPbI_3$ (red circles, c), $PbCl_2$ (green circles, c), PbI_2 (blue circles, c) acquired with a photon energy of 280 eV. The fit result is also reported for M1 and M2 samples: gray peaks correspond to elemental Pb, red peaks to $MAPbI_3$, and black peaks to $MAPbCl_3$. Vertical bars represent the energy of the benchmarks peaks.

Upon perovskite formation we can see that both $MAPbCl_3$ and $MaPbI_3$ show a Pb 4f lower binding energy than their respective salts, suggesting an effective stabilization effect of the methylammonium ion, even more pronounced in the $MAPbCl_3$ case.

Sample M1 shows much more broad and asymmetric peaks, indicating the presence of different and well separated components. We fitted its peaks with three voight components and a Shirley background: the first component has been held at 136.69 eV to take in account for the elemental component, the other two left free to move. The fit result is reported in table 1: the energy of the two free components show a excellent similarity with the energy of the $MAPbCl_3$ and $MAPbI_3$ perovskites, supporting the idea of the coexistence of the two phases in what is called mixed halide perovskite. From this analysis M1 sample results to be formed by 30% $MAPbCl_3$ and 70% $MaPbI_3$. A similar analysis has been performed for sample M2, with similar results for what concern the binding energies (see table 1). The calculated stoichiometry is 95% $MAPbCl_3$ and 5% $MaPbI_3$.

It is worth noting that the results we obtained are not competitive with the recent results obtained by Colella et al.[22], where a wetting layer of chlorine between the TiO_2 compact layer and

	Lower energy component ($MaPbI_3$)	Higher energy component ($MAPbCl_3$)
$MaPbI_3$	138.08 ± 0.20 eV	-
$MAPbCl_3$	-	139.05 ± 0.07 eV
M1	138.25 ± 0.23 eV	139.05 ± 0.23 eV
M2	137.77 ± 0.22 eV	139.13 ± 0.07 eV

Table 1: Pb $4f_{7/2}$ binding energy for $MAPbCl_3$ and $MaPbI_3$, and fit result for M1 and M2 sample.

the $MAPbI_3$ has been found. Their extremely thin sample shows that the $MAPbI_3$/chlorine/TiO_2 interface is energetically favoured with respect to the bare $MAPbI_3$/TiO_2 interface, however they did not investigate a bulky sample. Our results indicate that the coexistence of $MAPbI_3$ and $MAPbCl_3$ in an optically thick sample is possible.

Figure 3 shows the valence band spectra of sample M1 (panel a) and M2 (b), along with valence band spectra of $MAPbI_3$ (c) and $MAPbCl_3$ (d) phases.

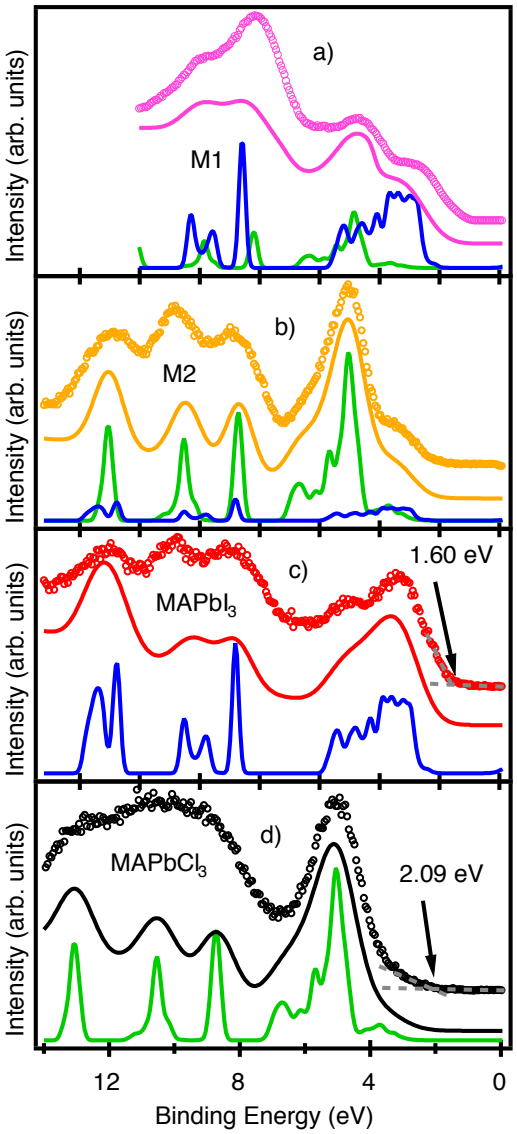

Figure 3: Valence band spectra of M1 (panel a), M2 (b), $MAPbI_3$ (c), and $MAPbCl_3$ (d). For each panel the bottom continuous line is the GW calculated spectrum, while the top continuous line is the same spectrum convoluted with a gaussian function to take in account the finite experimental resolution. Circles represent the experimental points. Valence bands in panel a is acquired with photon energy of 21.22 eV, all the others valence bands are acquired with photon energy of 55 eV. Arrows indicate the valence band onset, whose energy value is reported in the same graph.

The agreement between the band structure calculations for $MAPbCl_3$ and $MAPbI_3$ and the respective experimental spectra is extremely good in the region 0-7 eV, while at higher binding energy the electronic states are broadened due to the superposition with the states of the unreacted MACl and MAI present on the surface.

From panel a and b we can see that the valence band of the two mixed halide samples can be easily obtained as the superposition of the calculated electronic structure of $MAPbI_3$ (blue line) and $MAPbCl_3$ (green line) perovsiktes, varying their relative ratio. In particular M1 is composed by 70% of $MAPbCl_3$ and 30% of $MaPbI_3$, while 85% of $MAPbCl_3$ and 15% of $MaPbI_3$ compose M2. Both the results are in fair accordance with the stoichiometry calculated from core level spectra.

Binding energies of calculated spectra in figure 3 are calibrated on the experimental spectra of $MAPbCl_3$ and $MaPbI_3$, and kept fixed for the mixed phases (figure 3a and 3b). However from figure 3a seems that the first electronic states of M1 sample is shifted towards lower binding energy with respect to the calculated one. Since in the region 0-4 eV the electronic structure is dominated by the $MaPbI_3$ part, in figure 4 we compared the experimental spectrum of sample M1 with a superposition of calculated spectra of $MAPbCl_3$ and $MaPbI_3$, where the last has been shifted of 0.5 eV towards lower binding energy. In this case a better accordance between experimental data and calculated spectrum is

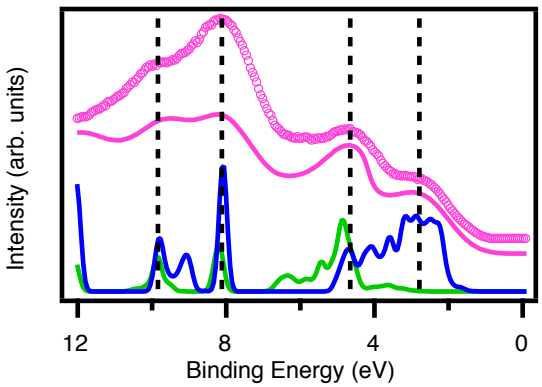

Figure 4: Valence Band of M1 sample (purple circles) compared with calculations (purple continuous line). In this case the $MaPbI_3$ calculation is shifted 0.5 eV toward lower binding energy in comparison with the calculations in figure 3.

evident. It has been suggested that residual clusters of metallic lead can cause a n-doping of $MAPbI_3$ perovskite[9], evident from the fact that the onset of the valence band correspond roughly to bandgap (1.6 eV vs 1.61 eV respectively). In the case of M1 sample the formation of $PbCl_2$, evident from diffraction patterns, can neutralize the doping effect of lead clusters, probably encapsulating the residual metallic lead.

Once understood the concomitance of the two halide phases in a thick sample we investigated their band alignment. In figure 3a and 3b arrows indicate the valence band onset for $MAPbCl_3$ and $MaPbI_3$. This information can be joined with the work function values calculated from the secondary electron cut-off reported in figure 5b, and with the bandgap reported in the literature, to obtain the band alignment. Figure 5c reports a scheme of the valence band alignment: the band onset of $MAPbCl_3$ is slightly higher with respect to the band onset of $MAPbI_3$, allowing the photoexcited holes in the last to be transferred in the chlorine perovskite. At the same time the higher bandgap in $MAPbCl_3$ ensures that no electrons can be transferred with the holes, realizing an effective charge separation interface. Once holes are trapped in the $MAPbCl_3$ part, photoexcited electrons lose their main decay channel i.e. the electron-hole recombination, resulting in the strong enhancement of the photoluminescence lifetime observed in the mixed halide $MAPbI_{3-x}Cl_x$[8].

Conclusions

In this paper we investigated the structure of the mixed phase $MAPbI_{3-x}Cl_x$ by mean of X ray diffraction, and its electronic structure by mean of photoemission spectroscopies, to understand why this phase shows an enhancement of the excitonic lifetime.

We confirmed the coexistence of both $MAPbCl_3$ and $MaPbI_3$ in the mixed phase, and we showed that their energetic levels alignment provide a good charge separation interface. Once electrons and holes are spatially separated in the two different parts of the sample, their recombination is forbidden, justifying the enhanced photoluminescence lifetime. This finding can help the development of higher efficiency devices. Controlling the relative $MAPbCl_3/MaPbI_3$ ratio, and their morphology inside the device can result in extremely efficient charge separation interfaces.

Moreover we showed that the $MaPbI_3$ doping level can be modified using small amounts of $MAPbCl_3$, opening the route to new a new parameter that can be used to enhance the final device efficiency.

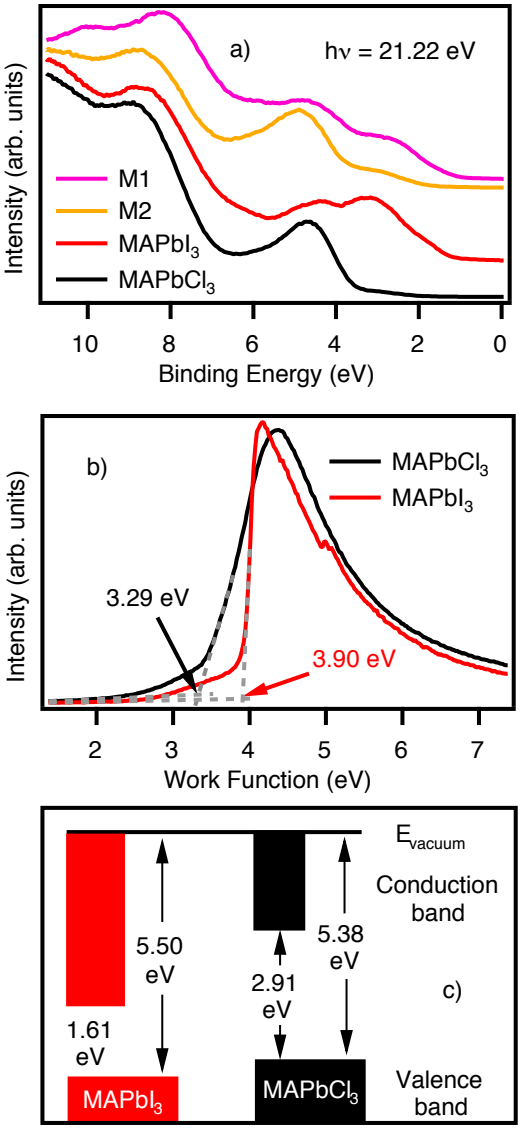

Figure 5: Valence band spectra acquired with photon energy of 21.22 eV, corresponding to the HeI excitation line of the discharge lamp (panel a). Secondary electron cut-off for $MaPbI_3$ and $MAPbCl_3$ (b) and band alignment scheme of the two perovskites (c). It is worth noting that the work function values in the x axis of panel b are referred to the Fermi level of the systems, while the energetic levels in panel c are referred to the vacuum level.

References

(1) Kojima, A.; Teshima, K.; Shirai, Y.; Miyasaka, T. Organometal Halide Perovskites as Visible-Light Sensitizers for Photovoltaic Cells. *J. Am. Chem. Soc.* **2009**, *131*, 6050–6051.

(2) Kim, H.-S.; Lee, C.-R.; Im, J.-H.; Lee, K.-B.; Moehl, T.; Marchioro, A.; Moon, S.-J.; Humphry-Baker, R.; Yum, J.-H.; Moser, J. E.; et al. Lead Iodide Perovskite Sensitized All-Solid-State Submicron Thin Film Mesoscopic Solar Cell with Efficiency Exceeding 9%. *Sci. Rep.* **2012**, *2*, 591.

(3) Lee, M. M.; Teuscher, J.; Miyasaka, T.; Murakami, T. N.; Snaith, H. J. Efficient Hybrid Solar Cells Based on Meso-Superstructured Organometal Halide Perovskites. *Science* **2012**, *338*, 643–647.

(4) Burschka, J.; Pellet, N.; Moon, S.-J.; Humphry-Baker, R.; Gao, P.; Nazeeruddin, M. K.; Grätzel, M. Sequential Deposition as a Route to High-Performance Perovskite-Sensitized Solar Cells. *Nature* **2013**, *499*, 316–319.

(5) Wehrenfennig, C.; Eperon, G. E.; Johnston, M. B.; Snaith, H. J.; Herz, L. M. High Charge Carrier Mobilities and Lifetimes in Organolead Trihalide Perovskites. *Adv. Mater.* **2014**, *26*, 1584–1589.

(6) Noh, J.; Im, S.; Heo, J.; Mandal, T.; Seok, S. Chemical Management for Colorful, Efficient, and Stable Inorganic–Organic Hybrid Nanostructured Solar Cells. *Nano Lett.* **2013**.

(7) Xing, G.; Mathews, N.; Sun, S.; Lim, S. S.; Lam, Y. M.; Grätzel, M.; Mhaisalkar, S. G.; Sum, T. C. Long-Range Balanced Electron- and Hole-Transport Lengths in Organic-Inorganic CH3NH3PbI3. *Science* **2013**, *342*, 344–347.

(8) Stranks, S. D.; Eperon, G. E.; Grancini, G.; Menelaou, C.; Alcocer, M. J. P.; Leijtens, T.; Herz, L. M.; Petrozza, A.; Snaith, H. J. Electron-Hole Diffusion Lengths Exceeding 1 Micrometer in an Organometal Trihalide Perovskite Absorber. *Science* **2013**, *342*, 341–344.

(9) Conings, B.; Baeten, L.; De Dobbelaere, C.; D'Haen, J.; Manca, J.; Boyen, H.-G. Perovskite-Based Hybrid Solar Cells Exceeding 10% Efficiency with High Reproducibility Using a Thin Film Sandwich Approach. *Adv. Mater.* **2013**, 1–6.

(10) Liu, M.; Johnston, M. B.; Snaith, H. J. Efficient Planar Heterojunction Perovskite Solar Cells by Vapour Deposition. *Nature* **2013**, *501*, 395–398.

(11) Malinkiewicz, O.; Yella, A.; Lee, Y. H.; Espallargas, G. M.; Grätzel, M.; Nazeeruddin, M. K.; Bolink, H. J. Perovskite Solar Cells Employing Organic Charge-Transport Layers. *Nat. Photonics* **2013**, 1–5.

(12) Hao, F.; Stoumpos, C. C.; Cao, D. H.; Chang, R. P. H.; Kanatzidis, M. G. Lead-Free Solid-State Organic–inorganic Halide Perovskite Solar Cells. *Nat. Photonics* **2014**, *8*, 489–494.

(13) Pang, S.; Hu, H.; Zhang, J.; Lv, S.; Yu, Y.; Wei, F.; Qin, T.; Xu, H.; Liu, Z.; Cui, G. NH2CH═NH2PbI3: An Alternative Organolead Iodide Perovskite Sensitizer for Mesoscopic Solar Cells. *Chem. Mater.* **2014**, *26*, 1485–1491.

(14) Suarez, B.; Gonzalez-Pedro, V.; Ripolles, T. S.; Sanchez, R. S.; Otero, L.; Mora-Sero, I. Recombination Study of Combined Halides (Cl, Br, I) Perovskite Solar Cells. *J. Phys. Chem. Lett.* **2014**, *5*, 1628–1635.

(15) Colella, S.; Mosconi, E.; Fedeli, P.; Listorti, A.; Gazza, F.; Orlandi, F.; Ferro, P.; Besagni, T.; Rizzo, A.; Calestani, G.; et al. MAPbI3-xClx Mixed Halide Perovskite for Hybrid Solar Cells: The Role of Chloride as Dopant on the Transport and Structural Properties. *Chem. Mater.* **2013**, *25*, 4613–4618.

(16) Grätzel, M. The Light and Shade of Perovskite Solar Cells. *Nat. Mater.* **2014**, *13*, 838–842.

(17) Yamada, Y.; Nakamura, T.; Endo, M.; Wakamiya, A.; Kanemitsu, Y. Photocarrier Recombination Dynamics in Perovskite CH3NH3PbI3 for Solar Cell Applications. *J. Am. Chem. Soc.* **2014**, *136*.

(18) Giannozzi, P.; Baroni, S.; Bonini, N.; Calandra, M.; Car, R.; Cavazzoni, C.; Ceresoli, D.; Chiarotti, G. L.; Cococcioni, M.; Dabo, I.; et al. QUANTUM ESPRESSO: A Modular and Open-Source Software Project for Quantum Simulations of Materials. *J. Phys. Condens. Matter* **2009**, *21*, 395502.

(19) Perdew, J.; Burke, K.; Ernzerhof, M. Generalized Gradient Approximation Made Simple. *Phys. Rev. Lett.* **1996**, *77*, 3865–3868.

(20) Hybertsen, M. S.; Louie, S. G. Electron Correlation in Semiconductors and Insulators: Band Gaps and Quasiparticle Energies. *Phys. Rev. B* **1986**, *34*, 5390–5413.

(21) Godby, R. W.; Schlüter, M.; Sham, L. J. Self-Energy Operators and Exchange-Correlation Potentials in Semiconductors. *Phys. Rev. B* **1988**, *37*, 10159–10175.

(22) Colella, S.; Mosconi, E.; Pellegrino, G.; Alberti, A.; Guerra, V. L. P.; Masi, S.; Listorti, A.; Rizzo, A.; Condorelli, G. G.; De

Angelis, F.; et al. Elusive Presence of Chloride in Mixed Halide Perovskite Solar Cells. *J. Phys. Chem. Lett.* **2014**, *5*, 3532–3538.

6

Fabrication and electrochemical characterization of amorphous lithium iron silicate thin films as positive electrodes for lithium batteries

Better batteries today means safer and higher capacity batteries. Today's electrolyte are composed by lithium salts in an organic solvent, very likely to flame if they go in contact with the air. Another safety issue comes from the cobalt present in most of the cathode, in fact $LiCoO_2$ is a a potential human carcinogen. In addition cobalt is the rarest first row transition metal, making its substitution also economically desirable.

Design new cathodes can give a triple advantage:

1. Substitute the expensive and unsafe $LiCoO_2$
2. Increase the lithium intercalation possibility, and so the battery capacity
3. Having a better interface with the new solid electrolyte

The most promising class of material is the orthosilicate compounds with formula Li_2MSiO_4, with M = Fe or Mn [47]. The key feature of these compounds is the possibility to intercalate two lithium ions per unit cell, overcoming the today's limitation in energy density.

In this paper we reported fabrication and characterization of $Li_2Fe_{0.5}Mn_{0.5}SiO_4$ and Li_2FeSiO_4 amorphous thin film cathodes especially designed for microbatteries. Electrochemical characterization confirmed performances comparable with bulk-crystalline samples, while XPS characterization enlightened a non-optimal stoichiometry and chemistry of the film. Optimization of the deposition parameters is mandatory for a correct film fabrication, that will lead hopefully to even better performances.

Journal of Power Sources 266 (2014) 179–185

Contents lists available at ScienceDirect

Journal of Power Sources

journal homepage: www.elsevier.com/locate/jpowsour

Fabrication and electrochemical characterization of amorphous lithium iron silicate thin films as positive electrodes for lithium batteries

I. Quinzeni [a], S. Ferrari [a,*], E. Quartarone [a], D. Capsoni [a], M. Caputo [b], A. Goldoni [b], P. Mustarelli [a], M. Bini [a]

[a] Dept. of Chemistry, University of Pavia, Viale Taramelli 16, 27100 Pavia, Italy
[b] Elettra Sincrotrone Trieste, Strada Statale 14, Km 163.5, I-34149 Trieste, Italy

HIGHLIGHTS

- Thin film deposition of amorphous Li/M(Fe,Mn)/Si/O by r.f. sputtering.
- Good electrochemical performances: 50 mAh g^{-1} at 2.5 C.
- The films were able to sustain about 300 cycles of charge–discharge.

GRAPHICAL ABSTRACT

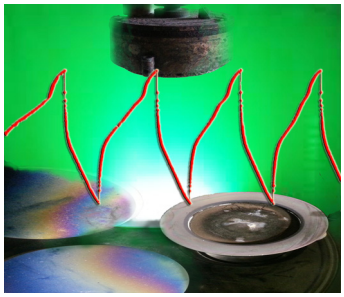

ARTICLE INFO

Article history:
Received 22 January 2014
Received in revised form
25 April 2014
Accepted 3 May 2014
Available online 13 May 2014

Keywords:
Lithium microbattery
Thin film
r.f. sputtering
Li_2FeSiO_4
XPS
Cyclic voltammetry

ABSTRACT

In this work we reported, for the first time, the preparation by radio frequency sputtering and the electrochemical characterization of Li/M/Si/O thin films (M = Fe, Mn), as positive electrodes for lithium microbatteries. The deposited films were amorphous both in case of pure iron and mixed iron/manganese compositions. The electrochemical performances, in terms of capacity values and coulombic efficiency, were comparable to those currently reported for the corresponding crystalline bulk materials. In particular, capacities of the order of 50 mAh g^{-1} were obtained at 2.5 C with coulombic efficiency near 90% by using a standard liquid electrolyte. Our preliminary electrochemical results, together with the easiness of preparation, suggested that Li/M/Si/O thin films could be interesting candidates as cathodes in lithium microbatteries.

1. Introduction

The development of thin-film lithium batteries as power sources for new generation micro-devices was rapidly growing over these last years. Such microsystems show several advantages, e.g. lightness, low cost and easy integration in micro-devices owing to their miniaturization [1,2]. A wide area of applications may be foreseen, ranging from microelectronics to sensors in medical and

* Corresponding author. Dipartimento di Chimica, Sezione di Chimica Fisica, Università di Pavia, Viale Taramelli 16, 27100 Pavia, Italy. Tel.: +39 382 987213; fax: +39 382 987575.
E-mail addresses: stefania.ferrari@unipv.it, S.Ferrari@warwick.ac.uk (S. Ferrari).

http://dx.doi.org/10.1016/j.jpowsour.2014.05.012
0378-7753/

military fields, smart cards and other micro-devices (MEMS, NEMS), and also Radio Frequency Identification (RFID) tags, and this represents a very topical target. Large-scale applications in the next future are chiefly expected for food and drug control. During the last years, many efforts on the optimization of lithium microbatteries were discussed in the literature, regarding both flat [Ref. [3] and references therein] and 3D configurations [4].

Many materials were suggested in the past as microbattery components, such as V_2O_5 [5], $LiCoO_2$ [6,7] or $LiMn_2O_4$ [8,9] as high voltage cathodes, lithium oxide or sulphide compounds (crystals and glasses) as solid electrolytes [10], and Li metal or vanadates [11] as the anodes. The use of thin film electrodes to shorten diffusion paths of Li ions seems to be an effective solution to enhance the rate capability of a battery, but the energy density still remains a challenge. A recently proposed solution encompassing both high energy and high power densities is the development of three-dimensional (3D) nanostructured architectures and design with large surface area [12–14]. However, there are still two major obstacles for wider applications of the 3D electrodes. The first one is the complex and high-cost fabrication process, that limits the large-scale production. The other is that the energy density of the whole device is still low, due to the extremely thin active material layer as compared with the much thicker substrate.

Moreover, increasingly important safety and toxicity issues should be considered, which are chiefly relevant in case of $LiCoO_2$ and $LiMn_2O_4$, the most used compounds for thin film cathode preparation. Therefore, more environmentally friendly compounds are required for these applications. In this frame, $LiFePO_4$ belonging to the family of polyanion compounds is important because, among other fundamental properties such as the good cycling stability, it is highly safe and non-toxic. Thin films of $LiFePO_4$ have been prepared by different deposition techniques such as r.f. sputtering [15], electrophoretic deposition [16] and pulsed laser deposition [17], and the effects of deposition temperature and kind of substrate on the crystal structure and morphology of the resulting thin films have been already addressed.

Recently, low toxic, low cost and highly available cathode materials belonging to the orthosilicate family with formula Li_2MSiO_4 (M = Fe, Mn) were proposed as bulk materials [18–20]. Several works were devoted to their structural and computational characterization [21–24], as well as to the optimization of their electrochemical performances [25]. The importance of these compounds chiefly resides in their high theoretical capacity (up to 330 mAh g^{-1} for two lithium ions insertion/extraction) that justifies the efforts devoted to the preparation of new architectures such as nano- and mesoporous forms [26–28]. In case of standard Li-ion cells, orthosilicates (e.g. Li_2MnSiO_4) are generally prepared and used in crystalline form, but they can undergo amorphization on repeated cycling [29]. This crystalline-to-amorphous transition, in turn, leads to a progressive worsening of the electrochemical performances. So far, the preparation of orthosilicate thin films was never reported, likely due to the difficulty to deposit with the right stoichiometry a ternary oxide, differently from binary compounds such as vanadium [30], titanium [31] and iron oxides [32].

In this work, for the first time to our knowledge, we reported the radiofrequency (r.f.) magnetron sputtering preparation and the physico-chemical characterization of Li/M/Si/O (M = Fe, Mn) amorphous films with nominal composition $Li_2Fe_{1-x}Mn_xSiO_4$ (x = 0, 0.5). The structural and microstructural properties of the thin films were investigated by means of XRD, SEM and XPS techniques. The electrochemical properties were addressed by performing cyclic voltammetry and preliminary battery tests on a lithium cell with a standard liquid electrolyte.

2. Experimental

2.1. Synthesis

Thin films with nominal composition $Li_2Fe_{1-x}Mn_xSiO_4$ ($x = 0, 0.5$) were deposited in a high vacuum (10^{-3} Pa) r.f. magnetron sputtering system, which consists of three confocal cathodes at 40–50 mm from the substrate center. As the deposition substrates, we used stainless steel (s.s.) disks with a diameter of 10 mm (Good Fellow, SS-AISI304 Fe/Cr18/Ni10 annealed), previously coated by a 150 nm-thick layer of gold as current collector. $Li_2Mn_{0.5}Fe_{0.5}SiO_4$ and Li_2FeSiO_4 powders, prepared by sol–gel synthesis [20,21], were used as the target. The depositions were performed by a procedure made of two consecutive steps without sample extraction: 1) at 60 W for 1 h; 2) at 100 W for 2 h. The pressure was kept at $3\cdot10^{-2}$ mbar, with a substrate temperature of 700 °C and 20 sccm of Ar flow. At the end of the deposition, the samples were kept at the same temperature (700 °C) for additional 1 h inside the r.f. sputtering chamber, and then cooled down to ambient temperature under vacuum. The thickness of both the films was about 390 nm, as determined by profilometry. The samples were named FeMn or Fe for the mixed or iron silicate, respectively.

2.2. Characterization techniques

X-ray diffraction (XRD) measurements were performed using a Bruker D5005 diffractometer with the CuKα radiation, a graphite monochromator and a scintillation detector. The patterns were collected with a step size of 0.02° and counting time of 6 s per step in the angular range 15–65°/2θ.

Scanning Electron Microscopy (SEM) measurements were performed with a Zeiss EVO®-MA10-HR microscope.

The film thickness was measured by means of a stylus profilometer (KLA Tencor P6 Profiler), by applying a force of 20 μN. The active mass of the silicate thin films (about 30 μg i.e. 60 μg/cm^2) was measured by using an ultra sensitive microbalance (HIDEN ISOCHEMA IGA-001).

X-ray Photoelectron Spectroscopy (XPS) spectra were acquired on a sample deposited in the same way as FeMn on Ni substrate, in order to avoid the signal of Fe coming from stainless steel. XPS spectra were acquired *ex situ* by inserting the sample in a modified VG ESCALAB MkII system, with a base pressure of 10^{-10} mbar, equipped with a non-monochromatic Al Kα X-ray source. The photoelectrons were collected with an hemispherical energy analyzer working at pass energy 10 eV with an energy resolution of 0.9 eV. Sample surface was not treated in any way before the measurements. Si2p has been taken as energy reference in its silicate form (102 eV) [33], after this the binding energy of all the other peaks has been checked and was considered consistent.

The electrochemical tests were performed using a three-electrodes T-cell with lithium metal as the negative and the counter electrodes and a glass-wool (Whatman GF/A) disc as the separator. The electrolyte was 1 M $LiPF_6$ in ethylene carbonate/diethyl carbonate (EC/DEC) 1:1 (Merck). All the cells were assembled in a dry-box under Argon atmosphere. Cyclic voltammetry (CV) was performed by using an Autolab PGSTAT30 (Eco Chemie) at a scan rate of 0.2 mV s^{-1} in the potential range 2.5–4.0 V. The galvanostatic cycling tests were carried out at ambient temperature in the range 2.5–4.5 V using an Arbin battery cycler (model BT-2000).

3. Results and discussion

3.1. Film microstructure and composition

The target materials were thoroughly characterized before to proceed to thin films deposition. The crystalline nature of the

starting powders, as well as structural parameters were determined by XRD [20,21]. Fig. 1 shows the diffraction patterns of the Fe and FeMn thin films. For both the as-prepared films no peaks pertinent to the silicate phase were detected, so we can assume that the films are totally amorphous. Only the peaks due to the gold layer and to the stainless steel substrate are clearly visible (see Fig. 1).

Fig. 2 reports the SEM images of the as-deposited films. The FeMn sample (Fig. 2a) is constituted by two types of particles of different shapes: the film surface is composed by worm-like particles, about 1 μm long and 100–200 nm wide, whereas the part in contact with the substrate is constituted by rounded particles. This layered morphology could be due to the deposition procedure, which comprised two successive steps with different power. In the case of Fe sample (Fig. 2b), the morphology is very different from the one of FeMn, but is again constituted by two different layers: the lower formed by a compact aggregate of small rounded particles and the upper one by bigger particles randomly distributed on the underlying layer.

In order to investigate the composition of the film and the oxidation state of the metal cations, XPS analysis was performed on the FeMn sample. The wide range spectrum (see Fig. 3a) showed peaks of the expected ions pertaining to the orthosilicate target, together with the peak of carbon and Ni. The carbon is a common contaminant for sample growth *ex situ*, while the Ni signal comes from the outer circular ring of the substrate, not covered by the thin film, but completely lightened by the X-ray source and seen by the electron analyzer. Anyway, we cannot exclude the occurrence of an intermixing between Ni and the top $LiMSiO_4$ layer after diffusion of Ni through the Au layer, that could also explain the presence of Ni^{2+} on the cathode surface. For a more detailed analysis, we performed acquisitions of small spectral regions, in the range of the binding energy of the Fe2p (Fig. 3b) and of Li1s, Fe3p and Mn3p one (Fig. 3c). A Shirley-type background was subtracted from each peak and the area subtended by the peak was calculated. Finally, each area was normalized and the intensity of each peak was compared, obtaining the Fe:Mn 2:1 ratio among the elements. Analyzing the Fe2p peaks with their fine structure, that is the fingerprint of the oxidation state of the species, we determined the Fe oxidation state. $Fe2p_{3/2}$ peak has a binding energy of 711.8 eV with a satellite at 718.6 eV, in good accordance with the Fe^{3+} state. For Mn we can base our result just on the binding energy of the $2p_{3/2}$ peak. Its energy is 641.1 eV, in good agreement with Mn^{2+} state. Special care was taken for Li1s peak; in fact, its binding energy is very close to that of the Fe3p one, resulting in just one visible peak. Fig. 3c shows the peak and the fit we performed to separate the two components. This way we were able to evidence the Li presence. Then, we have direct evidence of Fe^{3+} formation, even if only Fe^{2+} should be present for the $Li_2Mn_{0.5}Fe_{0.5}SiO_4$ compound. Anyway, we stress here that XPS probes just the topmost atomic layers (10 nm) so Fe^{3+} is detected on the film surface, and it is likely due to air exposure. In addition, intermixing with elements from the SS substrate, such as Fe and Cr, could have been occurred. This aspect is worth to be investigated in future works.

3.2. Electrochemical properties

The cyclic voltammetry (CV) curves of the Fe and FeMn samples are reported in Fig. 4a and b, respectively. In the case of the Fe film, only one peak is clearly seen during both the anodic and cathodic scans. The oxidation peak at about 3.5 V slightly shifts towards higher voltages by increasing the cycle number. The peak current increases up to the third cycle, then remains stable for the successive cycles. The reduction peak at about 3.2 V seems to shift towards lower values during the 6th cycle.

A similar CV plot was obtained for the FeMn sample (see Fig. 4b) where again a single peak at about 3.4 V was seen at positive currents and at about 3.2 V at negative currents. The reversibility of the intercalation/deintercalation process was so proved for both the thin films. The CV profile of the films is very similar to that found for our target materials, where a peak ascribable to the electron transfer reaction in which Fe^{2+} oxidizes to Fe^{3+} is observed at almost the same potentials (see inset of Fig. 4a and b). Therefore, we can conclude that the films are able to intercalate and deintercalate Li^+ during the electrochemical cycling. These results also give an indirect and circumstantial evidence that the amorphous phase is retaining the lithium orthosilicate composition.

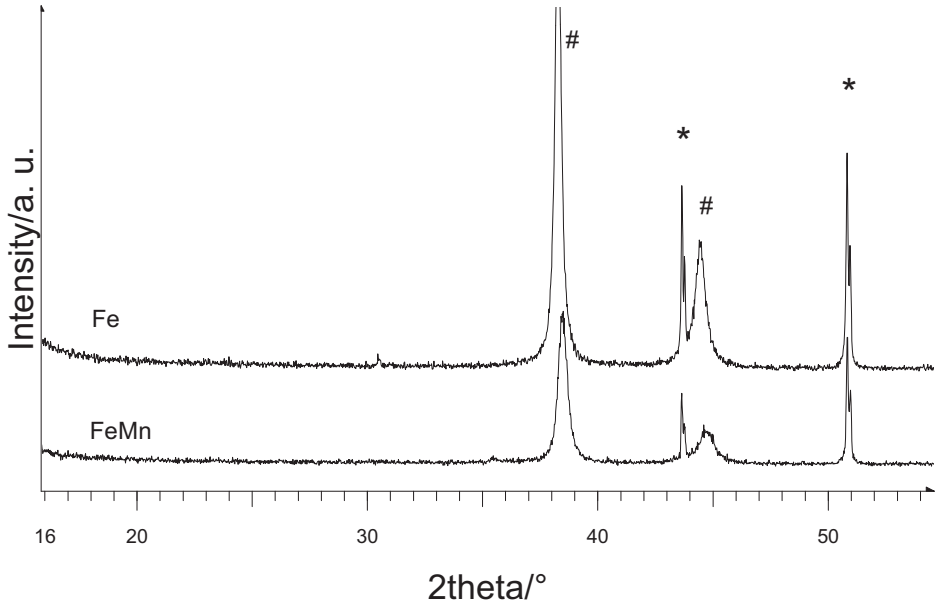

Fig. 1. XRD patterns of the as-deposited Fe and FeMn thin films (* indicate SS substrate reflections and # the gold ones).

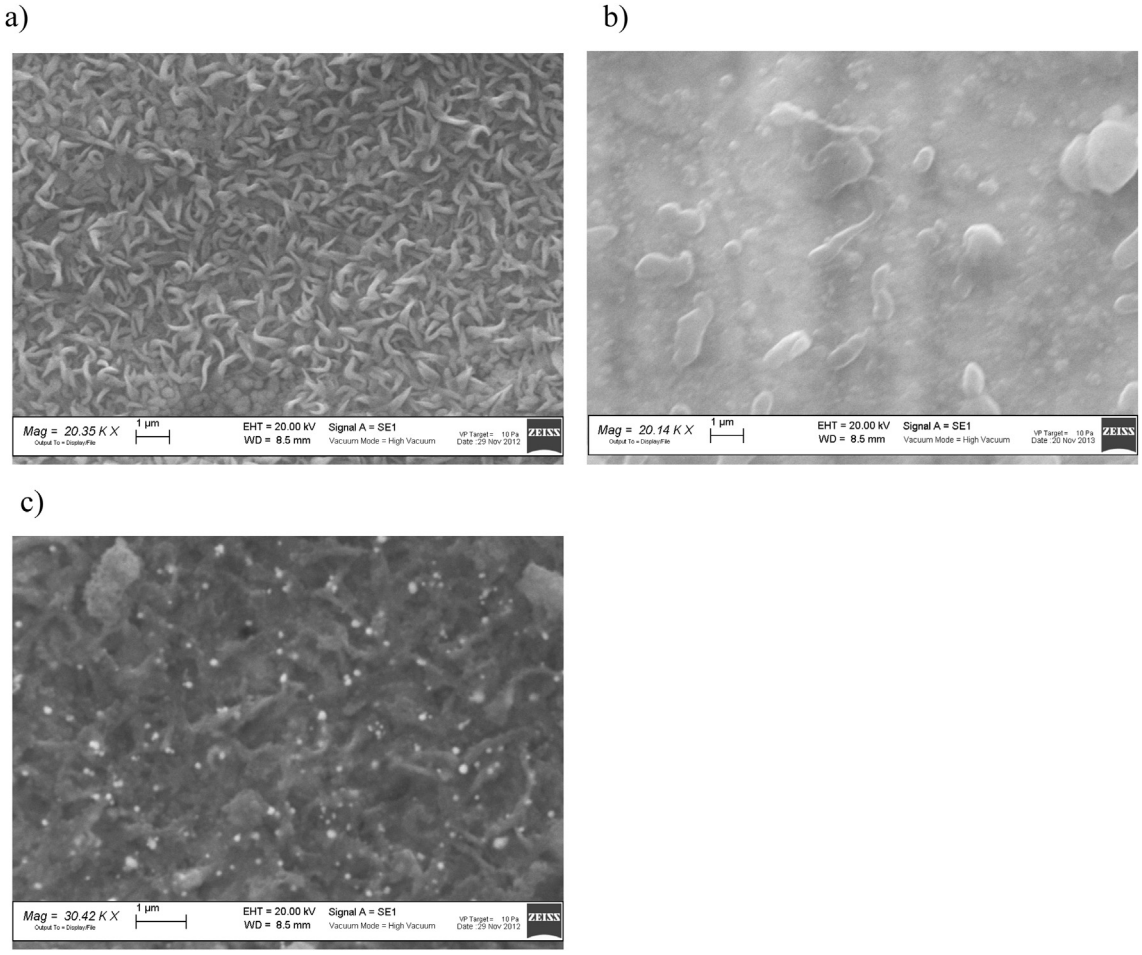

Fig. 2. SEM micrographs of a) as-deposited FeMn, b) as-deposited Fe thin film, c) FeMn thin film after galvanostatic charge–discharge cycling.

The thin films were then tested by galvanostatic charge/discharge measurements, and their performances are reported in Fig. 5a and b. The Fe sample (Fig. 5a) could deliver an initial charge capacity of about 170 mAh g^{-1} for the first cycles at 0.5 C, then the current was raised at 1 C and capacity values around 50 mAh g^{-1} were observed. After 75 cycles, the same galvanostatic test was repeated to check the cell response to repeated cycling, and we obtained a maximum charge capacity of 140 mAh g^{-1} at 0.5 C, which faded immediately in the successive cycles at the same current. However, at current as high as 2.5 C, and after more than 250 cycles, the cell was still able to deliver about 50 mAh g^{-1} with a coulombic efficiency higher than 90% (see Fig. 5a). A very similar behavior was observed for the FeMn sample (Fig. 5b) for which, after an initial very high charge capacity of about 250 mAh g^{-1}, a decrease towards values of about 50 mAh g^{-1} was obtained for 2.5 C current. Noteworthy, at the lower current of 0.5 C, this sample showed a better performance than the Fe one, but with a lower coulombic efficiency (between 70 and 80% at 0.5 C, see Fig. 5b). For microbatteries is also very important to know capacity and current density per surface unit, and the values corresponding to the first cycle at each current density for the last part of the galvanostatic test are reported in Fig. 5c. The calculated values are quite low, but this is not surprising since this is a well known problem of electrodes in form of thin films, for which new 3D architectures has been recently proposed [12–14].

Generally speaking, the observed lower coulombic efficiency with respect to the corresponding target materials may be explained by considering the amorphous nature of the silicate, for which the lacking of a stable crystalline structure can make the Li^+ intercalation/deintercalation process less reversible. After the cycling measurements, the thin film morphology for the FeMn film appears different from the as-prepared sample (Fig. 2c). In particular, the bright, rounded particles could be the lithium salt of the electrolyte, but what is really evident is the formation of a compact layer in which the worm-like particles are not seen anymore. On the other hand, the use of amorphous active materials could help to achieve higher capacity and cyclability, thanks to the presence of additional stable sites for lithium ions, considering the open and random structure typical of amorphous materials. For example, amorphous MoO_2 exhibited better rechargeability than crystalline MoO_2 [34]. Recently, it was also shown that amorphous TiS_3 has better electrochemical properties than its crystalline counterpart, because it retained its structure during the first tests [35]. In this frame, it is helpful to test amorphous thin films as cathode materials. This could also lead to better interfacial properties towards glassy thin film electrolytes such as LIPON. It should be also pointed out that the cycling performances are generally improved when the electrode is covered by a solid-state electrolyte as often reported in the literature [5,36–38]. For our thin films the observed degradation of the capacity retention may partly result from the use of a liquid electrolyte. In addition, the use of EC/DEC up to 4.5 V may contribute to the losses. A liquid electrolyte based on EC/DMC, that can withstand higher voltages up to 4.5–4.6 V, could help in improving the cell performances.

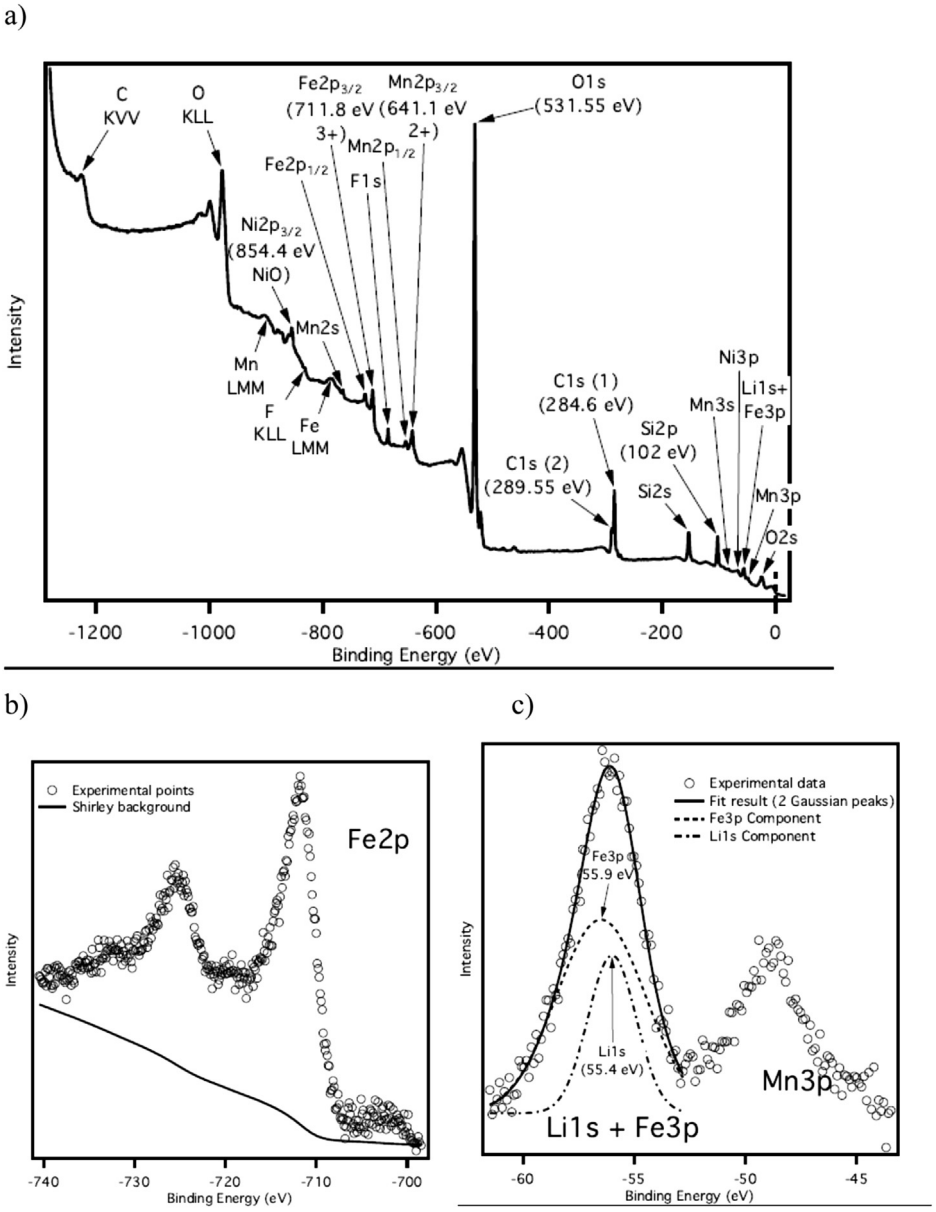

Fig. 3. XPS of FeMn sample: a) wide range spectrum, b) $Fe2p_{3/2}$ photoemission peak, c) Li1s, Mn3p and Fe3p peaks.

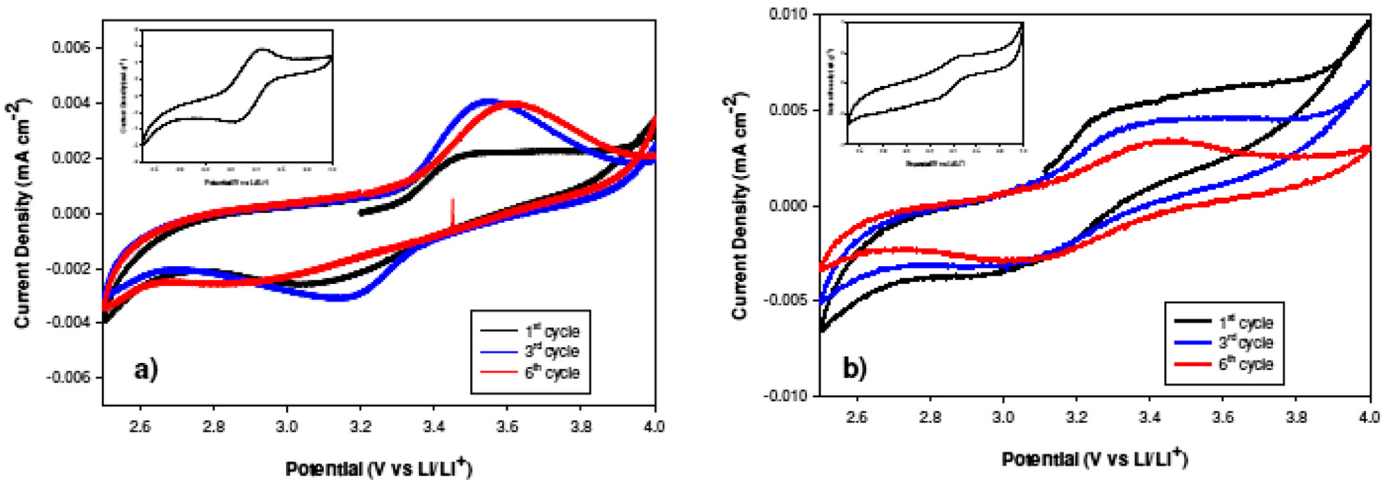

Fig. 4. Cyclic voltammetry plots of a) Fe and b) FeMn samples recorded at 0.2 mV s^{-1} between 2.5 and 4 V. The inset shows CV plots of Fe and FeMn target bulk materials.

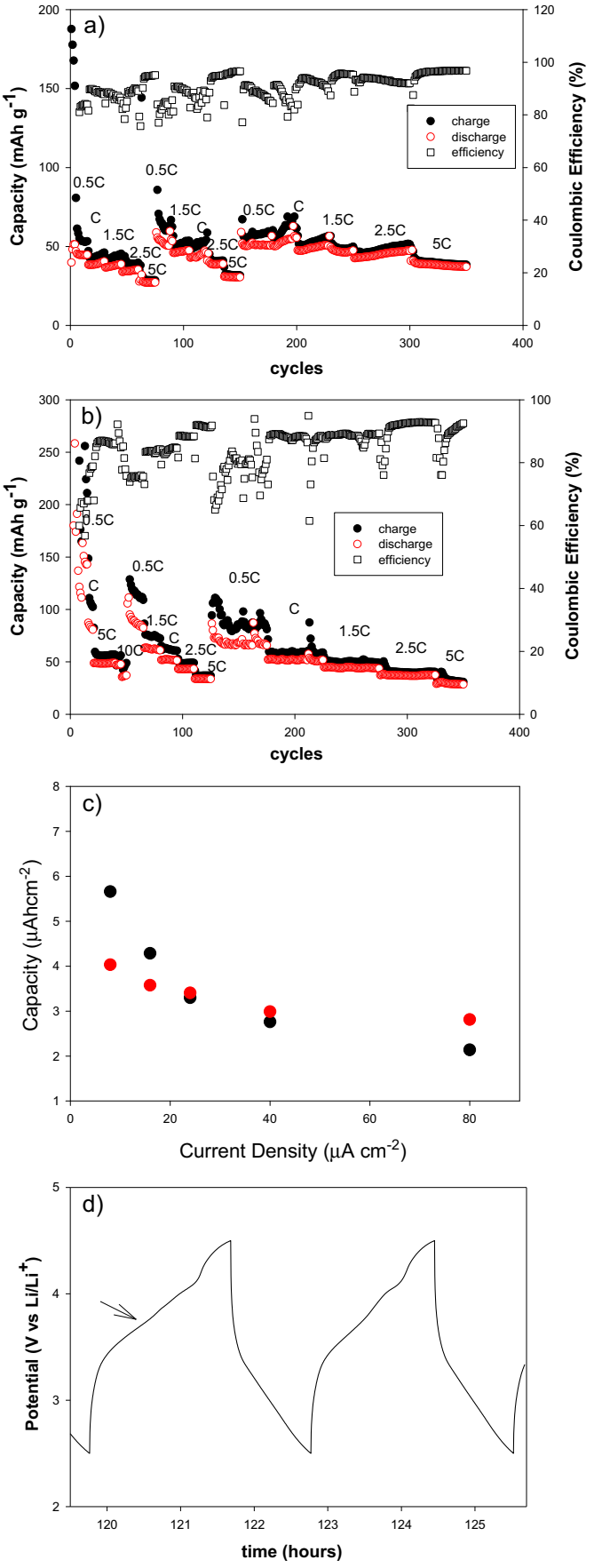

The chronopotentiograms of the FeMn sample are reported in Fig. 5d. In accordance with the CVs, the chronopotentiograms showed a reversible plateau at about 3.5 V, that is clearly visible at least at low current rates, whereas in the charge curve it is less marked. This fact suggests that the Li^+ extraction could proceed in a continuous way, as expected for amorphous materials, rather than with the formation of well-defined phases as expected for crystalline compounds.

4. Conclusions

We successfully deposited lithium iron and iron/manganese orthosilicate amorphous thin films by r.f. sputtering, and preliminary demonstrated their suitability as positive electrodes for lithium batteries. Our films were able to sustain more than 300 galvanostatic cycles with encouraging performances.

Anyway, further improvements can be envisaged by optimizing the deposition parameters such as r.f. power and deposition time, to obtain also crystalline films and to assess their properties with respect to those of the amorphous ones. A future goal is to prepare orthosilicate films with the chance to extract two lithium ions, so obtaining higher capacities and efficiencies.

Acknowledgments

This work was performed in the frame of Cariplo Project 2011-0325 “New electrolyte and electrode materials for thin-film lithium microbatteries”. We kindly thank Mr. Alessandro Girella for the SEM analyses.

References

[1] J.F.M. Oudenhoven, L. Baggetto, P.H.L. Notten, Adv. Energy Mater. 1 (2011) 10–33.
[2] W. Lai, C.K. Erdonmez, T.F. Marinis, C.K. Bjune, N.J. Dudney, F. Xu, R. Wartena, Y.-M. Chiang, Adv. Mater. 22 (2010) E139–E144.
[3] A. Patil, V. Patil, D.W. Shin, Ji-Won Choi, D.-S. Paik, S.-J. Yoon, Mater. Res. Bull. 43 (2007) 1913–1942.
[4] J.W. Long, B. Dunn, D.R. Rolison, H.S. White, Chem. Rev. 104 (2004) 4463–4492.
[5] C. Gerbaldi, M. Destro, Jijeesh R. Nair, S. Ferrari, I. Quinzeni, E. Quartarone, Nano Energy 2 (2013) 1279–1286.
[6] C. Navone, S. Tintignac, J.P. Pereira-Ramos, R. Baddour-Hadjean, R. Salot, Solid State Ionics 192 (2011) 343–346.
[7] E. Ferg, R.J. Gummow, A. de Kock, M.M. Thackeray, J. Electrochem. Soc. 141 (1994) L147–L150.
[8] M. Roberts, P. Johns, J. Owen, D. Brandell, K. Edstrom, G. El Enany, C. Guery, D. Golodnitsky, M. Lacey, C. Lecoeur, H. Mazor, Emanuel Peled, E. Perre, M.M. Shaijumon, P. Simonc, P.-L. Taberna, J. Mater. Chem. 21 (2011) 9876–9890.
[9] P. Birke, W.F. Chu, W. Weppner, Solid State Ionics 93 (1997) 1–15.
[10] S.D. Jones, J.R. Akridge, F.K. Shokooki, Solid State Ionics 69 (1994) 357–368.
[11] M.V. Reddy, B. Pequenard, P. Vinatier, A. Levasseur, J. Phys. Chem. B 110 (2006) 4301–4306.
[12] K. Xie, Z. Lu, H. Huang, W. Lu, Y. Lai, J. Li, L. Zhou, Y. Liu, J. Mater. Chem. 22 (2012) 5560.
[13] J.H. Pikul, P.V. Braun, W.P. King, J. Phys. Conf. Ser. 476 (2013) 012087.
[14] S.J. Dillon, K. Sun, Curr. Opin. Solid State Mater. 16 (2012) 153–162.
[15] X. Zhu, L.-B. Cheng, C.-G. Wang, Z.-P. Guo, P. Zhang, G.-D. Du, H.-K. Liu, J. Phys. Chem. C 113 (2009) 14518–14522.
[16] H. Mazor, D. Golodnitsky, L. Burstein, A. Gladkich, E. Peled, J. Power Sources 198 (2012) 264–272.
[17] V. Palomares, I. Ruiz de Larramendi, J. Alonso, M. Bengoechea, A. Goni, O. Miguel, T. Rojo, Appl. Surf. Sci. 256 (2010) 2563–2568.

Fig. 5. Galvanostatic charge discharge tests at different current rates (0.5, 1, 1.5, 2.5, 5 C) of a) Fe and b) FeMn samples. The Coulombic efficiency is also shown.; c) influence of the current density in μA cm^{-2} (corresponding to 0.5, 1, 1.5, 2.5, 5 C) on the first charge capacity from the 125th cycle onward, (red dots, Fe sample); d) chronopotentiograms of the FeMn sample (13th and 14th cycle of charge–discharge at 0.5 C). (For interpretation of the references to color in this figure legend, the reader is referred to the web version of this article.)

[18] A. Nyten, A. Abouimrane, M. Armand, T. Gustafsson, J.O. Thomas, Electrochem. Commun. 7 (2005) 156–160.
[19] M.S. Islam, R. Dominko, C. Masquelier, C. Sirisopanaporn, A.R. Armstrong, P.G. Bruce, J. Mater. Chem. 21 (2011) 9811–9818.
[20] M. Bini, S. Ferrari, D. Capsoni, C. Spreafico, C. Tealdi, P. Mustarelli, J. Solid State Chem. 200 (2013) 70–75.
[21] M. Bini, S. Ferrari, C. Ferrara, M.C. Mozzati, D. Capsoni, A.J. Pell, G. Pintacuda, P. Canton, P. Mustarelli, Sci. Rep. 3 (2013) 3452, http://dx.doi.org/10.1038/srep03452.
[22] R. Dominko, C. Sirisopanaporn, C. Masquelier, D. Hanzel, I. Arcon, M. Gaberscek, J. Electrochem. Soc. 157 (2010) A1309–A1316.
[23] M.M. Kalantarian, S. Asgari, P. Mustarelli, J. Mater. Chem. A 1 (2013) 2847–2855.
[24] A.R. Armstrong, N. Kuganathan, M.S. Islam, P.G. Bruce, J. Am. Chem. Soc. 133 (2011) 13031–13035.
[25] C. Sirisopanaporn, C. Masquelier, P.G. Bruce, A.R. Armstrong, R. Dominko, J. Am. Chem. Soc. 133 (2011) 1263–1265.
[26] T. Kawase, H. Yoshitake, Microporous Mesoporous Mater. 155 (2012) 99–105.
[27] D. Rangappa, K.D. Murukanahally, T. Tomai, A. Unemoto, I. Honma, Nano Lett. 12 (2012) 1146–1151.
[28] Z. Chen, S. Qiu, Y. Cao, J. Qian, X. Ai, K. Xi, X. Hong, H. Yang, J. Mater. Chem. A 1 (2013) 4988–4992.
[29] R. Dominko, M. Bele, A. Kokalj, M. Gaberscek, J. Jamnik, J. Power Sources 174 (2007) 457.
[30] I. Quinzeni, S. Ferrari, E. Quartarone, P. Mustarelli, J. Power Sources 196 (2011) 10228–10233.
[31] C. Tealdi, E. Quartarone, P. Galinetto, M.S. Grandi, P. Mustarelli, J. Solid State Chem. 199 (2013) 1–6.
[32] X.J. Wu, Z.Z. Zhang, Q.S. Liang, J. Meng, J. Cryst. Growth 340 (2012) 74–77.
[33] Y. Xu, Y. Li, S. Liu, H. Li, Y. Liu, J. Power Sources 220 (2012) 103–107.
[34] J.H. Ku, J.H. Ryu, S.H. Kim, O.H. Han, S.M. Oh, Adv. Funct. Mater. 22 (2012) 3658–3664.
[35] T. Matsuyama, A. Sakuda, A. Hayashi, Y. Togawa, S. Mori, M. Tatsumisago, J. Solid State Electrochem. 17 (2013) 2697–2701.
[36] X. Yu, J.B. Bates, G.E. Jellison, F.X. Hart, J. Electrochem. Soc. 144 (1997) 524–532.
[37] L. Baggetto, N.A.M. Verhaegh, R.A.H. Niessen, F. Roozeboom, J.-C. Jumas, P.H.L. Notten, J. Electrochem. Soc. 157 (2010) A340–A347.
[38] N.J. Dudney, J.B. Bates, R.A. Zuhr, S. Young, J.D. Robertson, H.P. Jun, S.A. Hackney, J. Electrochem. Soc. 146 (1999) 2455–2464.

7

Segregation and selective oxidation of Ni atoms in $Pt_3Ni(111)$ in a low-pressure oxygen environment

Most of the energy loss in a PEMFC consists in the overpotential needed to dissociate the O_2 at the cathode. Today the only catalyst capable to reduce significantly the oxygen dissociation energy is platinum, but its extremely rare occurrence on the earth prevents the wide distribution of this technology. The key to make this technology cost effective is to find viable alternatives to platinum.

Bimetallic alloys present often improved catalytic performances with respect to their metal components, and it has been shown that $Pt_3Ni(111)$ alloy exhibits greater performance than a pure Pt surface [48].

In this paper we studied the oxidation kinetic of a $Pt_3Ni(111)$ surface. In particular we focused on the surface composition: the clean surface shows a platinum skin with a Ni-rich second layer, while after an annealing in oxygen atmosphere the nickel seems to segregate on the surface binding selectively the oxygen.

THE JOURNAL OF PHYSICAL CHEMISTRY C

Article

pubs.acs.org/JPCC

Segregation and Selective Oxidation of Ni Atoms in $Pt_3Ni(111)$ in a Low-Pressure Oxygen Environment

A. Politano,[†] M. Caputo,[†,‡] A. Goldoni,[‡] P. Torelli,[§] and G. Chiarello[†,∥,*]

[†]Dipartimento di Fisica, Università degli Studi della Calabria, 87036 Rende (Cs), Italy

[‡]ST-INSTM Lab., Elettra Sincrotrone Trieste S.C.p.A., s.s. 14 km 163.5 in Area Science Park, 34149 Trieste, Italy

[§]Laboratorio TASC, IOM-CNR, s.s. 14 km 163.5 in Area Science Park, 34149 Trieste, Italy

[∥]Consorzio Nazionale Interuniversitario di Scienze Fisiche della Materia, via della Vasca Navale, 84, 00146 Roma, Italy

ABSTRACT: Understanding the microscopic mechanism of oxygen interaction with the surfaces of Pt-based alloys is an important issue for applications in various fields such as corrosion and oxygen reaction reduction in fuel cells, for which Pt-based alloys are more efficient catalysts with respect to platinum. Herein, the interaction of oxygen with $Pt_3Ni(111)$ has been studied by X-ray photoemission, X-ray absorption, and high-resolution electron energy loss spectroscopies. We have found that the oxidation of $Pt_3Ni(111)$ at 600 K leads to the segregation of Ni atoms to the surface region. The presence of Ni atoms at the $Pt_3Ni(111)$ surface allows O_2 to dissociate to form NiO_x surface species. High-resolution electron energy loss spectroscopy measurements performed on Pt(111), Ni(111), and $Pt_3Ni(111)$ directly show that, on the $Pt_3Ni(111)$ surface, oxygen binds selectively on Ni sites and, moreover, that the O−Ni bond formed on Pt_3Ni is weaker than the O−Pt bond formed on Pt(111).

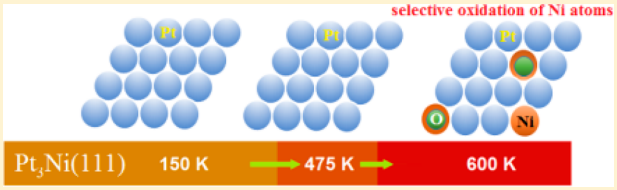

INTRODUCTION

Platinum is a precious and expensive noble metal commonly used as a catalyst in numerous chemical reactions.[1−4] For example, Pt is the most efficient catalyst in hydrogen-fuel cells and in CO oxidation.[5−7] Hence, lowering the amounts of Pt at the catalytic surface is a critical mission for technology transfer. Indeed, generally it has been reported that bimetallic alloys have superior catalytic properties with respect to the pure metal.[8−12] As an example, Stamenkovic and co-workers have reported that the $Pt_3Ni(111)$ surface is more active than Pt(111) and current state-of-the-art Pt/C catalysts for the oxygen reduction reaction in fuel cells.[13] Likewise, the use of bimetallic surfaces has led to the design of novel catalysts with improved reaction rates and chemical selectivity.[14,15]

Here, we have used synchrotron radiation X-ray photoemission (XPS) and X-ray absorption (XAS) spectroscopies as well as high-resolution electron energy loss spectroscopy (HREELS) to investigate the oxidation of $Pt_3Ni(111)$.

The $Pt_3Ni(111)$ surface at room temperature has a peculiar atomic arrangement.[13,16−19] In particular, the outermost and the third surface layers are Pt-rich, while the second atomic layer is Ni-rich. However, the atomic (Ni, Pt) diffusion and segregation with the temperature can lead to a different surface composition. Despite their importance, scarce information is available about diffusion and segregation at higher temperature.

Moreover, the interaction of oxygen with surface alloys is particularly important for studying the corrosion and passivation mechanisms[20,21] and for the prospect of selective oxidation of surface atoms of the alloy.

Core level XPS and XAS show that, at 600 K and in an oxygen environment, Ni atoms segregate toward the surface region and form surface NiO_x species. The valence band of the $NiO_x/Pt_3Ni(111)$ sample is dominated by an electronic state at 2 eV, arising from the hybridization between O 2p and Ni 3d states. Moreover, HREELS experiments indicate that on the Ni-rich surface oxygen binds selectively to Ni atoms.

EXPERIMENTAL SECTION

The $Pt_3Ni(111)$ sample was purchased from MaTecK GmbH. The substrate was cleaned by repeated cycles of ion sputtering and annealing at 1000 K. Surface cleanliness and order were checked using XPS and low-energy electron diffraction (LEED) measurements, respectively. The $Pt_3Ni(111)$ sample showed an excellent LEED pattern with bright spots.

XPS and XAS measurements were carried out at the Advanced Photoelectric Experiments (APE) beamline of the Elettra synchrotron in Trieste (Italy). The APE high-energy (APE-HE) beamline delivers a high-flux focalized photon beam with photon energy ranging from 150 to 1600 eV and with a resolving power of 7000 at 400 eV. The detection system consists of an Omicron EA125 electron energy analyzer for photoemission experiments.

The experimental setup includes a preparation chamber connected to the APE-HE end station through a transfer system in ultrahigh vacuum (UHV).

Received: October 6, 2013
Revised: November 7, 2013
Published: November 19, 2013

HREELS experiments were performed at University of Calabria (Unical), Italy. The experimental apparatus at Unical consists of an ultrahigh vacuum chamber equipped with standard facilities for surface characterization, described elsewhere,[22,23] and with an electron energy loss spectrometer (Delta 0.5, SPECS). HREEL spectra were taken in the specular direction (angle of incidence 55° with respect to the sample normal) with an impinging energy of 4 eV, and the energy resolution was set at 2−3 meV.

RESULTS AND DISCUSSION

Figure 1 shows the evolution of the valence band of $Pt_3Ni(111)$ as a function of the oxygen exposure, carried out at 600 K. The

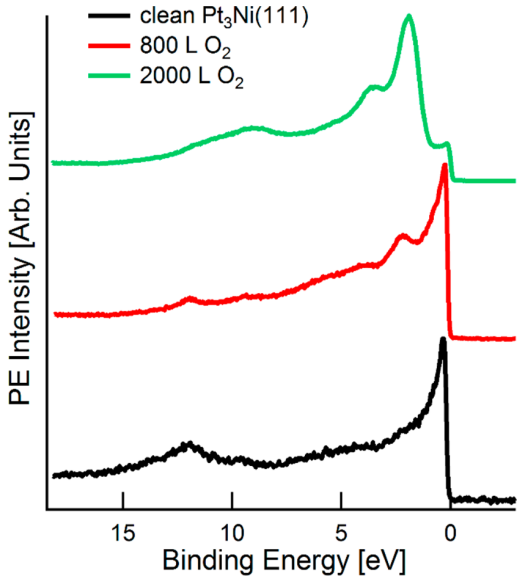

Figure 1. Photoemission from the valence band of the bare $Pt_3Ni(111)$ and for the same surface exposed to 800 and 2000 L of O_2 at 600 K, respectively. Measurements have been taken at room temperature and with a photon energy of 300 eV.

pristine $Pt_3Ni(111)$ shows d states just located in the nearness of the Fermi level. An additional weak feature is recorded at a binding energy of 12.0 eV. The exposure of the $Pt_3Ni(111)$ to oxygen ($p(O_2) = 5 \times 10^{-7}$ mbar) causes dramatic changes near the Fermi level. For an intermediate oxidation (800 L, 1 L = 1.33×10^{-6} mbar), an intense peak appears at 2.0 eV, while weak features are recorded at 4.0 and 9.2 eV, respectively. We assign the peak at 2.0 eV to the hybridization of p states of oxygen with Ni d bands. For increasing oxidation, the peak at 2.0 eV becomes more intense, and moreover, other states at 3.6 and 9.1 eV appear.

Such assignment is confirmed also by the inspection of the spectra reported in Figure 2, where we show the evolution of the Pt 4f and Ni 3p states with oxygen exposure.

While the Pt 4f core levels do not show any shift upon oxygen exposure (Figure 2), the Ni 3p core levels exhibit dramatic changes. In the clean $Pt_3Ni(111)$ sample, the Ni $3p_{3/2}$ has a binding energy of 65.5 eV, while the Ni $3p_{1/2}$ is not spectroscopically resolved due to its weakness. After oxidation, the Ni $3p_{3/2}$ shifts to 67.1 eV, and this indicates that most of the Ni atoms have interacted with oxygen.

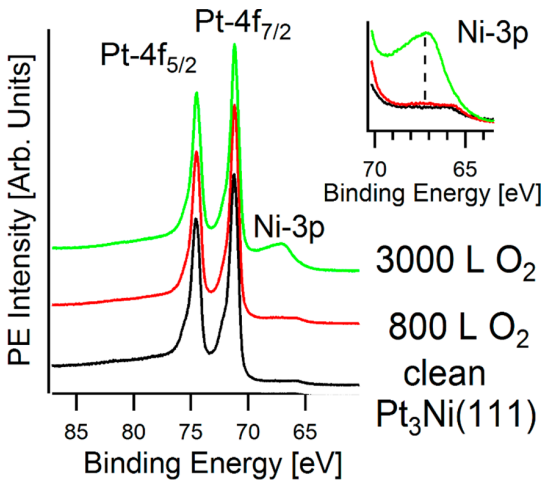

Figure 2. XPS experiments on Pt 4f and Ni $3p_{3/2}$ core levels for the bare $Pt_3Ni(111)$ and for the same surface exposed to 800 and 2000 L of O_2 at 600 K, respectively. In the inset, the Ni $3p_{3/2}$ region is magnified. A weak feature at a binding energy of 52 eV is observed and assigned to the Pt $5p_{3/2}$ core level. Notice that core level Ni $3p_{1/2}$ and Pt $5p_{1/2}$ are too weak to be observed in this scale.

Hence, results in Figure 1 and Figure 2 unambiguously demonstrate that a selective oxidation of Ni atoms occurs, while Pt atoms do not interact appreciably with oxygen.

The formation of a surface NiO_x phase in these conditions could play a major role in many catalytic processes. In fact, the oxidation of the sample has long been thought to lead to a poisoning of the chemical activity of the surface.[24] However, it is now well established[25] that surface oxides are active centers in many chemical reactions and, in particular, for CO oxidation on many metal samples.[25] Moreover, the present results agree with measurements reporting that the highest activity of PtCo nanoparticles toward oxygen reduction reaction is obtained for samples composed of small amounts of Co/Co oxides decorating the Pt-rich surface of the Pt_3Co sample.[26]

To provide more detailed information on the oxidation state of the $Pt_3Ni(111)$ surface, we have carried out a XAS experiment on Ni L edges. The $L_{2,3}$ absorption spectra relate to the transition of a 2p core state to an empty state. At the edge, the spectra are dominated by 2p → 3d transitions.

Upon oxidation, several features appear in the XAS spectrum due to the presence of multiplets. In particular, a double-peak feature is clearly visible in the L_2 edges of Ni (Figure 3). It is well-known that the presence of multiplets constitutes a fingerprint of NiO_x formation.[27] This finding confirms the occurrence of the selective oxidation of Ni atoms and the appearance of Ni^{2+} species.

Hence, photoemission for both valence bands and core levels as well as XAS results indicate that the Pt-skin[13,17,18,28−30] of $Pt_3Ni(111)$ is thermodynamically unstable with adsorbed oxygen.

The oxidation processes of a Pt−Ni−Pt(111) structure have been investigated in ref 31 by Menning et al. Therein, the possible segregation of Ni atoms toward the outermost Pt layer (Pt-skin) has been suggested to occur at 450 K. The activation barrier of the segregation of subsurface Ni atoms in these systems has been estimated to be 15 kcal/mol.[31]

However, all measurements reported here have been recorded at room temperature (with the oxidation performed at 600 K). Thus, we suggest that once the O−Ni bond is

dx.doi.org/10.1021/jp409917b | J. Phys. Chem. C 2013, 117, 27007−27011

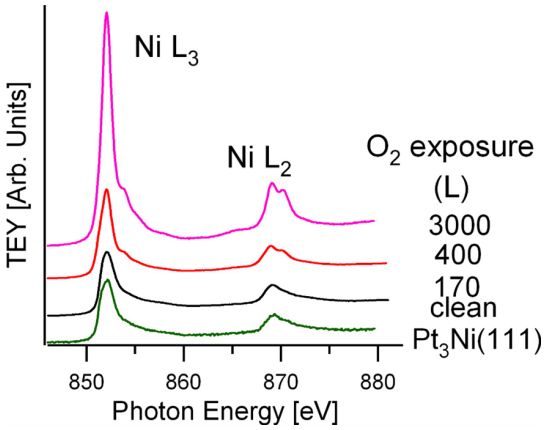

Figure 3. XAS experiments on the clean $Pt_3Ni(111)$ and the same surface exposed to different amounts of O_2 at 600 K.

formed the Ni species remain in the near-surface region, so as to alter the stoichiometry in the near-surface region of the alloy as compared with the pristine $Pt_3Ni(111)$ which exhibits a Pt-skin.

This conclusion is directly supported by XPS measurements on Ni 3p core levels performed as a function of the photon energy (Figure 4). The branching ratio between the Pt 4f and Ni 3p decreases for low photon energies, which are more surface sensitive. This suggests the occurrence of Ni diffusion in the near-surface region.

The oxidation process of the $Pt_3Ni(111)$ has been further investigated by HREELS measurements. In Figure 5 we show the loss spectrum for Ni(111), Pt(111), and $Pt_3Ni(111)$ samples exposed to 100 L of O_2 at 600 K. The oxidized Ni(111) sample shows the characteristic loss spectrum with a phonon mode at 25 meV and the O−Ni vibration at 70 meV.[32] Weaker features are present at higher energies.

The HREELS spectrum of O/Pt(111) is rather complicated with features at 50 and 75 meV and an intense mode at 103 meV. Similar vibrational peaks have been reported by Ibach and co-workers.[33] Differences in vibrational energies are ascribed to the different O coverage and, more importantly, to the different temperature. In particular, our sample is an oxided surface, while the phase studied in ref 33 is a chemisorbed O phase.

Instead, the oxidized $Pt_3Ni(111)$ sample shows a main feature at 75 meV and a broad band with weak intensity in the 80−140 meV range. We note that the oxidation processes produce similar loss features in both Ni(111) and $Pt_3Ni(111)$, thus suggesting the formation of Ni−O complexes on the surface of the Pt_3Ni alloy.

To fasten O-based chemical reactions, O_2 molecules should easily dissociate at the catalyst surface. The resulting atomic oxygen should bind to the catalyst not too strongly to allow reactions with other species.

We suggest that the segregation of Ni atoms and their selective oxidation could deeply influence the reactivity of the Pt_3Ni alloy with respect to pure Pt. In fact, oxygen binds more weakly on the oxidized $Pt_3Ni(111)$ (main feature at 70 meV) than on Pt(111), for which the main O−Pt feature is located at 103 meV. As the O-substrate vibration directly reflects the strength of the O-substrate bond, the O−Ni bond is as strong in $Pt_3Ni(111)$ as in Ni(111). As a comparison, the O−Pt stretching in Pt(111) is revealed at 58 meV.[33] It has been proposed that oxygen is more tightly bound and more localized

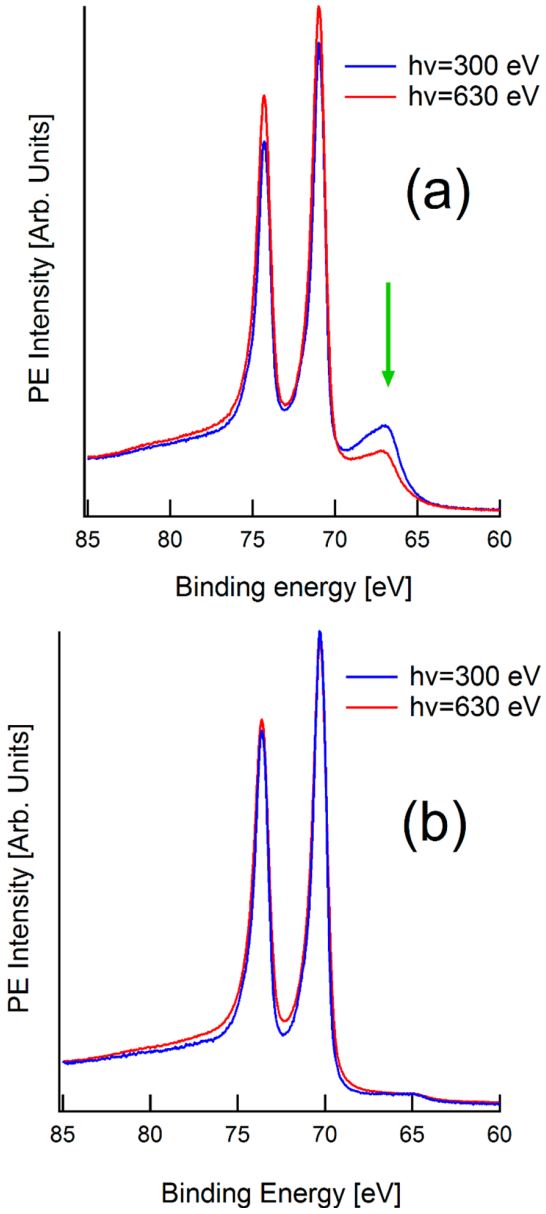

Figure 4. Pt 4f and Ni 3p core levels acquired at a photon energy of 300 and 630 eV for (a) the oxidized and (b) the pristine $Pt_3Ni(111)$ samples, respectively.

on Pt/Ni(111) than on pure Pt(111),[34] but our results suggest that this generalization may not be straightforward due to the selective bonding of O on Ni atoms.

Calculations by Mavrikakis et al.[35] reported that the enhanced ORR activity of the Co/Pt alloy surface, as compared with monometallic Pt, is reduced by the O-poisoning effect due to the weaker metal−O bond on the bimetallic surface. Our HREELS results demonstrate that in the oxidation of $Pt_3Ni(111)$ there is no softening of the metal−O bond but just a preferential adsorption of O on Ni atoms. Furthermore, the ORR activity of the $Pt_3Ni(111)$ remains very high, even in the presence of features in the valence band which are a fingerprint of the occurred oxidation (see the valence band reported in ref 13).

dx.doi.org/10.1021/jp409917b | J. Phys. Chem. C 2013, 117, 27007−27011

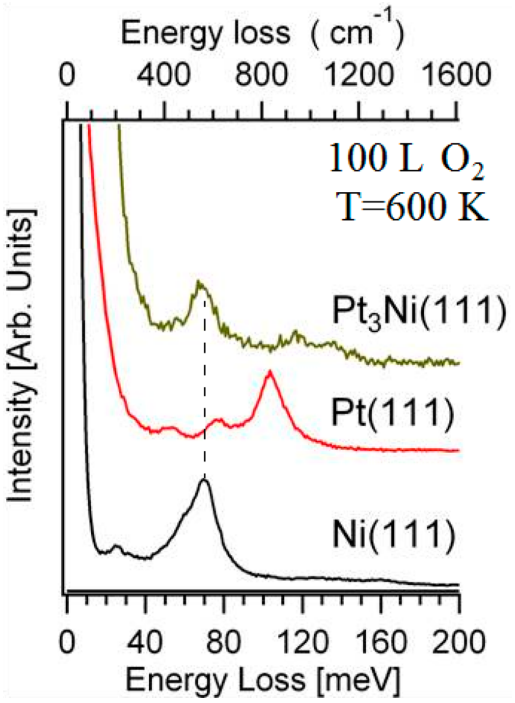

Figure 5. HREELS spectra of Ni(111), Pt(111), and $Pt_3Ni(111)$ surfaces exposed to 100 L of O_2 at T = 600 K.

In conclusion, we have found that at 600 K and in an oxygen environment nickel atoms of $Pt_3Ni(111)$ segregate at the surface, and they selectively bond with O, forming NiO_x species. Our measurements show that oxygen on Ni centers binds more weakly than on Pt sites.

AUTHOR INFORMATION

Corresponding Author

*Tel.: +39-0984-496157. Fax: +39-0984-494401.

Notes

The authors declare no competing financial interest.

ACKNOWLEDGMENTS

A.P. thanks Regione Calabria for financial support.

REFERENCES

(1) Hellsing, B.; Gao, S. W. Molecular Chemisorption Of Oxygen On Cu(100), Ni(100) And Pt(111). *Solid State Commun.* **1994**, *90*, 223−228.

(2) Meng, S.; Wang, E. G.; Gao, S. Water Adsorption On Metal Surfaces: A General Picture From Density Functional Theory Studies. *Phys. Rev. B* **2004**, *69*, 195404.

(3) Mcclure, S. M.; Goodman, D. W. New Insights Into Catalytic CO Oxidation On Pt-Group Metals At Elevated Pressures. *Chem. Phys. Lett.* **2009**, *469*, 1−13.

(4) Anghel, A. T.; Hoyle, R. B.; Irurzun, I. M.; Proctor, M. R. E.; King, D. A. Theoretical Study Of Pattern Formation During The Catalytic Oxidation Of CO On Pt{100} At Low Pressures. *J. Chem. Phys.* **2007**, *127*, 164711.

(5) Alavi, A.; Hu, P.; Deutsch, T.; Silvestrelli, P. L.; Hutter, J. CO Oxidation On Pt(111): An Ab Initio Density Functional Theory Study. *Phys. Rev. Lett.* **1998**, *80*, 3650−3653.

(6) Ehteshami, S. M. M.; Jia, Q.; Halder, A.; Chan, S. H.; Mukerjee, S. The Role Of Electronic Properties Of Pt And Pt Alloys For Enhanced Reformate Electro-Oxidation In Polymer Electrolyte Membrane Fuel Cells. *Electrochim. Acta* **2013**, *107*, 155−163.

(7) Sun, S.; Zhang, G.; Geng, D.; Chen, Y.; Li, R.; Cai, M.; Sun, X. A Highly Durable Platinum Nanocatalyst For Proton Exchange Membrane Fuel Cells: Multiarmed Starlike Nanowire Single Crystal. *Angew. Chem.* **2011**, *123*, 442−446.

(8) Hansgen, D. A.; Vlachos, D. G.; Chen, J. G. Using First Principles To Predict Bimetallic Catalysts For The Ammonia Decomposition Reaction. *Nature Chem.* **2010**, *2*, 484−489.

(9) Inderwildi, O. R.; Jenkins, S. J.; King, D. A. When Adding An Unreactive Metal Enhances Catalytic Activity: Nox Decomposition Over Silver-Rhodium Bimetallic Surfaces. *Surf. Sci.* **2007**, *601*, L103−L108.

(10) Jacobsen, C. J. H.; Dahl, S.; Clausen, B. S.; Bahn, S.; Logadottir, A.; Nørskov, J. K. Catalyst Design By Interpolation In The Periodic Table: Bimetallic Ammonia Synthesis Catalysts. *J. Am. Chem. Soc.* **2001**, *123*, 8404−8405.

(11) Linic, S.; Jankowiak, J.; Barteau, M. A. Selectivity Driven Design Of Bimetallic Ethylene Epoxidation Catalysts From First Principles. *J. Catal.* **2004**, *224*, 489−493.

(12) Nilekar, A. U.; Xu, Y.; Zhang, J.; Vukmirovic, M. B.; Sasaki, K.; Adzic, R. R.; Mavrikakis, M. Bimetallic And Ternary Alloys For Improved Oxygen Reduction Catalysis. *Top. Catal.* **2007**, 1−9.

(13) Stamenković, V. R.; Fowler, B.; Mun, B. S.; Wang, G.; Ross, P. N.; Lucas, C. A.; Marković, N. M. Improved Oxygen Reduction Activity On $Pt_3Ni(111)$ Via Increased Surface Site Availability. *Science* **2007**, *315*, 493−497.

(14) Chen, J. G.; Menning, C. A.; Zellner, M. B. Monolayer Bimetallic Surfaces: Experimental And Theoretical Studies Of Trends In Electronic And Chemical Properties. *Surf. Sci. Rep.* **2008**, *63*, 201−254.

(15) Baraldi, A.; Bianchettin, L.; De Gironcoli, S.; Vesselli, E.; Lizzit, S.; Petaccia, L.; Comelli, G.; Rosei, R. Enhanced Chemical Reactivity Of Under-Coordinated Atoms At Pt-Rh Bimetallic Surfaces: A Spectroscopic Characterization. *J. Phys. Chem. C* **2011**, *115*, 3378−3384.

(16) Chiarello, G.; Marino, A. R.; Formoso, V.; Politano, A. The Adsorption And Co-Adsorption Of Oxygen And Carbon Monoxide On $Pt_3Ni(111)$: A Vibrational Study. *J. Chem. Phys.* **2011**, *134*, 224705.

(17) Yang, Z.; Wang, J.; Yu, X. The Adsorption, Diffusion And Dissociation Of O_2 On Pt-Skin $Pt_3Ni(111)$: A Density Functional Theory Study. *Chem. Phys. Lett.* **2010**, *499*, 83−88.

(18) Pillay, D.; Johannes, M. D. Effect Of S On Pt(111) And $Pt_3Ni(111)$ Surfaces: A First Principles Study. *J. Phys. Chem. C* **2008**, *112*, 1544−1551.

(19) Jacob, T.; Goddard, W. A., III Adsorption Of Atomic H And O On The (111) Surface Of Pt_3Ni Alloys. *J. Phys. Chem. B* **2004**, *108*, 8311−8323.

(20) Das, N. K.; Shoji, T. Early Stage Oxidation Of Ni−Cr Binary Alloy (111), (110) And (100) Surfaces: A Combined Density Functional And Quantum Chemical Molecular Dynamics Study. *Corros. Sci.* **2013**, *73*, 18−31.

(21) Politano, A.; Formoso, V.; Chiarello, G. Chemical Reactions At Clean And Alkali-Doped Mismatched Metal/Metal Interfaces. *J. Phys. Chem. C* **2009**, *113*, 316−320.

(22) Politano, A.; Chiarello, G. Unravelling Suitable Graphene-Metal Contacts For Graphene-Based Plasmonic Devices. *Nanoscale* **2013**, *5*, 8215−8220.

(23) Politano, A.; Chiarello, G.; Benedek, G.; Chulkov, E. V.; Echenique, P. M. Vibrational Measurements On Alkali Coadsorption Systems: Experiments And Theory. *Surf. Sci. Rep.* **2013**, *68*, 305−389.

(24) Fouquet, P.; Witte, G. Monitoring Of Electronic Poisoning Of Ultrathin Alkali Metal Films By Oxygen And Carbon Monoxide Adsorption. *Surf. Sci.* **2000**, *454*, 256−261.

(25) Hendriksen, B. L. M.; Frenken, J. W. M. CO Oxidation On Pt(110): Scanning Tunneling Microscopy Inside A High-Pressure Flow Reactor. *Phys. Rev. Lett.* **2002**, *89*, 046101.

(26) Wang, D.; Xin, H. L.; Hovden, R.; Wang, H.; Yu, Y.; Muller, D. A.; Disalvo, F. J.; Abruña, H. D. Structurally Ordered Intermetallic Platinum−Cobalt Core−Shell Nanoparticles With Enhanced Activity And Stability As Oxygen Reduction Electrocatalysts. *Nat. Mater.* **2013**, *12*, 81−87.
(27) Ikeno, H.; De Groot, F. M. F.; Stavitski, E.; Tanaka, I. Multiplet Calculations Of $L_{2,3}$ X-Ray Absorption Near-Edge Structures For 3d Transition-Metal Compounds. *J. Phys.: Condens. Matter* **2009**, *21*, 104208.
(28) Fowler, B.; Lucas, C. A.; Omer, A.; Wang, G.; Stamenković, V. R.; Marković, N. M. Segregation And Stability At $Pt_3Ni(111)$ Surfaces And $Pt_{75}Ni_{25}$ Nanoparticles. *Electrochim. Acta* **2008**, *53*, 6076−6080.
(29) Stamenković, V.; Schmidt, T. J.; Ross, P. N.; Marković, N. M. Surface Segregation Effects In Electrocatalysis: Kinetics Of Oxygen Reduction Reaction On Polycrystalline Pt_3Ni Alloy Surfaces. *J. Electroanal. Chem.* **2003**, *554*−*555*, 191−199.
(30) Zhang, J.; Yang, H.; Fang, J.; Zou, S. Synthesis And Oxygen Reduction Activity Of Shape-Controlled Pt_3Ni Nanopolyhedra. *Nano Lett.* **2010**, *10*, 638−644.
(31) Menning, C. A.; Hwu, H. H.; Chen, J. G. Experimental And Theoretical Investigation Of The Stability Of Pt−3d−Pt(111) Bimetallic Surfaces Under Oxygen Environment. *J. Phys. Chem. B* **2006**, *110*, 15471−15477.
(32) Ibach, H.; Bruchmann, D. Observation Of Surface Phonons On Ni(111) By Electron Energy-Loss Spectroscopy. *Phys. Rev. Lett.* **1980**, *44*, 36−39.
(33) Steininger, H.; Lehwald, S.; Ibach, H. Adsorption Of Oxygen On Pt(111). *Surf. Sci.* **1982**, *123*, 1−17.
(34) Jacob, T.; Merinov, B. V.; Goddard, W. A., III Chemisorption Of Atomic Oxygen On Pt(111) And Pt/Ni(111) Surfaces. *Chem. Phys. Lett.* **2004**, *385*, 374−377.
(35) Xu, Y.; Ruban, A. V.; Mavrikakis, M. Adsorption And Dissociation Of O_2 On Pt-Co And Pt-Fe Alloys. *J. Am. Chem. Soc.* **2004**, *126*, 4717−4725.

Conclusions

In this thesis I dealt with many problems related to renewable energy harvesting and storage. Even if my studies are base research, finalized to generate new knowledge on the investigated systems, the final aim has always been to contribute to build better devices: more efficient solar cell, safer batteries, or cheaper fuel cells.

Most of my efforts were concentrated in studying new alternatives for molecular photovoltaics. In particular, using the powerful tool of Resonant Photoemission, we demonstrated that the charge transfer time of Zn-Tetra Phenyl Porphirin on ZnO is one order of magnitude lower than Ru-based dyes on TiO_2. This can open different routes in the development of Dye Sensitized Solar Cells. The possibility to substitute Ru-based dyes with the much cheaper Zn-based porphyrin, and the fact that one of the process involved in the photocurrent generation in DSSC is even more efficient, can revitalize the DSSC field, opening the way to a new series of experiment based on this interface.

Similar to Zn-TPP, Octa Ethyl Porphiryn is another good candidate to be an absorber in molecular photovoltaics. Using Photoemission, Near Edge X-ray Absorption Spectroscopy, Inverse Photoemission, and GW calculations, we investigated the solid state effects that occurs to the frontier orbitals of H2OEP. Screening effects and symmetry breaking have been found to be responsible of the gap shrinking and LUMO/LUMO+1 degeneracy lifting. Knowing these effects means having a new degree of freedom to control the electronic structure of this molecule, this can help to tailor new interfaces for better devices.

Picene/C_{60} is a completely new interface investigated in this thesis. In the attempt of building a new donor - acceptor heterojunction, we discovered a way to control doping in K-doped C_{60}. The emergence of an unexpected metallic system for Picene/C_{60} heterojunction, and the possibility to finely control the doping level of C_{60}, can represent a solution to the problem of C_{60} phase separations. New experiments based on C_{60} superconductivity can prove if this system is still a superconductor, and how the observed screening of correlation effect influence the transition temperature.

Another important way to tailor device characteristics is to control their morphology. Nanoimprinting Lithography can be used to build nanometric structures on polymers in order to help the charge flowing in devices, but also to modify the conductivity and the electronic structure of the polymer itself. We investigated the effects of this treatment on the electronic structure of PEDOT:PSS, a commonly used polymer in organic photovoltaic. Thanks to photoelectron spectroscopy we found that controlling nanoimprintng process parameters will result in controlled shift of both valence band offset and work function. The possibility to tune this two key parameter for organic photovoltaic pave the way to new applications of PEDOT:PSS, both as cathode and anode in new all-organic photovoltaic devices.

In the last two years a completely new class of organic-inorganic photovoltaic devices attracted the attention of the scientific community. Hybrid organic-inorganic devices after just two years of developments already show grater performance than the most advanced organic technology, being competitive with the thin film devices. The problem of long-living excited states has been investigated by a simple band structure approach, revealing that the existence of separated $CH_3NH_3PbI_3$ and $CH_3NH_3PbCl_3$ phases, and their relative band alignment, is the source of excitonic dissociation process in the mixed $CH_3NH_3PbI_{3-x}Cl_x$ phase. Knowing this we can think to design new class of devices that can use this process to take an advantage in terms of overall efficiency.

Finally, a certain amount of my work has been also dedicated to energy storage systems. An innovative cathode for lithium batteries has been characterized. Even if more efforts have to be done in order to completely control the stoichiometry of the film, first galvanostatic measures encourage to continue the work. This new type of cathode promises to double the specific capacity of lithium batteries, making them at the same time safer.

Alternative to the batteries, fuel cells can be also used to obtain the energy stored as molecular hydrogen. We reported a combined photoemission and X-ray absorption study on the oxidation kinetic of a bimetallic Pt-Ni alloy that can be used instead of the more expensive platinum. Nickel segregation on the surface and its

selective oxidation is a clear sign of its participation in the catalytic reactions that occurs on the Pt-skin of the alloy, but future studies are required to understand its exact role.

References

[1] B. O'Regan and M. Grätzel. *A low-cost, high-efficiency solar cell based on dye-sensitized colloidal TiO_2 films.* Nature **353**(6346), 737 (1991). 2

[2] A. Yella, H.-W. Lee, H. N. Tsao, C. Yi, A. K. Chandiran, M. K. Nazeeruddin, E. W.-G. Diau, C.-Y. Yeh, S. M. Zakeeruddin, and M. Grätzel. *Porphyrin-sensitized solar cells with cobalt (II/III)-based redox electrolyte exceed 12 percent efficiency.* Science (New York, N.Y.) **334**(6056), 629 (2011). 2

[3] C. W. Tang. *Two-layer organic photovoltaic cell.* Applied Physics Letters **48**(2), 183 (1986). 2, 29

[4] N. S. Lewis. *Toward cost-effective solar energy use.* Science (New York, N.Y.) **315**(5813), 798 (2007). 2

[5] Y. Liang, Z. Xu, J. Xia, S.-T. Tsai, Y. Wu, G. Li, C. Ray, and L. Yu. *For the bright future-bulk heterojunction polymer solar cells with power conversion efficiency of 7.4%.* Advanced materials (Deerfield Beach, Fla.) **22**(20), E135 (2010). 2

[6] A. Haugeneder, M. Neges, C. Kallinger, W. Spirkl, U. Lemmer, and J. Feldmann. *Exciton diffusion and dissociation in conjugated polymer/fullerene blends and heterostructures.* Physical Review B **59**(23), 346 (1999). 2

[7] G. Yu, J. Gao, J. C. Hummelen, F. Wudl, and A. J. Heeger. *Polymer Photovoltaic Cells: Enhanced Efficiencies via a Network of Internal Donor-Acceptor Heterojunctions.* Science (New York, N.Y.) **270**, 1789 (1995). 2

[8] C. J. Brabec, M. Heeney, I. McCulloch, and J. Nelson. *Influence of blend microstructure on bulk heterojunction organic photovoltaic performance.* Chemical Society reviews **40**(3), 1185 (2011). 2, 41

[9] A. Kojima, K. Teshima, Y. Shirai, and T. Miyasaka. *Organometal halide perovskites as visible-light sensitizers for photovoltaic cells.* Journal of the American Chemical Society **131**(17), 6050 (2009). 2, 57

[10] H.-S. Kim, C.-R. Lee, J.-H. Im, K.-B. Lee, T. Moehl, A. Marchioro, S.-J. Moon, R. Humphry-Baker, J.-H. Yum, J.-E. Moser, M. Grätzel, and N.-G. Park. *Lead iodide perovskite sensitized all-solid-state submicron thin film mesoscopic solar cell with efficiency exceeding 9%.* Scientific reports **2**, 591 (2012). 2, 57

[11] J. Burschka, N. Pellet, S.-J. Moon, R. Humphry-Baker, P. Gao, M. K. Nazeeruddin, and M. Grätzel. *Sequential deposition as a route to high-performance perovskite-sensitized solar cells.* Nature **499**(7458), 316 (2013). 2, 57

[12] G. Xing, N. Mathews, S. Sun, S. S. Lim, Y. M. Lam, M. Grätzel, S. G. Mhaisalkar, and T. C. Sum. *Long-range balanced electron- and hole-transport lengths in organic-inorganic $CH_3NH_3PbI_3$.* Science (New York, N.Y.) **342**(6156), 344 (2013). 2

[13] A. Marchioro, J. Teuscher, D. Friedrich, M. Kunst, R. van de Krol, T. Moehl, M. Grätzel, and J.-E. Moser. *Unravelling the mechanism of photoinduced charge transfer processes in lead iodide perovskite solar cells.* Nature Photonics **8**, 1 (2014). 2, 57

[14] M. Armand and J.-M. Tarascon. *Building better batteries.* Nature **451**(7179), 652 (2008). 2

[15] J. F. M. Oudenhoven, L. Baggetto, and P. H. L. Notten. *All-Solid-State Lithium-Ion Microbatteries: A Review of Various Three-Dimensional Concepts.* Advanced Energy Materials **1**(1), 10 (2011). 2

[16] S. Park, Y. Shao, J. Liu, and Y. Wang. *Oxygen electrocatalysts for water electrolyzers and reversible fuel cells: status and perspective.* Energy & Environmental Science **5**(11), 9331 (2012). 3

[17] A. Morozan, B. Jousselme, and S. Palacin. *Low-platinum and platinum-free catalysts for the oxygen reduction reaction at fuel cell cathodes.* Energy & Environmental Science **4**(4), 1238 (2011). 3

[18] D. Briggs and P. Seah. *Practical Surface Analysis, Auger and X-ray Photoelectron Spectroscopy.* Practical Surface Analysis (Wiley, 1990). 3

[19] J. Stöhr. *NEXAFS Spectroscopy*, vol. 25 of *Springer Series in Surface Sciences 25* (Springer, 1992). 3

[20] P. A. Brühwiler, O. Karis, and N. Martensson. *Charge-transfer dynamics studied using resonant core spectroscopies.* Reviews of Modern Physics **74**(July), 703 (2002). 4

[21] J. Schnadt, P. A. Brühwiler, L. Patthey, J. N. O'Shea, S. Södergren, M. Odelius, R. Ahuja, K. Olof, M. Bässler, P. Persson, H. Siegbahn, S. Lunell, and N. Martensson. *Experimental evidence for sub-3-fs charge transfer from an aromatic adsorbate to a semiconductor.* Nature **418**(8), 620 (2002). 7

[22] J. Schnadt, J. N. O'Shea, L. Patthey, L. Kjeldgaard, J. Ahlund, K. Nilson, J. Schiessling, J. Krempasky, M. Shi, O. Karis, C. Glover, H. Siegbahn, N. Martensson, and P. A. Brühwiler. *Excited-state charge transfer dynamics in systems of aromatic adsorbates on TiO_2 studied with resonant core techniques.* The Journal of Chemical Physics **119**(23), 12462 (2003).

[23] L. C. Mayor, J. Ben Taylor, G. Magnano, A. Rienzo, C. J. Satterley, J. N. O'Shea, and J. Schnadt. *Photoemission, resonant photoemission, and x-ray absorption of a Ru(II) complex adsorbed on rutile TiO_2(110) prepared by in situ electrospray deposition.* The Journal of chemical physics **129**(11), 114701 (2008). 7

[24] W. Shockley and H. J. Queisser. *Detailed Balance Limit of Efficiency of p-n Junction Solar Cells.* Journal of Applied Physics **32**(3), 510 (1961). 17

[25] G. Dutton, W. Jin, J. Reutt-Robey, and S. Robey. *Ultrafast charge-transfer processes at an oriented phthalocyanine/C_{60} interface.* Physical Review B pp. 1–4 (2010). 29

[26] W. Chan, M. Ligges, and A. Jailaubekov. *Observing the Multiexciton State in Singlet Fission and Ensuing Ultrafast Multielectron Transfer.* Science **1541**(2011) (2011).

[27] A. E. Jailaubekov, A. P. Willard, J. R. Tritsch, W.-L. Chan, N. Sai, R. Gearba, L. G. Kaake, K. J. Williams, K. Leung, P. J. Rossky, and X.-Y. Zhu. *Hot charge-transfer excitons set the time limit for charge separation at donor/acceptor interfaces in organic photovoltaics.* Nature materials **12**(1), 66 (2013). 29

[28] P. Vilmercati, C. Castellarin-Cudia, R. Larciprete, C. Cepek, G. Zampieri, L. Sangaletti, S. Pagliara, A. Verdini, A. Cossaro, L. Floreano, A. Morgante, L. Petaccia, S. Lizzit, C. Battocchio, G. Polzonetti, and A. Goldoni. *Molecular orientations, electronic properties and charge transfer timescale in a Zn-porphyrin/C_{70} donor-acceptor complex for solar cells.* Surface Science **600**(18), 4018 (2006). 29

[29] P. Vilmercati, C. Castellarin-Cudia, R. Gebauer, P. Ghosh, S. Lizzit, L. Petaccia, C. Cepek, R. Larciprete, A. Verdini, L. Floreano, A. Morgante, and A. Goldoni. *Mesoscopic donor-acceptor multilayer by ultrahigh-vacuum codeposition of Zn-tetraphenyl-porphyrin and C_{70}.* Journal of the American Chemical Society **131**(2), 644 (2009). 29

[30] S. Yoo, B. Domercq, and B. Kippelen. *Efficient thin-film organic solar cells based on pentacene/C_{60} heterojunctions.* Applied Physics Letters **85**(22), 5427 (2004). 29

[31] X. Zhu, Q. Yang, and M. Muntwiler. *Charge-Transfer Excitons at Organic Semiconductor Surfaces and Interfaces.* Accounts of chemical research **42**(11), 1779 (2009).

[32] P. Vilmercati, D. Cvetko, A. Cossaro, and A. Morgante. *Heterostructured organic interfaces probed by resonant photoemission.* Surface Science **603**(10-12), 1542 (2009). 29

[33] C. Tzeng, W. Lo, J. Yuh, R. Chu, and K. Tsuei. *Photoemission, near-edge x-ray-absorption spectroscopy, and low-energy electron-diffraction study of C_{60} on Au(111) surfaces.* Physical Review B **61**(3), 2263 (2000). 29

[34] A. Goldoni, C. Cepek, R. Larciprete, S. Pagliara, L. Sangaletti, and G. Paolucci. *Tuning the charge state of a C_{60} single layer on Ag(100) by Na deposition.* Surface Science **482-485**(0), 606 (2001).

[35] W. L. Yang, V. Brouet, X. J. Zhou, H. J. Choi, S. G. Louie, M. L. Cohen, S. a. Kellar, P. V. Bogdanov, A. Lanzara, A. Goldoni, F. Parmigiani, Z. Hussain, and Z.-X. Shen. *Band structure and Fermi surface of electron-doped C_{60} monolayers.* Science **300**(5617), 303 (2003). 29

[36] D. M. Poirier. *Isolation of fulleride phases by distillation.* Applied Physics Letters **64**, 1356 (1993). 29

[37] M. Kaltenbrunner, M. S. White, E. D. Glowacki, T. Sekitani, T. Someya, N. S. Sariciftci, and S. Bauer. *Ultrathin and lightweight organic solar cells with high flexibility.* Nature communications **3**, 770 (2012). 41

[38] L. Hu, M. Pasta, F. L. Mantia, L. Cui, S. Jeong, H. D. Deshazer, J. W. Choi, S. M. Han, and Y. Cui. *Stretchable, porous, and conductive energy textiles.* Nano letters **10**(2), 708 (2010). 41

[39] S. Hou, Z. Lv, H. Wu, X. Cai, Z. Chu, and D. Zou. *Flexible conductive threads for wearable dye-sensitized solar cells.* Journal of Materials Chemistry **22**(14), 6549 (2012). 41

[40] M. M. Lee, J. Teuscher, T. Miyasaka, T. N. Murakami, and H. J. Snaith. *Efficient hybrid solar cells based on meso-superstructured organometal halide perovskites.* Science (New York, N.Y.) **338**(6107), 643 (2012). 57

[41] J. Noh, S. Im, J. Heo, T. Mandal, and S. Seok. *Chemical Management for Colorful, Efficient, and Stable InorganicÄìOrganic Hybrid Nanostructured Solar Cells.* Nano letters (2013).

[42] B. Conings, L. Baeten, C. De Dobbelaere, J. D'Haen, J. Manca, and H.-G. Boyen. *Perovskite-Based Hybrid Solar Cells Exceeding 10% Efficiency with High Reproducibility Using a Thin Film Sandwich Approach.* Advanced materials (Deerfield Beach, Fla.) pp. 1–6 (2013).

[43] M. Liu, M. B. Johnston, and H. J. Snaith. *Efficient planar heterojunction perovskite solar cells by vapour deposition.* Nature **501**(7467), 395 (2013). 57

[44] S. D. Stranks, G. E. Eperon, G. Grancini, C. Menelaou, M. J. P. Alcocer, T. Leijtens, L. M. Herz, A. Petrozza, and H. J. Snaith. *Electron-hole diffusion lengths exceeding 1 micrometer in an organometal trihalide perovskite absorber.* Science (New York, N.Y.) **342**(6156), 341 (2013). 57

[45] C. Wehrenfennig, G. E. Eperon, M. B. Johnston, H. J. Snaith, and L. M. Herz. *High Charge Carrier Mobilities and Lifetimes in Organolead Trihalide Perovskites.* Advanced Materials **26**(10), 1584 (2014).

[46] Y. Yamada, T. Nakamura, M. Endo, A. Wakamiya, and Y. Kanemitsu. *Photocarrier Recombination Dynamics in Perovskite CH3NH3PbI3 for Solar Cell Applications.* Journal of the American Chemical Society **136**(11610-11613) (2014). 57

[47] M. S. Islam, R. Dominko, C. Masquelier, C. Sirisopanaporn, a. R. Armstrong, and P. G. Bruce. *Silicate cathodes for lithium batteries: alternatives to phosphates?* Journal of Materials Chemistry **21**(27), 9811 (2011). 67

[48] V. R. Stamenkovic, B. Fowler, B. S. Mun, G. Wang, P. N. Ross, C. a. Lucas, and N. M. Marković. *Improved oxygen reduction activity on $Pt_3Ni(111)$ via increased surface site availability.* Science (New York, N.Y.) **315**(5811), 493 (2007). 75